NTNU
Norwegian University of
Science and Technology

Net exhumation estimation from seismic traveltimes and burial history modelling in the Western Barents Sea.

Ricardo Jose Martinez Guzman

Petroleum Geosciences
Submission date: February 2018
Supervisor: Kenneth Duffaut, IGP

Norwegian University of Science and Technology
Department of Geoscience and Petroleum

I would like to acknowledge NPD-Schlumberger for the well log data, and CREWES and Gary, F. Margrave for the Matlab Ray Tracing facility.

I would like to thank my home university USB and their professors for the initial years of training which represent my groundwork as a geophysical engineer. I would like to thank NTNU and their professors for the training and knowledge provided during my master studies.

I would like to thank my supervisor Assoc. Prof. Kenneth Duffaut, for giving me the opportunity to work with this very interesting project, but also for the guidance, advices and inspiring discussions throughout the entire project period.

I would like to thank my father Yensy Martinez, my mother Beatriz Guzman, and my sister Claudia Martinez, for their unconditional love, support, and for always believing in me. This is also yours!

Abstract

A new seismically based technique is proposed for the estimation of net exhumation magnitudes in sedimentary basin areas. The method uses traveltimes mapped from well log data or pre-stack seismic data, starting from the seabed, on a reference area with only subsidence, and from an area suspected to be uplifted. The method is compaction-based, and allows for estimating net exhumation magnitudes at areas where severe uplift and erosion prevent the usage of the shale compaction depth-trend technique. The technique considers the similarity between the stratigraphic sequences from reference and uplifted areas in terms of their NMO parameters and velocity heterogeneity. Linear P-wave velocity functions are then estimated for both areas using dix-type mathematical relations, and compared in a depth dependent scheme. Three sets of net exhumation magnitudes were estimated by applying the method in nine wells spread across the Western Barents Sea. The net exhumation magnitudes increases from the west and southwest where minor or no uplift is predicted, towards the East and North-East, where exhumation magnitudes between 800 m and 1700 m are estimated. Compared to the shale compaction technique, the method is considered to be less affected by abnormal pore pressure development. The estimates are in agreement with published net uplift magnitudes derived from shale compaction and thermal maturity techniques, petrographical and sedimentological analysis, etc. The net exhumation magnitudes were further used in the construction of burial history curves for simulating mechanical and chemical compaction in clean sandstones. The modelling scheme successfully predicts the quartz cement volumes quantified in petrographic analysis, and the porosity, rock moduli, and velocities measured by wireline well logging. The P-wave velocity proved to be the property least affected by factors outside the model. The property modelling appeared to be most sensitive to the maximum temperatures achieved according to the net exhumation magnitudes. Further empirical evidence regarding the quality of the net uplift estimates is provided by positive correlation of the exhumation estimates with present-day differential stress profiles. Moreover, the velocity of exhumation-corrected Barents Sea sandstones is in agreement with published mechanical and chemical compaction velocity depth trends, derived for unexhumed sandstones from the Norwegian and North Sea.

Table of Contents

List of Tables

List of Figures

Chapter 1

Introduction

Net uplift, or net exhumation estimates represents one of the most important inputs in a hydrocarbon exploration setting. Together with its timing, it provides information about the maturation state of a source rock, the expected quality of the reservoirs, and the sealing capacity of a impermeable rock unit. If uplift is not taken into account, a source rock which might have produced hydrocarbons in the past, might be considered today as immature, due to present day burial depth and temperature. Reservoir rocks that have been uplifted will exhibit poorer reservoir quality compared to what would normally be expected at its present day depth (Dore and Jensen, 1996). Units that effectively work as membrane seal in normally compacted areas of a basin, might possibly leak over uplifted areas of a basin, as the rocks are moved from a high temperature - high pressure, plastic strength field, to a strength field in which brittle fracture dominates (Dore and Jensen, 1996). Tight reservoir units might increase its permeability due to fracture development. Re-deposition of erosional products can develop isolated working hydrocarbon kitchens. Furthermore, alternative mechanism of hydrocarbon charging such as methane ex-solution from formation waters, and retrograde condensate drop-out, come into the exploration scheme (Corcoran and Dore, 2005). Hence, exhumation changes the exploration dynamics and strategy, and its accurate prediction is critical for a successful risk assessment of the key elements in a petroleum system. However, net uplift estimation is not restricted to hydrocarbon exploration. It offers also critical insights to other geological processes such as the evolution of passive margins, the role of mantle plumes, evidence for underplating, isostatic readjustment, glacial erosion, etc. (Corcoran and Dore, 2005).

Compaction is defined as the reduction of sediment volume in response to mechanical and thermochemical processes (Corcoran and Dore, 2005). In the mechanical domain, compaction is mainly controlled by the differential stress, which is the difference between the weight of the rock column above a certain depth, and the pressure of the fluid in the pores at the same depth. In the chemical domain, compaction in sandstones com-

prises dissolution of minerals or amorphous material, and precipitation of mineral cement (Bjørlykke and Jahren, 2015). Moreover, in shales clay mineral diagenetic transformations is also expected. If the permeability of the rocks allows the pore pressure to be hydrostatic, a systematic decrease of porosity with increasing burial depth is expected (Hansen, 1996). On the other hand, compaction is considered to be an irreversible process (Magara, 1976; Richardsen et al., 1993; Corcoran and Dore, 2005; Hansen, 1996; Baig et al., 2016). Despite some porosity rebound can occur during exhumation as a consequence of the stress release, a significant number of laboratory tests and empirical observations supports the claim (Corcoran and Dore, 2005). Thus, a normally compacted/hydrostatically pressured rock sequence, will retain the diagenetic properties acquired at maximum burial depth (Baig et al., 2016). The latter is the principle behind the compaction-based technique, which has been used in several studies for the estimation of net uplift magnitudes in sedimentary basin areas Magara (1976); Hansen (1996); Heasler and Kharitonova (1996); Jaspen (1998); Henriksen et al. (2011a); Tassone et al. (2014); Baig et al. (2016).

Shale compaction net exhumation techniques rely upon finding an homogeneous shale with similar characteristics in both reference and uplifted areas. However, this is not always achieved. In the Norwegian part of the Barents Sea, the Paleogene shale Fm., Torsk, is missing in areas that have been severely uplifted. Thus, older shale formations as the regionally preserved Aptian-Albian Kolmule Fm. have to be used. Nevertheless, in areas considered to be at the maximum burial depth as Vestbakken province, the wells do not penetrate this formations. Baig et al. (2016) addressed the problem by using wells from areas with minor uplift as Tromsø Basin where the formation is drilled, and depth correcting those wells to maximum burial depth based on uplift estimates from opal-A to opal-CT to quartz silica-phase transformation. This induces an extra uncertainty that adds to the uncertainty of the shale compaction method itself. Moreover, Henriksen et al. (2011a) have reported uplift magnitudes of 250 m for wells used by Baig et al. (2016) to construct the normal compaction trends (NCT's).

Aven (2017) investigates the use of average velocity profiles derived from check-shot data, in an attempt to quantify the magnitude of net uplift in the Norwegian Barents Sea from rather composite lithologies (effective medium), and not an specific shale formation as previously addressed. However, his technique appears to underpredict the magnitude of net exhumation in areas severely uplifted.

The present study continues the research on effective-medium, compaction-based uplift estimation techniques, and studies the use of seismic traveltimes, as a mean to estimate the net uplift magnitude. Stovas and Ursin (2007) presented a mathematical formulation that allows the estimation of a P-wave linear velocity function that explains the seismic traveltimes through a stack of isotropic layers, given that PP large-offset seismic reflection curves are provided. The present study seeks to make use of Stovas and Ursin (2007) formulation, as the basis for estimating the net uplift magnitude at different locations across the Western Barents Sea, using composite lithological sequences, rather than a particular shale unit. Moreover, since the uplift estimates will be based on effective media, wells from areas currently at their maximum burial depth, from the Norwegian Sea and North Sea, can be used as reference. Lastly, the net uplift magnitudes will be used as sensitive pa-

rameter for the construction of burial history curves, which will be used as input for a sandstone property modelling using Lander and Walderhaug (1999) mechanical and chemical compaction models. The purpose is to investigate whether the exhumation estimates can explain published quartz cement volumes observed in thin sections petrographical analysis, and whether the porosity, elastic moduli and velocities measured at well locations, can be predicted.

1.1 Previous studies on compaction-based net uplift estimation.

Magara (1976) studied the thickness of sedimentary rocks removed by erosion in the Southwestern part of the Western Canada Basin using shale compaction techniques, and described the decrease in interval transit time due to compaction by means of a simple exponential relation. Hansen (1996) used sonic transit time for normally compacted and normally pressured shales from 32 wells from the Norwegian shelf, to derive a normal compaction trend (NCT) on the form of Magara (1976). With it, estimated net uplift magnitudes in 29 wells, by calculating the difference between the present day burial depth of the given formation and the maximum burial depth according to the NCT. Heasler and Kharitonova (1996) argued that the simple exponential compaction model of Magara (1976) incorrectly predicts the sonic transit time in a totally compact rock, and proposed an improved exponential model by adding to the simple exponential relation, a constant shift approximately equal to the rock matrix transit time. Baig et al. (2016) derived NCT's of the improved exponential model form, for the regionally preserved Aptian-Albian Kolmule Fm. and the Paleogene Torsk Fm, from sonic transit time data from 3 wells located at Sørvestsnaget Basin, Vestbakken Volcanic Province, and Tromsø Basin, respectively.

Diverging from the exponential compaction approach, Japsen (1993) presented a new quantity named the velocity anomaly, defined as the deviation between a velocity measurement and a linear velocity depth function for the formation. Jaspen (1998) derived a normal velocity-depth trend for the Upper Cretaceous-Danian Chalk Group in the North Sea, composed of linear segments of velocity-depth functions, and estimated net uplift and overpressure magnitudes from the velocity anomalies. Jaspen (2000) studied velocity-depth data from wells in the UK southern North Sea and Danish wells outside the late Cenozoic depocentre, and extended his previous work by exemplifying how multi-phase erosion can be quantified from sonic data when two homogeneous units, which have not been simultaneously at maximum burial depth, are encountered in the same wells.

Richardsen et al. (1993) used interval velocity from seismic sections to estimate the amount of post-early Cretaceous uplift and erosion within the Southern Barents Shelf. However, the erosion estimates were not based on the seismic velocities independently. The method relied rather on a calibration curve constructed for a shale of fixed density/velocity within the (Aptian-Albian) Kolmule Fm, that allowed the mapping of net exhumation estimates from vitrinite reflectance and fission track data, into the seismic

volume.

In a more comprehensive study, Henriksen et al. (2011a) estimated net exhumation magnitudes within the Norwegian Barents Sea through a variety of compaction-based, thermal-based, and other techniques, and discussed the methods in terms their uncertainty level. Moreover, they evaluated their uplift estimates by comparing core porosity of Late Triassic Jurassic sandstones to Ramm and Bjørlykke (1994) porosity depth-trend derived for Middle Jurassic sandstones from the Halten Terrance in the mid-Norwegian Shelf. Notwithstanding, describing mechanical and chemical compaction with a single linear trend, represents rather a gross approximation.

Chapter 2

Theory

2.1 Erosion, Uplift, and Exhumation: Terminology and Considerations

A broad terminology have been used in the bibliography to describe the movement of rock masses in the continents and sedimentary basins, and the removal of overburden that is generally related to it. Depending upon the frame of reference used to quantify the rock mass movements, the different mechanisms that causes it, and the interrelation between the events and its timing, etc. different terms are used. Therefore, a description of this terminology is mandatory.

Uplift is a broad term that refers to the vertical displacement of a rock body or marker horizon with respect to a selected datum. It is distinguished from *Surface uplift*, which refers to the vertical movement of the earth's surface with respect to a selected datum. These data are generally mean sea level, as an approximation of the geoid. Upward movements are considered positive while downward movements are considered negative (Riis and Jensen, 1992).

According to the mechanisms which causes it uplift can be divided into: *tectonic uplift*, when the uplift occurs in response to tectonic forces or temperature changes, and *Isostatic uplift*, when it occurs in response to loading or unloading of the earth's crust. The uplift is measured with respect to mean sea level, which makes the term vague considering the eustatic variations in the sea level.

Erosion comprises local subaerial or submarine removal of material by mechanical and chemical processes (Corcoran and Dore, 2005), and it is closely related to uplift. In general, erosion is expected whenever a rock mass is uplifted above wave base, while passive

uplift is expected after removal of an isostatic load (Dore and Jensen, 1996). However, if an area experiences rapid uplift, erosion may not have time to reduce the topography (Figure 2.1c). Conversely, the erosion caused by a deeply incised valley or glacially overdeepened basin may be to local to be compensated isostatically (Dore and Jensen, 1996). Under marine conditions, erosion is not only restricted to uplift, it may take place during periods of subsidense or static conditions (Figure 2.1b) (Riis and Jensen, 1992). Taking into account the considerations above, erosion can be consistently defined as the difference between the uplift of the rocks (or a given marker) and the surface uplift (Riis and Jensen, 1992).

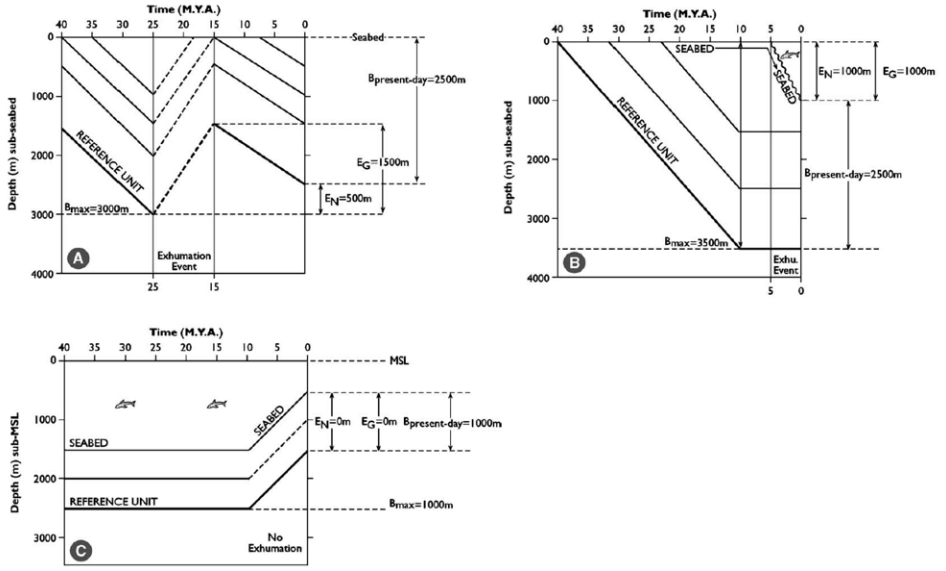

Figure 2.1: Schematic representation of the uplift and erosion terminology. A) Gross exhumation E_G, and Net exhumation E_N. B) Erosion takes place without any necessary uplift. See how maximum subsidence is reached at 10 M.Y.A, together with maximum burial, whereas from 5 M.Y.A to present, while rocks are still at maximum subsidence, maximum burial is lost. C) Rocks are uplifted without erosion taking place. Note how Riis and Jensen (1992) definition of erosion holds for all scenarios. Modified from (Corcoran and Dore, 2005).

Exhumation, is a general concept used to describe removal of overburden material, regardless of the causes that originate the removal, such that previously buried rocks are exposed at earth's surface (Corcoran and Dore, 2005).

Within the context of petroleum exploration, scientist are interested in the *net exhumation* or *net uplift* as defined by Dore and Jensen (1996), which is the difference between the present day burial depth of a reference unit and its maximum burial depth prior to exhumation (Corcoran and Dore, 2005). The interest comes from the idea that if maximum burial depth coincides with maximum compaction and temperature exposure, then the first is the main parameter controlling the maturation, compaction and diagenetic state of source, reservoir and seal rocks, and it has therefore significant implications in the hydrocarbon

prospectivity of a basin (Corcoran and Dore, 2005).

Gross exhumation, on the other hand, describes the magnitude of erosion that occurs at a particular unconformity prior to post-exhumation re-burial (Figure. 2.1a)(Corcoran and Dore, 2005). Net exhumation can be converted to gross exhumation if the timing of the exhumation event prior to maximum burial depth is known (Tassone et al., 2014).

Riis and Jensen (1992) distinguished between the terms *maximum burial* and *maximum subsidence*. The first is described as the maximum overburden over a marker horizon, while the second refers to the minimum altitude of that horizon. These two are usually used interchangeably in the bibliography. Nevertheless, under marine conditions, where deposition may continue after the time of maximum burial, or when erosion take place without any apparent uplift of the rocks, they might differ from each other, as illustrated in Figure 2.1b.

2.2 Uplift estimation: The compaction based technique

Compaction can be defined as the reduction in bulk volume of a mass of sediments as pressure is applied (Wilson and Stanton, 1994). Athy (1930) described compaction as exponentially decaying porosity function of depth

$$\phi = \phi_o e^{-bz} \tag{2.1}$$

where, ϕ is the porosity, ϕ_o is the depositional porosity, and b is the compaction coefficient controlling the rate of porosity loss with depth.

The method is built upon two fundamental assumptions (Corcoran and Dore, 2005):

1. Compaction is an irreversible process: Although some porosity rebound can occur during exhumation, a large number of laboratory experiment and empirical observations confirm the irreversible character of compaction.
2. The basin has experienced equilibrium compaction (Compaction under hydrostatic pressure conditions).

Under these conditions, a shale will thus retain the compaction it has gain at maximum burial depth (Hansen, 1996).

The general methodology to compute an absolute estimate of the magnitude of exhumation at a particular well location comprises two main steps (Corcoran and Dore, 2005):

1) Establishment of a reference plot of porosity, or another geophysical parameter that reflects compaction, versus depth, for a given normally-buried, unexhumed rock succes-

sion within the basin (Figure 2.2a). Porosity-depth curves can be generated from direct porosity measurements on core plugs retrieved from a wellbore or it can be derived from wireline log density and interval transit time measurements. However, the sonic log has been widely used as a compaction indication itself. The advantage of using sonic logs over porosity data is that the latter is usually acquired only over reservoir sections, while sonic data is generally available throughout the whole well section (Baig et al., 2016). Moreover, the reduction of vertical stress experienced during uplift may induce fractures in the uplifted rocks. The acoustic waves transmitted by the sonic tool avoid such fractures and are mainly affected by intergranular porosity, while density logs for instance, are affected by both intergranular and fracture porosity Hansen (1996).

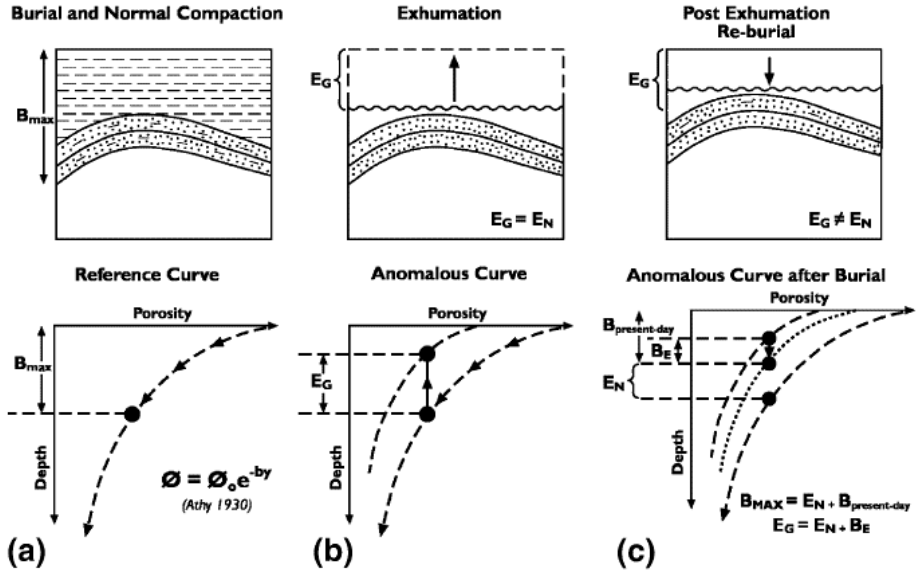

Figure 2.2: Schematic representation of the compaction-based net exhumation estimation technique. a) Establishment of a reference plot of a selected compaction parameter (porosity in the figure) for a normally buried and unexhumed rock succession. b) Establishment of the compaction curve for the well under study. c) Net exhumation is given by the vertical depth between the compaction curves of the reference and uplifted wells. From Corcoran and Dore (2005).

2) A porosity-depth curve or a proxy thereof, is established for each well and compared with the established reference curve (Figure 2.2b). Stratigraphic units that are shallower than their maximum burial depth will have anomalously low porosity (low transit time) compared to present-day burial depth. The displacement along the depth axis of the observed compaction parameter (transit time, porosity, etc.) from the normally compacted unexhumed trend yields the estimate of the magnitude of net exhumation at that location (Figure 2.2c). The compaction method for determination of uplift and erosion will only yield the original magnitudes of uplift *(*Gross exhumation) when no sediment has been deposited after erosion Hansen (1996) (Figure 2.2b).

2.3 Estimation of Linear P-wave Velocity functions from large-offset PP seismic reflections

The seismic traveltimes for a sequence of isotropic, horizontally layered strata with a given P-wave velocity profile can be explained by a linear P-wave velocity function of the form:

$$Vp(z) = Vp_0(1 + \beta_p z) \tag{2.2}$$

where $z = 0$ corresponds to the top of the layer, Vp_0 to the velocity at the top of the layer, and β_p to the velocity gradient in units of $[distance]^{-1}$. Stovas and Ursin (2007) proposed a method to estimate a P-wave linear velocity function from PP large-offset seismic traveltimes, for a horizontally layered medium with isotropic layers, with constant P- and S- wave velocity gradients.

Stovas and Ursin (2007) methodology can be summarized in three main steps:

1. Velocity analysis on large-offset PP seismic traveltimes curves to obtain NMO parameters at the top and bottom of a given layer.

2. Solving equation

$$f(y_p) = \frac{(\Delta(T_0 V_{nmo}^4 S)\Delta(T_0)}{[\Delta(T_0 V_{nmo}^2)]^2} - 1 = \frac{\left(1 + y_p + \frac{y_p^2}{2}\right)\ln(1 + y_p)}{y_p\left(1 + \frac{y_p}{2}\right)} - 1 \tag{2.3}$$

   for y_p, where Δ denotes the difference in parameters between the reflections from the base and top of the layer of interest, T_0 is the zero-offset two-way traveltime, V_{nmo} is the P-wave NMO velocity, S is the heterogeneity coefficient, and $y_p = \beta H$. H stands for the thickness of the layer.

3. Compute layer parameters from Stovas and Ursin (2007) analytical expressions:

$$Vp_0 = \sqrt{\frac{\Delta(T_0 V_{nmo}^2)\ln(1 + y_p)}{\Delta(T_0) y_p (1 + \frac{y_p}{2})}} \tag{2.4}$$

$$\beta_p = \pm\sqrt{\frac{2y_p(2 + y_p)\ln(1 + y_p)}{\Delta(T_0)\Delta(T_0 V_{nmo}^2)}} \tag{2.5}$$

$$H = \frac{y_p}{\beta_p} \tag{2.6}$$

.

2.4 PP Traveltime Modelling

Stovas and Ursin (2007) explain that considering a stack of isotropic layers, the two-way PP traveltime as a function of the offset x can be estimated by Ursin and Stovas (2006):

$$T(x) = \left[T_0^2 + \frac{x^2}{V_{nmo}^2} - \frac{(S-1)x^4}{4V_{nmo}^4 \left[T_0^2 + \frac{(S-1)}{2} \frac{x^2}{V_{nmo}^2} \right]} \right]^{1/2} \tag{2.7}$$

where T_0, V_{nmo} and S are NMO parameters: two-way zero-offset traveltime, P-wave NMO velocity and heterogeneity coefficient, respectively.

2.5 Basic Velocity Types in exploration geophysics

Herron (2011) presents a review of the basic velocity types commonly used in the oil and gas exploration.

2.5.1 Interval Velocity

The interval velocity V_{int}, is the distance traveled per unit time, where the distance traveled is the thickness of a a given layer or stratum (Herron, 2011).

$$V_{int_i} = 2\frac{\Delta Z_i}{\Delta t_i} \tag{2.8}$$

where ΔZ_i is the thickness of the i_{th} layer, and Δt_i its respective thickness.

2.5.2 Average Velocity

Average Velocity V_{avg} is defined as the distance traveled per unit time, where the distance traveled is given by the total thickness of many layers or strata measured from the top of the uppermost layer to the base of the lowermost layer:

$$V_{avg} = 2\frac{\sum \Delta Z_i}{\sum \Delta t_i} = \frac{\sum V_{int} \Delta t_i}{\sum \Delta t_i} \tag{2.9}$$

where V_{int} is the interval velocity, and ΔZ_i and Δt_i, are the thickness and zero-offset interval two-way traveltime of the i_{th} layer, respectively.

2.5.3 RMS Velocity

Root-mean-square (RMS) velocity V_{rms}, is a statistical quantity calculated from V_{int} as

$$V_{rms} = \frac{\sum V_{int}^2 \Delta t_i}{\sum \Delta t_i} \tag{2.10}$$

2.6 V(z) ray tracing

Margrave (2000) reviews some of the mathematics behind the Ray Tracer of the Crewes Matlab Toolbox. Consider a sequence of N discrete horizontal layers identified as $k = 1, 2, ..., N.$, with interval velocity V_k, and thickness ΔZ_k. For a ray described by its ray parameter p (horizontal component of the slowness vector) that travels from the top of layer 1 to the bottom of layer N, the traveltime expression becomes

$$t(p) = \sum_{k=1}^{N} \frac{\Delta Z_k}{V_k \sqrt{1 - p^2 V_k^2}} \tag{2.11}$$

$$x(p) = \sum_{k=1}^{N} \frac{p V_k \Delta Z_k}{\sqrt{1 - p^2 V_k^2}} \tag{2.12}$$

The quantity pV_k is easily shown to be $\sin\theta_k$, where θ_k is the angle the ray makes with the vertical in the kth layer. At the same time $\cos\theta_k = \sqrt{1 - p^2 V_k^2}$. The procedure is known as *ray shooting* because the starting point and direction of the ray are specified but the final position is unknown until calculation is computed.

The problem thus consist in finding the ray parameter p that solves equations (2.11) and (2.12). To solve this, an iterative procedure is used. Consider the shooting position x_1, at the top of layer 1 and the receiver position x_2 at the base of layer N as shown in Figure 2.3. A fan of M rays starting at x_1 that are estimated to bracket the point x_2 can be shot. Assuming $x_1 > x_2$ the fan of M rays to be shot are allowed to vary between $p_1 = 0$ and $p_{max} = V_{max}^{-1}$. If two rays p_k and p_{k+1} from the fan of rays shot $k = (1, 2..., M-1)$ bracket the point x_2, then a new fan of M rays can be shot with p_k and p_{k+1} as the extremal ray parameters. The procedure is then repeated until a ray is found that comes within a defined *capture radius* around x_2.

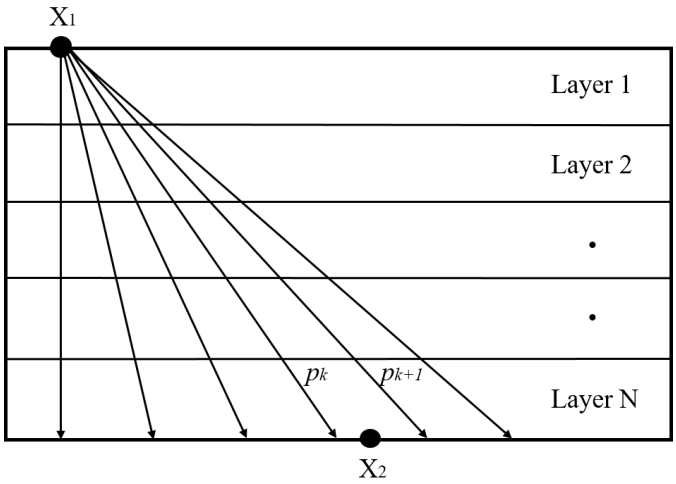

Figure 2.3: Schematic representation of the ray tracing procedure. If two rays p_k and p_{k+1} from the fan of rays shot bracket the point x_2, then a new fan of M rays can be shot with p_k and p_{k+1} as the extremal ray parameters

2.7 Heterogeneity Factor

Al-Chalabi. (1974) presented a quantity named the Heterogeneity Factor which gives a measure of the degree of velocity heterogeneity in the ground. This quantity is always positive and its lower bound is equal to zero when the model is isotropic. It is expressed as

$$g = \frac{V_{rms}^2 - V_{avg}^2}{V_{avg}^2} \tag{2.13}$$

where V_{rms} and V_{avg} are the RMS and average velocities, respectively. V_{rms} equals V_{avg}, when the ground is homogeneous, and isotropic. On the contrary, as the ground becomes more heterogeneous, V_{rms} progressively exceeds V_{avg}. The heterogeneity factor g is independent of the order of layering.

2.8 Burial History Modelling

Lander and Walderhaug (1999) proposed a model that allows the prediction of porosity in sandstones whose porosity loss is mainly controlled by mechanical compaction and quartz cementation.

2.8.1 Lander and Walderhaug (1999) Mechanical Compaction Model

Compaction in sandstones is controlled by four major mechanisms: the reduction of bulk rock volume in response to grain rearrangement, plastic deformation, dissolution, and brittle deformation (Wilson and Stanton, 1994).

1. Grain rearrangement: comprises rotation and slippage of grains into more stable packing configurations (Wilson and Stanton, 1994). It is considered by a number of petrographers as the primary control on compaction of well-sorted sandstones which are poor in matrix and ductile grains (Lander and Walderhaug, 1999).

2. Plastic deformation: involves bending of the grains under applied overburden stress, and squashing of grains into the pore space. It represents a minor compaction mechanism in highly quartzose or feldspathic sandstones, though it can become a major compaction mechanism when ductile grain content significantly exceeds 10% (Wilson and Stanton, 1994).

3. Dissolution: occurs at the grain contacts in response to increasing overburden pressure concentrated at the grain contacts (Wilson and Stanton, 1994). There is little empirical evidence of it being a primary control on reservoir quality for clean sands. Despite grain dissolution at stylolites is common, such dissolution has little effect on rock properties at thin-section or core-plug level (Lander and Walderhaug, 1999).

4. Britte fracturing: Since the number and area of load-bearing contacts decrease with increasing grain size, coarser grained sandstones are more prone to fracturing. However, it represent a minor compaction mechanism in most sands (Wilson and Stanton, 1994).

Lander and Walderhaug (1999) proposed a mechanical compaction model that accounts for grain rearrangement, grain ductility, sorting, and size, as a function of effective stress. It relies on the intergranular volume (IGV) as indirect measure of compaction, and it can be easily compared to thin-section standard point-count data. Moreover, it can be used directly in the simulation of intergranular porosity when cement volumes known. The compaction function is:

$$IGV = IGV_f + (\phi_o + m_o - IGV_f)e^{-\beta\sigma_{es}} \tag{2.14}$$

where, IGV is the sum of pore space, cements, and matrix material in volume fraction; IGV_f represents the stable packing configuration in volume fraction; ϕ_o is the depositional porosity (volume fraction); m_o is the inital proportion of matrix material (volume fraction); β represents the exponential rate of IGV decline with effective stress (MPa$^-$1); and lastly, σ_{es} is the maximun effective stress in MPa. It assumes that the matrix material in grain supported sandstone only exhibits minor compaction, and that no cements occur at the time of deposition.

2.8.2 Walderhaug (1996) Quartz cementation Model

Walderhaug (1996) proposed a kinetic model that simulates quartz cementation and the resultant porosity loss in quartzose sandstones as a function of temperature and time. The model is build around four fundamental assumptions (Lander and Walderhaug, 1999):

1. The quartz cement is sourced from stylolites or individual grain contacts containing clay or mica.
2. Silica precipitation is the rate-limiting step.
3. The surface area available for quartz cement precipitation is a function of the fraction, size, and extent of coating of quartz, together with the porosity.
4. No quartz dissolution occurs within the frame of reference for the simulation.

At constant temperature, the volume of quartz cement Vq (in cm^3) that precipitates in 1 cm^3 volume of sandstone with quartz surface area A (in cm^2), as a function of time t (in s), is given by

$$Vq = \frac{MrAt}{\rho} \tag{2.15}$$

where M represents the molar mass of quartz (60.09 g/mol); r, the quartz precipitation rate in moles/cm^2s; and ρ, the density of quartz (2.65 g/cm^3). The quartz precipitation rate is given by a logarithmic function of temperature

$$r = a10^{bT} \tag{2.16}$$

where T is the temperature (°C), and a and b are constants set to 1.98x10^{-22} moles/cm^2s and 0.022 1/°C, respectively. When temperature varies over time, the integrals presented by Walderhaug (1996) for the calculation of the volumes of quartz cement can be solved numerically by rewriting equation (2.15) in terms of the discrete time step dt (in s) (Blazevic, 2017):

$$Vq_n = Vq_{n-1} + \frac{Mr_{n-1}A_{n-1}dt}{\rho} \tag{2.17}$$

The subscript $n = 1, 2...., N$ refers to each of the steps at which quartz cement is precipitated, and $n = 1$, represents the step when the rock is at the onset of quartz cementation. The initial available surface area for cementation ($n = 1$), A_0 (in cm^2), can then be computed as

$$A_0 = \frac{6(1-C)f}{D} \tag{2.18}$$

where, D is the average sphere diameter (cm), f is the fraction of detrital quartz, and C is the fraction of quartz surface area that is coated by clay. For subsequent time steps, the porosity ϕ_n, and the quartz surface area A_n, are updated as in Walderhaug (1996) by

$$\phi_n = \phi_0 - Vq_n \tag{2.19}$$

$$A_n = A_0 \frac{\phi_n}{\phi_0} \tag{2.20}$$

2.9 Rock Physics Modelling

If the effective elastic properties of a mixture of grains and pores are to be predicted, three key aspects have to be specified: 1) The volume fractions of the various phases; 2) the elastic moduli of the various phases; 3) The geometric details of how the phases are arranged relative to each other. If we specify only the volume fractions and constituent moduli, only the upper and lower bounds can be predicted (Mavko et al., 2009).

Dvorkin and Nur (2002) present a review of the rock physics diagnostics techniques that can be used to infer rock microstructure from velocity-porosity relations.

2.9.1 Friable Sand Model

The friable sand model (Dvorkin et al., 1999) connects two end points in the elastic-modulus-porosity plane through the algebraic expression of the lower Hashin-Shtrikman (1963) bound. The high porosity end point is the at critical porosity ϕ_c (i.e.the porosity above which the rock can exist only as a suspension), and the low porosity end point is at zero porosity, where the elastic properties of the effective medium are equal to those of the solid phase. At the critical porosity the the dry bulk K_{HM} and shear μ_{HM} rock are given by the Hertz-Mindlin (1949) theory (Dvorkin et al., 1999):

$$K_{HM} = \left[\frac{n^2(1-\phi_c)^2\mu^2}{18\pi^2(1-\nu)^2} P \right]^{1/3} \tag{2.21}$$

$$\mu_{HM} = \frac{5-4\nu}{5(2-\nu)} \left[\frac{3n^2(1-\phi_c)^2\mu^2}{2\pi^2(1-\nu)^2} P \right]^{1/3} \tag{2.22}$$

$$\nu = \frac{3K - 2\mu}{2(3K+\mu)} \tag{2.23}$$

where, P is the effective pressure (the difference between confining pressure and pore pressure); μ and ν refers to the shear modulus and Poisson's ratio of the solid grains; and n is the coordination number (the average number of contacts per grain). K, and μ refers to the bulk and shear moduli of the solid grains, respectively.

The friable sand model assumes that porosity decreases from the initial critical porosity due to deposition of solid matter away from the grain contacts (Figure 2.4a). This

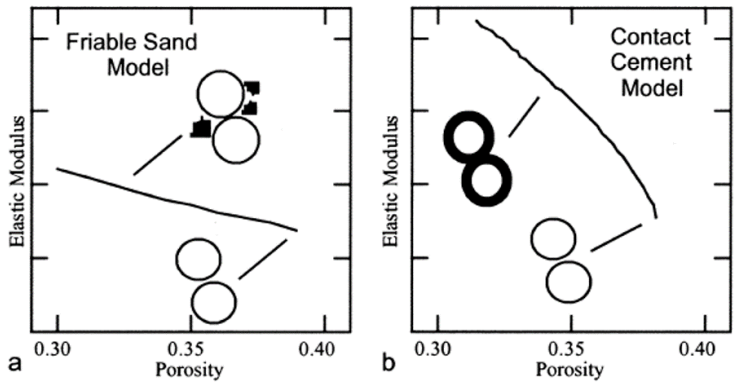

Figure 2.4: a) Deposition of solid matter away from the grain contacts reduces the porosity with a slight impact on the rock stiffness. b) Contact cement induces a dramatic increase in the stiffness of the rock with only a small decrease in porosity. Modified from Dvorkin and Nur (2002).

diagenetic process can be interpreted as deteriorating grain sorting, decreasing porosity while exhibiting only a slight increase in the rock stiffness (Avseth et al., 2010).

The bulk and shear moduli of the dry frame K_{Dry} and μ_{Dry}, respectively, are given by:

$$K_{Dry} = \left[\frac{\frac{\phi}{\phi_c}}{K_{HM} + \frac{4}{3}\mu_{HM}} + \frac{1 - \frac{\phi}{\phi_c}}{K + \frac{4}{3}\mu_{HM}} \right]^{-1} - \frac{4}{3}\mu_{HM} \tag{2.24}$$

$$\mu_{Dry} = \left[\frac{\frac{\phi}{\phi_c}}{\mu_{HM} + z} + \frac{1 - \frac{\phi}{\phi_c}}{\mu + z} \right]^{-1} - z \tag{2.25}$$

where, K_{HM} and μ_{HM}, refers to the Hertz Mindlin dry bulk and shear moduli, respectively; ϕ refers to porosity; and ϕ_o to the critical porosity.

2.9.2 Models for unconsolidated marine sediments

Dvorkin et al. (1999) proposed an analogous to the friable sand model to predict the elastic properties of high porosity sediments. To arrive at porosities above the critical porosity, empty voids are added inside the sphere pack in the Hashin-Shtrikman fashion (Figure 2.5).

The effective bulk and shear dry-rock moduli, K_{Dry} and μ_{Dry}, respectively, are given

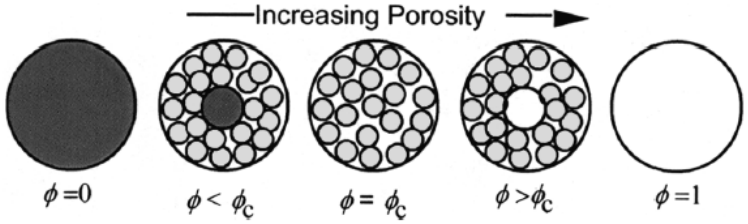

Figure 2.5: Schematic representation of the friable sand, and unconsolidated marine sediments models under the Hashin-Shtrikman geometric arrangement, to arrive at porosities below and above the critical porosity ϕ_c, respectively. From Dvorkin and Nur (2002).

by:

$$K_{Dry} = \left[\frac{(1-\phi)/(1-\phi_c)}{K_{HM} + \frac{4}{3}\mu_{HM}} + \frac{(\phi-\phi_c)/(1-\phi_c)}{\frac{4}{3}\mu_{HM}} \right]^{-1} - \frac{4}{3}\mu_{HM} \tag{2.26}$$

$$\mu_{Dry} = \left[\frac{(1-\phi)/(1-\phi_c)}{\mu_{HM} + z} + \frac{(\phi-\phi_c)/(1-\phi_c)}{z} \right]^{-1} - z \tag{2.27}$$

$$z = \frac{\mu_{HM}}{6} \left(\frac{9K_{HM} + 8\mu_{HM}}{K_{HM} + 2\mu_{HM}} \right) \tag{2.28}$$

where, K_{HM} and μ_{HM}, refers to the Hertz Mindlin dry bulk and shear moduli, respectively; ϕ refers to porosity; and ϕ_o to the critical porosity.

2.9.3 Contact-Cement Model

The contact-cement model (Dvorkin and Nur, 1996) assumes that porosity reduces from the initial porosity of a sand pack as a result of uniform deposition of cement layers on the surface of the grains (Figure 2.4b). The contact cement induces a dramatic increase in the stiffness of the rock with only a small decrease in porosity (Avseth et al., 2010). The dry-rock bulk modulus K_{Dry}, and dry-rock shear modulus μ_{Dry}, are calculated as

$$K_{Dry} = \frac{n(1-\phi_c)M_c S_n}{6} \tag{2.29}$$

$$\mu_{Dry} = \frac{3K_{Dry}}{5} + \frac{3n(1-\phi_c)\mu_c S_\tau}{20} \tag{2.30}$$

where ϕ_c is the critical porosity; K_c and μ_c are the bulk and shear moduli of the cement material, respectively; $M_c = K_c + 4\mu_c/3$ is the compressional modulus of the cement;

and n is the coordination number. Parameters S_n and S_τ are proportional to the normal and tangential stiffnesses, respectively. However, the expressions for those parameters are not expressed here. The reader may be referred to Dvorkin and Nur (1996) for a complete description of the expressions.

Chapter 3

Geological Setting

The Barents Sea is located in the Northwestern corner of the Eurasian continental shelf (Faleide et al., 2015). With water depths varying around 300 m, it represents one of the largest areas of continental shelf on the globe. It is bounded by the northern Norwegian and Russian coasts, the Novaya Zemlya, Franz Josef Land and Svalbard archipelagos, and the eastern margin of the deep Atlantic ocean (Doré, 1995) (See Figure 3.1). The west and north, comprises young passive margins that developed in response to Cenozoic opening of the Norwegian-Greenland Sea and the Eurasia Basin (Faleide et al., 2015).

The Barents sea was originally formed by two major Paleozoic continental collisions. The first collision event, the Caledonian orogeny (culminated in Early Devonian), resulted in the closure of the Iapetus Ocean, a major seaway occupying a similar position to the present northeast Atlantic. The Caledonian orogeny consolidated the Laurentian plate (Greenland, North America) and the Baltic plate (Scandinavia, western Russia) into the Laurasian continent (Doré, 1995).The second collision, related to the Uralian Orogeny, occurred between the Laurasian continent and Western Siberia. The process culminated in latest Permian-earliest Triassic, and produced the Ural mountain Chain, whose northern extension, Novaya Zemlya, represents the eastern margin of the Barents Sea (Doré, 1995).

The present study focuses on the western part of the Barents Sea, also known as the Norwegian Barents sea. The post-Caledonian history of the western Barents sea is dominated by three major extensional phases: Late Devonian-Carboniferous, Middle Jurassic-Early Cretaceous, and Early Tertiary (Faleide et al., 1984). The Late Paleozoic extension was dominated by Devonian collapse of the newly formed Caledonian orogenic belts (Baig et al., 2016). The crustal extension led to the development of half grabens, and later, a regional sag basin that covered major parts of the current Barents sea (Henriksen et al., 2011b). The carboniferous rift phase resulted in structural trends striking northeast to north that dominated most of the southwestern Barents Sea. Tromsø, Bjønøya,

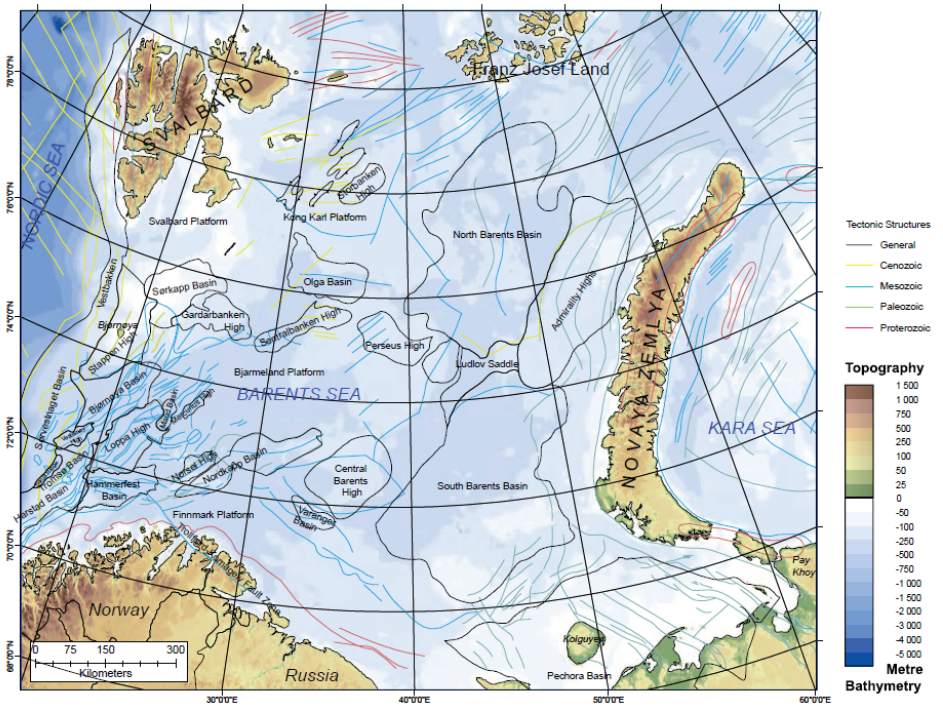

Figure 3.1: Map of the greater Barents Sea. The Barents sea is bounded by the north Norwegian and Russian coasts, the Novaya Zemlya, Franz Josef Land and Svalbard archipelagos, and the eastern margin of the deep Atlantic ocean (Doré, 1995). Figure taken from Smelror et al. (2009).

Nordakapp, Fingerdjupet, Maud, and Ottar basins are interpreted as rift basins formed at this time (Faleide et al., 2015). During Devonian and Carboniferous-Permian the eastern Barents Sea was uplifted as consequence of the Uralian Orogeny, producing pronounced changes in the physiography of the basin (Henriksen et al., 2011b).

During Early Triassic regional deepwater basin covered much of the Barents Sea. The Uralian highland, and the Baltic Shield, acted as sediment source, and large amounts amounts of clastic sediments were deposited (Faleide et al., 2015). Some areas were partially exposed during Middle Triassic time, resulting in northward and westward prograding deltaic systems. In the Late Triassic, regression took place, and the shoreline was moved back to the south and east of the southeastern Barents Sea (Faleide et al., 1984).

The lower-Middle Jurassic interval is dominated by sandstones through the Barents Sea (Faleide et al., 1984), as shown in Figure 3.2. This sands are of particular relevance since part of this study consist on modelling the variation through time of some of their most important petrophysical properties.

A renewed rifting phase occurred during Late Jurassic-Early Cretaceous, separating

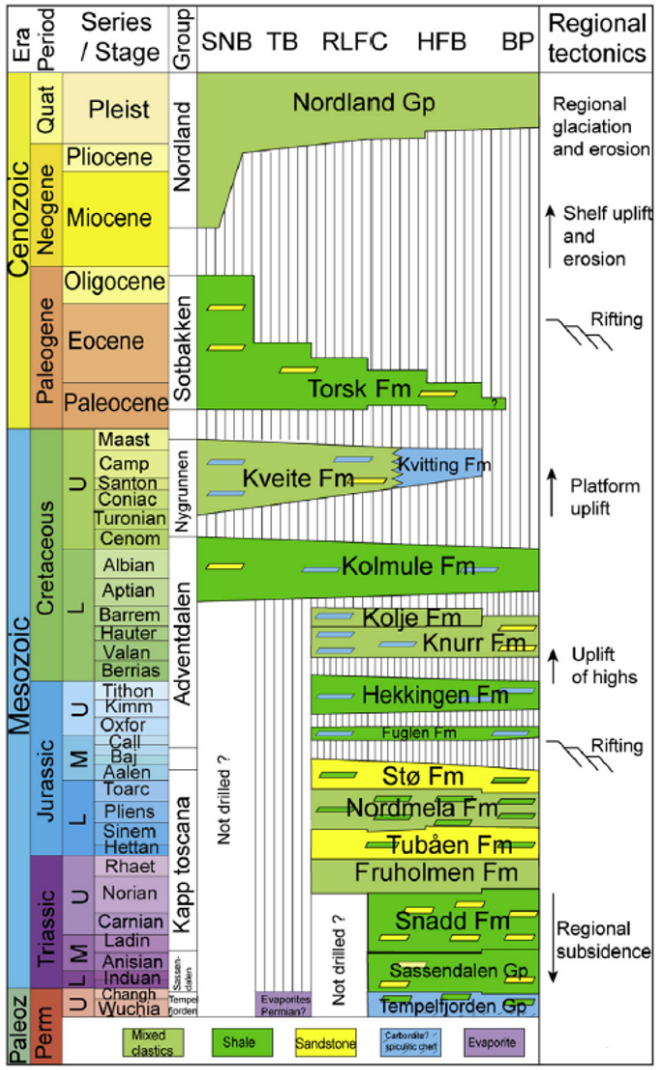

Figure 3.2: Chronostratigraphic Chart for the southwestern Barents Sea. Note that most of the sandstones were deposited during the Early-Middle Jurassic. Several unconformities are recognized in the area, with the Base Paleogene unconformity and the upper regional unconformity (URU) being the most importants. BP, Bjarmeland Platform; HFB, Hammerfest Basin; RLFC, Ringvassøy-Loppa Fault Complex; SNB, Sørvestsnaget Basin; TB, Tromsø Basin. Modified from Baig et al. (2016).

deep basins in the west from the shallow basins in the east (Baig et al., 2016). Bjørnøya, Tromsø and Harstad basins were developed as prominent rift basins during this episode (Faleide et al., 2015). The northern Barents Sea, on the other hand, was characterized by widespread magmatism without faulting. Deposition in the Upper Cretaceous occurred

mainly in the southwestern Barents Sea, where rocks continued to subside in response to faulting (Faleide et al., 2015).

The focus of the rifting has moved westward since the Late Paleozoic, and terminated with the opening of the Norwegian-Greenland Sea during the Paleocene-Eocene (Baig et al., 2016). The western margin of the Barents Sea developed then as a shear margin, comprising a southern sheared margin along the Senja Fracture Zone, a northern and sheared and later rifted segment along the Hornsund Fracture zone, and a central volcanic rifted segment along Vestbakken Volcanic Province (Baig et al., 2016).

The Late Cenozoic evolution was characterized subsidence of the basin margins and deposition of thick sedimentary wedges over it, where uplifted areas of the Barents Sea served sediment source (Faleide et al., 2015).

In total, three exhumation episodes have been attributed to the Barents Sea during Cenozoic: One in the Late Paleocene-Early (55-50 Ma) related to the opening of the Norwegian-Greenland Sea, a second, of age Oligocene-Miocene (30-15 Ma), related to inversion during the development of the passive margin, and a third, of fluvio-glacial origin, during the Late Pliocene-Pleistocene glaciation (2.6-0 Ma) (Zattin et al., 2016). Evidence of it can be observed in the major upper regional unconformity (URU) at the base of the Quaternary, where rocks units, Triassic, Jurassic, and Cretaceous in age, subcrop at various location within the western Barents sea (See Figure 3.2) (Henriksen et al., 2011b).

Chapter 4

Methodology

A new method that allows for estimating net exhumation magnitudes in sedimentary basin areas is introduced. The method is compaction-based, and uses traveltime data starting from the seabed, from a reference, normally-compacted non-uplifted area, and from an area suspected to be uplifted. The present study can be subdivided in three main steps: First, development the workflow that allows for the estimation of net exhumation magnitudes from traveltime data, and calibration of the technique with synthetic exhumation examples. Second, application of the method on a real case example where net exhumation magnitudes are estimated at nine locations across the Western Barents Sea. Lastly, modelling of mechanical and chemical compaction in clean sand formations from the locations studied, where input burial history curves are constructed based on the estimated net exhumation magnitudes. The last step is performed as a quality control procedure, with the aim of investigating whether the net uplift estimates can explain published quartz cement volumes observed in thin sections petrographical analysis, and petrophysical properties measured at well locations.

4.1 Data and Software

The present study was carried out using Matlab R2016A, which is a programming platform, that allows for numerical computation, data analysis, visualization and algorithm development, etc. Ray Tracing scripts from CREWES Matlab Toolbox, by Gary Margrave, were used.

The study used wireline well log data from one well in Norwegian Sea, two wells in the Norwegian North Sea, and nine wells spread across the Western Barents Sea. Generally, the well log data used comprised Gamma-ray, sonic interval transit time, bulk density, hole

size, neutron, and for some wells, shear wave interval transit times. Figure 4.1 shows the location of the well log data used in this study.

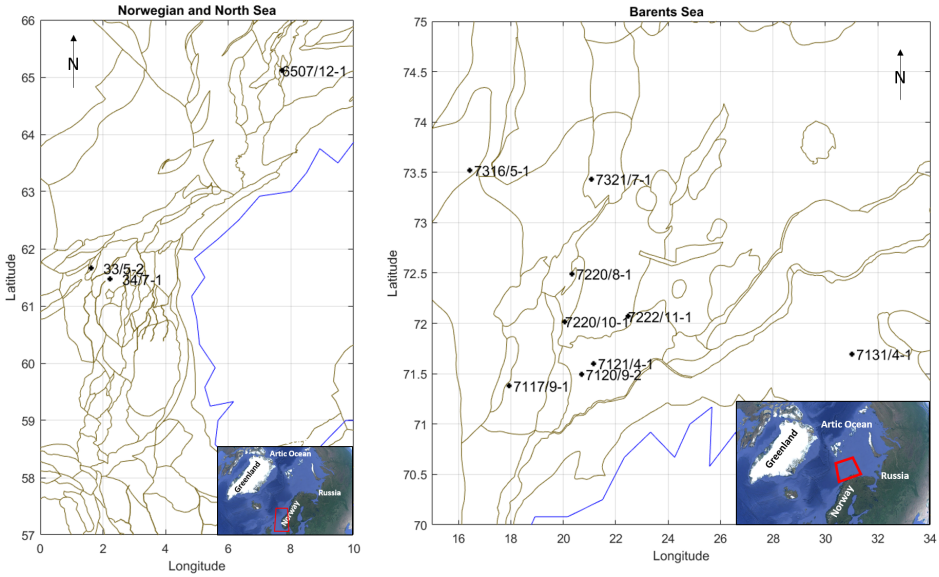

Figure 4.1: Location of the well log data used in the present study. Both data from the Norwegian Sea, Northern North Sea, and Barents Sea have been used. Coastline is depicted in blue.

4.2 The Net Exhumation Estimation method

The net exhumation estimation technique proposed in this study, in short, consists on estimating linear P-wave velocity functions from seismic traveltimes on a reference un-exhumed area, and on an area suspected to be uplifted. The areas, or the stratigraphic sequences in both areas, have previously been proven to be equal or comparable according to some predefined criteria. Later, the magnitude of net uplift is computed as the vertical depth difference between the two linear velocity trends. The procedure is thus repeated in a depth dependent scheme, where the thickness of the input reference area is increased at each step. In this section, a complete review of the uplift estimation technique will be presented, starting by a description of the procedure applied to estimate the linear P-wave velocity functions, explaining the criteria under which the two effective lithological columns are considered comparable, and revealing the technical details of how the uplift measurement is produced.

4.2.1 Estimation of Linear P-wave velocity functions from large-offset PP seismic traveltimes

Ray Tracing

It is important to mention, that the method to be introduced uses seismic traveltimes as input. The latter can be mapped from e.g. seismic data, or by ray tracing through well log P-wave velocity data. The examples presented in the present study uses traveltime mapped through isotropic ray tracing on well log velocity data. Prior to the ray racing, P- and S-wave velocity logs were upscaled by means of the Backus (1962) average. This was done to simulate wave propagation at seismic frequencies. For a average sedimentary rock velocity of 3000 m/s, and a wavelet frequency of 20 Hz (considering the attenuation of high frequencies with increasing depth), the correspondent wavelength is 150 m. Thus, the vertical seismic resolution given by a quarter or the propagated seismic wavelength is 37.5 m. Therefore, the Backus average was performed on 40 m thick intervals (Figure 4.2).

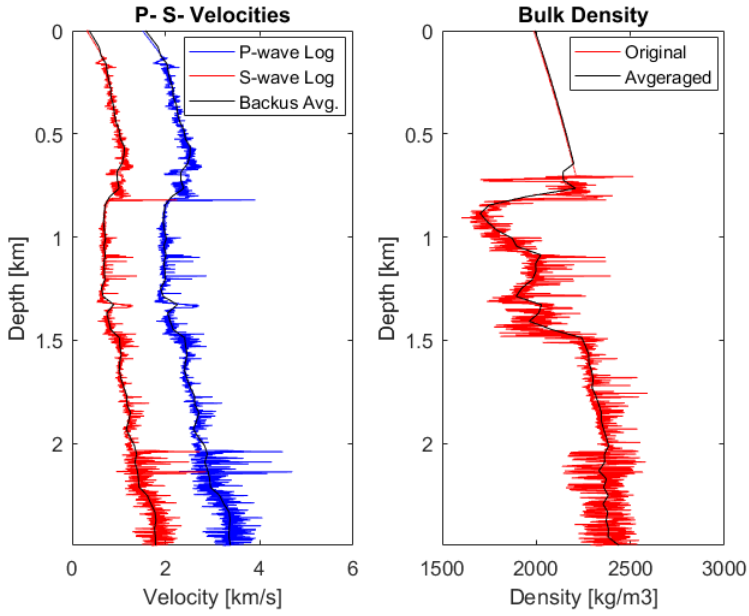

Figure 4.2: Backus average of P-wave velocity, S-wave velocity, and bulk density logs prior to ray tracing in 40 m thick intervals. Note the large velocity variations at well log frequencies.

With the upscaled P-wave velocity log, ray tracing was performed to produce PP seismic traveltime curves for the reference well (Figure 4.3). The ray tracer was provided by the CREWES matlab toolbox (Margrave, 2000). At each reflection depth Z_j, the maximum offset X_{max_j} was selected to be 2.5 times the depth of the reflector, to ensure the

large-offset condition required by Stovas and Ursin (2007) formulation.The receiver spacing was kept at 10 m to ensure enough sampling and ease the velocity analysis.

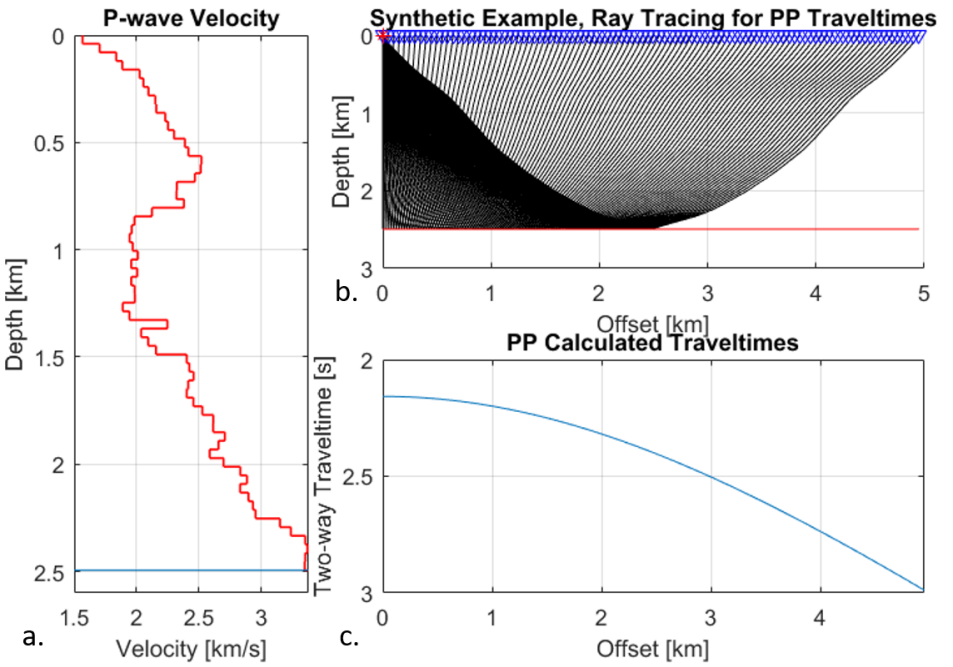

Figure 4.3: Ray tracing example. a) Input velocity model. Reflection depth is shown in blue. b) Fan of rays are shot and propagated through the input model, and reflected back at the selected depth. c) Resultant PP traveltime curve.

Velocity analysis

The procedure explained above can be repeated for each depth point within the input model and traveltime curves can be generated for the top and bottom of each layer. Thus, velocity analysis can be performed on each reflection curve in the model to obtain the effective NMO parameters down to each reflection time. The procedure can be divided in four steps: 1) Polynomial fitting on the measured traveltime curves to obtain an initial guess of the NMO velocity V_{nmo}, and zero-offset two-way traveltime T_0. 2) Traveltime modelling using Ursin and Stovas (2006) three-term approximation (Eq. (2.7)), using the initial guess of T_0 and V_{nmo}, and assuming the heterogeneity coefficient S to be 1. 3) Computation of the differences between the observed traveltimes T_{obs} and modelled traveltimes T_{mod} in a least square sense:

$$f = \sum \left[T_{obs} - T_{mod}\right]^2 \tag{4.1}$$

4) Minimization of the function above using MATLAB algorithm for unconstrained non-linear inversion. The latter is based on the Nelder-Mead minimization method.

Computation of Layer parameters and Heterogeneity

The velocity analysis provided effective NMO parameters. The latter serves as input for Stovas and Ursin (2007) formulation, and the velocity at the top of the layer $Vp0$, the P-wave velocity gradient β_p, and the layer thickness H can be computed using Equations (2.4), (2.5) and (2.6), respectively. A linear P-wave velocity that explains the seismic traveltimes through the input model can then be estimated, as shown in Figure 4.4a.

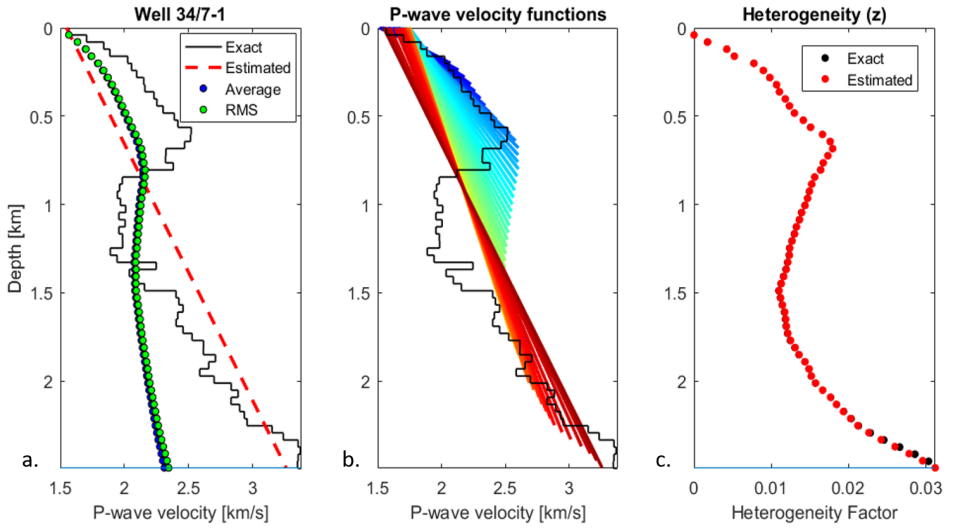

Figure 4.4: a) Backus-averaged P-wave velocity profile for the reference well 34/7-1 in the North Sea (in Black) and the P-wave velocity function estimated for the model (in Red). Calculated average and RMS velocities are also displayed. b) P-wave velocity functions estimated down to each depth in the input model. Color ranges from blue to red as the thickness of the column examined by the P-wave function increases. c) Heterogeneity factor g as a function of depth computed from: traveltimes (Red) and from known depth model (Black). Note how g is correlated with the velocity variations in the interval velocity.

Note that the method itself allows for the transformation from depth to time, as the layer thickness is one of the output of (Ursin and Stovas, 2006) formulation. The calculation can be extended for all times in the input model, and P-wave linear functions can be estimated down to each depth as shown in Figure 4.4b. In this case, the color of each line is associated to the thickness of layer through which the function explains the traveltimes. The first layer of the model is described by a blue line, and varies from blue to red, as the thickness of the column increases.

The procedure described above was followed by computation of the common velocity types used in exploration seismology. Interval two-way transit time Δt_0 and interval velocities V_{int} were calculated through the well known Dix (1955) equations. The latter uses as input the effective zero offset two-way traveltime and the NMO velocities estimated at the top and bottom of each layer. The average velocity V_{avg}, at all depths, was calculated from the interval velocity using Equation (2.9), as shown in Figure 4.4a. Since the model in question comprises horizontal layers, the RMS velocity V_{rms} can be approximated as the NMO velocity. However, it can also be calculated using Equation (2.10).

The average and the RMS velocities were then combined to compute Al-Chalabi. (1974) Heterogeneity Factor g (Eq. (2.13)) for all depths in the model, as shown in Figure 4.4b. Note that, in well log data examples, the interval velocity is known, and the NMO parameters can be computed through analytical equations. However, the methodology presented here is formulated assuming that the depth model is unknown, and that the seismic traveltimes is the only input information. Figure 4.4c depicts two dotted curves, which overlaps through almost the entire depth interval. The red circles, represents the heterogeneity factor computed from time parameters (i.e. from the NMO parameters produced in the velocity analysis). The black dots, represents the heterogeneity derived from calculations based on the input depth model. This step was done to verify the quality of the velocity analysis, and to ensure that the heterogeneity estimated from time parameters was close to the true value. Note how g is closely correlated with the velocity variations that the model exhibits with increasing burial depth. This is expected since the g is a measure of the velocity heterogeneity in the ground.

4.2.2 Net exhumation estimation for a single reference depth

In order to evaluate the methodology presented, a synthetic net exhumation example was performed. The example consisted in lifting up a selected reference well column, and eroding away the layers that were displaced above the initial depth of the seabed. A schematic representation of the procedure applied on well 34/7-1 from the Northern North Sea is shown in Figure 4.5. The synthetic exhumation example allows for generating the conditions expected to be observed on real case examples. Moreover, it allows for estimating the exhumation magnitude in a controlled scenario where the magnitude of uplift and erosion is known in advance.

The shale compaction depth-trend technique is based upon the assumption that two homogeneous shale formations, with similar acoustic properties are found in a reference unexhumed area, and in an area that has presumably been uplifted. Analogously to the shale compaction technique, in this method, we consider the composite stratigraphic sequences from reference and uplifted area as effective media, and their similarity is evaluated in terms of their NMO parameters and velocity heterogeneity.

Consider a reference depth Z_1 selected in the unexhumed area, for instance at 2.37 km depth. Thus, the NMO parameters T_{0_1}, V_{nmo_1}, S_1, and the heterogeneity factor g_1 can be

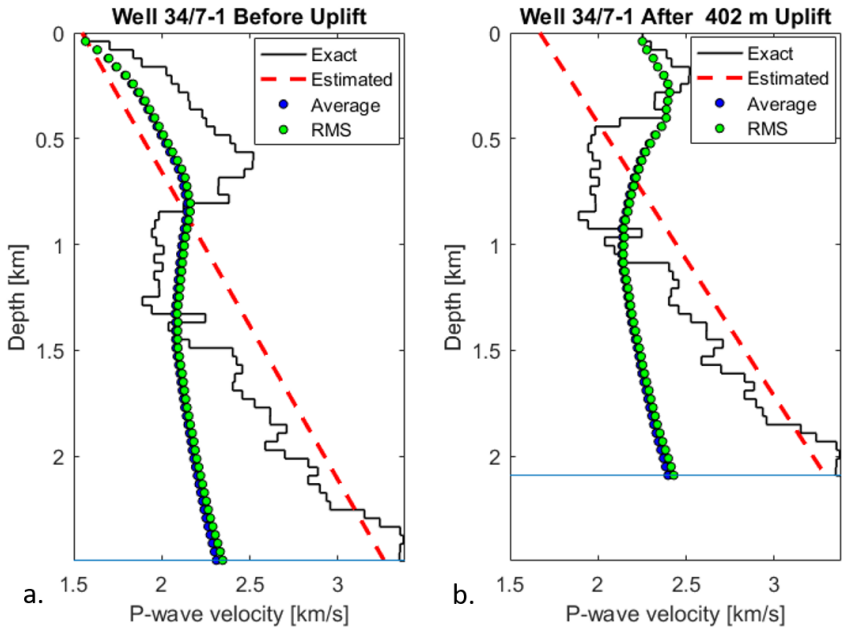

Figure 4.5: Synthetic uplift and erosion example: a) Well 34/7-1 prior to exhumation. b) Well 34/7-1 after 402 m uplift and erosion.

computed, together with the pair $[Vp_{0_1}, K_1]$, that forms the linear P-wave velocity function that explains the traveltimes down to Z_1 (Black curve, in Figure 4.6). By performing velocity analysis on all reflections in the uplifted well, NMO parameters can be estimated down to each interface, as shown in Figure 4.7. A search through the NMO velocity in the uplifted well can be performed until a value V_{nmo_2} equal or closest to V_{nmo_1} is found at a certain depth.

Now, the procedure can be repeated for the other criteria parameters T_0, S and g. This would provide a total of four linear functions defined by the four pairs $[Vp_{0_2T_0}, K_{2T_0}]$, $[Vp_{0_2V_{nmo}}, K_{2V_{nmo}}]$, $[Vp_{0_2S}, K_{2S}]$, and $[Vp_{0_2g}, K_{2g}]$ as shown in Figure 4.6.

As previously addressed, from the shale compaction technique, the vertical difference between the compaction curve, in this case, the linear P-wave functions in the reference and uplifted areas yields the net uplift magnitude. However, the gradients of the velocity functions in reference and uplifted areas will generally be different. Hence, the uplift provided by a given criteria is computed by averaging the vertical differences at the upper and lower ends of the curves as shown in Figure 4.6. The estimated linear function for a given criteria evaluated at the depth of equality $Vpl_2(Z_{2crit})$ might be lower or higher than the velocity of the reference function at the reference depth $Vpl_1(Z_1)$. Thus, the reference curve is extrapolated or contracted prior to the averaging as depicted by Figure 4.6. Lastly, the mean of the four exhumation estimates yields the amount of net exhumation for the given reference depth.

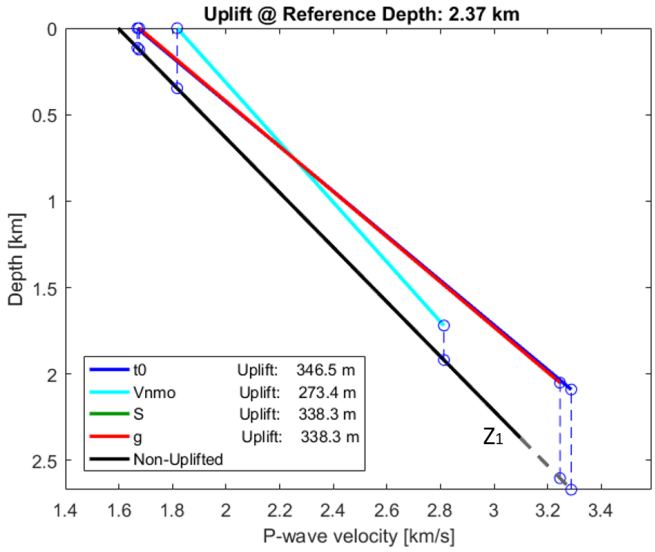

Figure 4.6: P-wave linear velocity functions estimated for each criteria parameter. Note that S function is equal to and overlapped by the g function. For each criteria, the uplift is computed by averaging the vertical differences between uplifted and reference curves at the upper and lower ends.Extrapolation of the reference function is shown in gray.

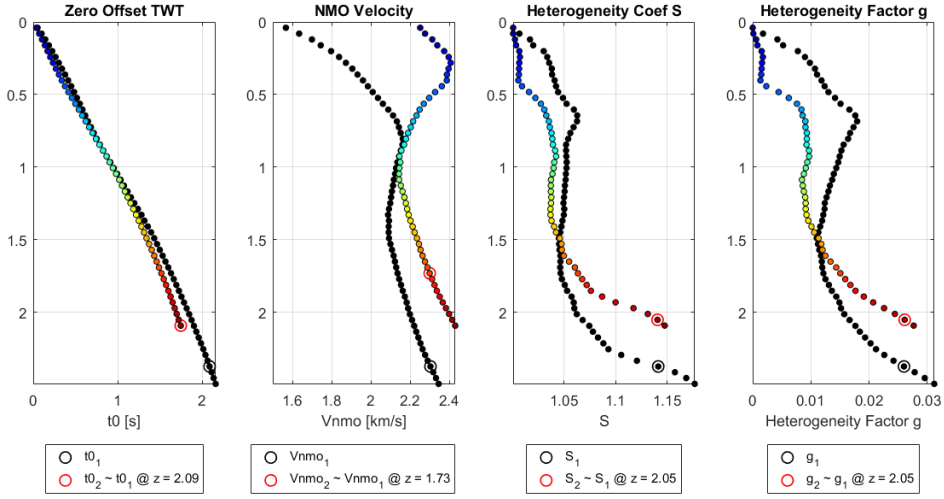

Figure 4.7: Parameter criteria for reference (in Filled-Black) and uplifted (Filled-Coloured) areas as a function of depth. Reference depth Z_1 is located at 2.37 km (Black non-filled circle). The uplifted parameters are color coded by burial depth from no burial (in Blue), to the bottom of the uplifted model (in Red). The depth of equality for each parameter in the uplifted well is depicted by the red non-filled circles.

4.2.3 Net exhumation estimation for multi-reference depth

The methodology discussed above is repeated for each depth in the reference area, producing the net exhumation curves shown in Figure 4.8. For shallow depths, the procedure is rather unstable. As the method examines deeper depths, and the P-wave functions are estimated for thicker lithological columns, the net exhumation magnitude increases and method becomes stable (A more detailed discussion is presented in the results and discussion chapters). The yellow triangle located close to 2 km depth depicts the stabilization depth, given by the maximum of the T_0 uplift curve. The second yellow triangle at around 2.4 km depth represents the deepest depth point at which equal heterogeneity is found.

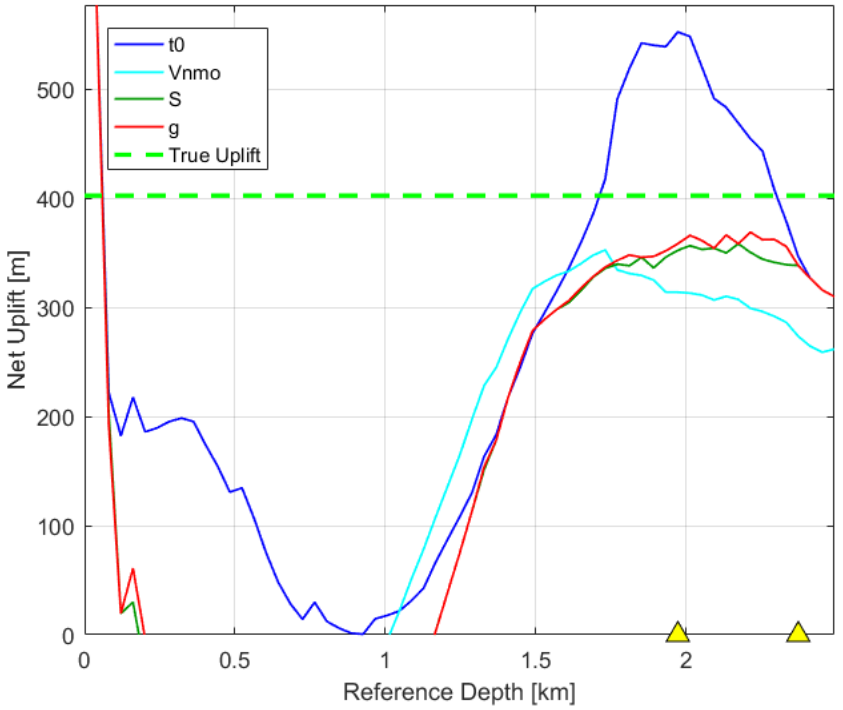

Figure 4.8: Net exhumation magnitude as a function of reference depth. The stabilization depth is given by the maximum of the T_0 uplift curve (Yellow triangle at 1.9 km depth). The yellow triangle at around 2.4 km depth depicts the last depth where equal heterogeneity is found.

A simple statistical analysis can be performed including all the samples from all the uplift curves within the two yellow triangles, yielding the uplift chart presented in Figure 4.9. The method predicts a mean exhumation value of 368 with a standard deviation of 68 m. The true magnitude of exhumation is our controlled exhumation example is 402 m. The true uplift magnitude is close to mean estimated magnitude and within the range of uncertainty provided by the standard deviation.

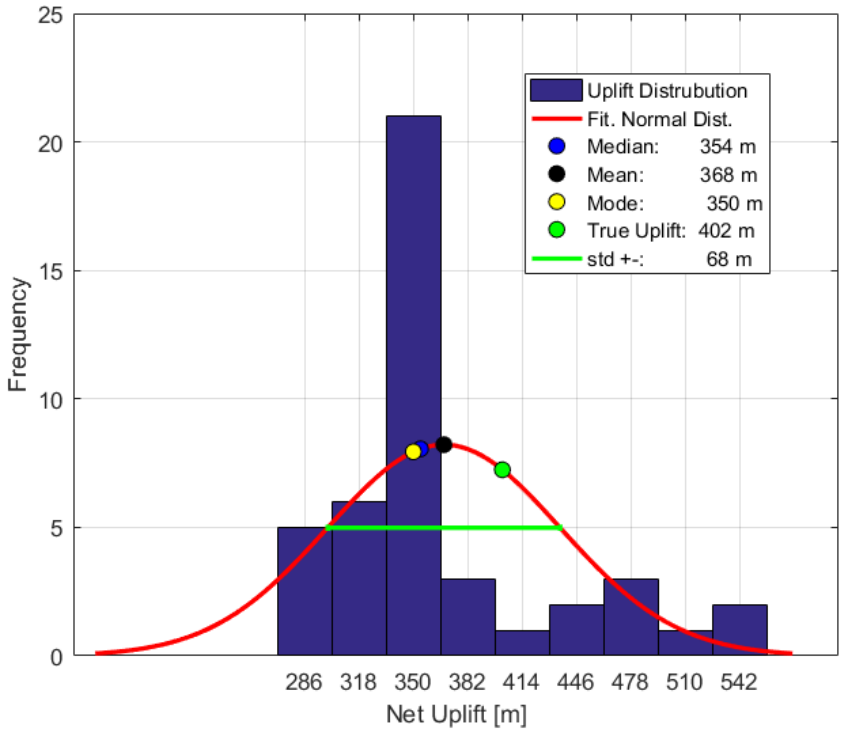

Figure 4.9: Uplift estimation statistics. The mean, median, mode, and standard deviation are computed from simple statistical analysis of the selected samples. The true magnitude of uplift is within the range of uncertainty provided by the standard deviation.

It is important to mention that the net exhumation magnitude is selected to be the mean of the studied samples, and not other statistical parameter as median or mode. The uplift curve for a given parameter can flatten out at a particular exhumation magnitude different from the true magnitude. This is the case for S and g in this particular example. This flattening result in increased frequency count for a given uplift magnitude, and therefore controls the mode. On the other hand, the median is less influenced by the criteria that differ the most from the mean value. As observed in a variety of synthetic uplift estimation examples, the criteria exhibiting the largest differences from the mean estimate might provide the closest estimate to the true uplift magnitude. Thus, the magnitude of net exhumation is considered to given be mean of the selected samples, which treats the contribution of the uplift curves from all criteria, equally.

4.3 Burial History Modelling

The net exhumation estimates obtained from the presented methodology were used as input for the generation of burial history curves that simulates the burial of the sediments through time, from the age of deposition, until the present day. This allows for understanding the mechanical and thermal history of the sediments, and serves as input for models that simulates mechanical and chemical compaction in clean sandstones. The aim is to evaluate whether the modelling can explain the quartz cement volumes quantified on thin section petrographical analysis, and whether the porosity, elastic parameters and velocities measured at well locations, can be predicted. This allows for quality controlling the uplift estimates produced with the method.

The burial history was reconstructed for clean sandstones located within the nine Barents Sea wells for which net exhumation estimates were produced. The sandstones were located within various formations as Stø, Fruholmen, Tubåen and Snadd. For a selected formation, at a given well location, only samples with clay volumes lower than 5% were used in the modelling. The methodology followed for the burial history modelling is based on Blazevic (2017) work, where porosity and velocities were modelled for clean sandstones from unexhumed areas within the Norwegian and North Sea.

Depending upon the availability of data at a given well location, and for a particular formation, each modelling problem had to be approached differently. The methodology described below represents the general workflow followed for the burial history modelling, and technical details related to the modelling of a specific well or formation are not provided on this section.

4.3.1 Porosity and Clay Volume calculation

The majority of the wireline well log data acquired in the North, Norwegian, and Barents Sea, are calibrated to limestone matrix. This means that the neutron porosity yields the true porosity only in clean limestones. Thus, the neutron porosity logs were corrected for sandstone lithology before further calculations, using a digitized version of (Por-11) calibration chart from Schlumberger (2009). Density porosity ϕ_D was calculated as:

$$\phi_D = \frac{\rho_{ma} - \rho_b}{\rho_{ma} - \rho_{fl}} \tag{4.2}$$

where ρ_{ma} is the matrix density assumed to be equal to the density of pure quartz (2.65 g/cm^3); ρ_{fl} is the fluid density, assumed to be water with density of 1.03 g/cm^3; and ρ_b is the bulk density as read from the log. The porosity ϕ was then computed by combining the sandstone calibrated, neutron porosity ϕ_N, and the density porosity ϕ_D as:

$$\phi = \sqrt{\frac{\phi_N^2 + \phi_D^2}{2}} \tag{4.3}$$

Equation (4.3) yields a good approximation of porosity in gas saturated rocks, which the hydrocarbon phase present in the hydrocarbon bearing sands analyzed in the present study. Moreover, since the present study focuses on clean sandstones, porosity is equal or very close to the effective porosity.

The clay volume was estimated as the average of the clay volumes estimated from the gamma ray log, and from the neutron-density logs. The Gamma ray clay volume is computed as:

$$V_{Cl_{GR}} = \frac{GR_{log} - GR_{min}}{GR_{max} - GR_{min}} \tag{4.4}$$

where GR_{log} is the gamma-ray log reading at the interval of interest; GR_{min} is the gamma ray log reading in a clean zone having no clay; and GR_{max} is the gamma ray log reading in a 100% clay depth interval. The neutron-density shale volumes are computed from the separation between the neutron and density porosity log curves as:

$$V_{Cl_{N-D}} = \frac{\phi_N - \phi_D}{\phi_{N_{Cl}} - \phi_{D_{Cl}}} \tag{4.5}$$

where, ϕ_N is the sandstone calibrated neutron porosity, ϕ_D is the density porosity; $\phi_{N_{Cl}}$ is the neutron porosity reading in a clay, set to 0.40; and $\phi_{D_{Cl}}$ is the density porosity reading in a clay, set to 0. For a selected formation, within a given well location, only clean sandstones with less than 5% clay volume are used further for the burial history modelling.

4.3.2 Pressure and Temperature Calculation

The temperature-depth function at a given well location was calculated by performing a linear interpolation between the temperature at the sea bottom T_{seabed} (4 °C), and the bottom hole temperature (BHT):

$$T(z) = T_{seabed} + \frac{BHT - T_{seabed}}{TVD_{Kb} - WD_{Kb}} z \tag{4.6}$$

where TVD_{Kb} and WD_{Kb} refers to the total vertical depth, and the water depth, measured with respect to the Kelly bushing.

At a sedimentary basin area, where rocks are located at their maximum burial depth, mechanical compaction can be modelled based on the in-situ differential stress field. The differential stress is computed as the difference between the lithostatic pressure σ_{lith} and the pore fluid pressure σ_{fl}. The first is given by the weight of the rock column above a certain depth Z, and is computed as:

$$\sigma_{lith}(Z) = g \int_0^Z \rho_b(z) dz \tag{4.7}$$

where g is the gravity constant, and $\rho_b(z)$ is the bulk density at a given depth z. Similarly, under hydrostatic pressure conditions the pore pressure can be computed as:

$$\sigma_{fl}(Z) = g \int_0^Z \rho_{fl}(z) dz \tag{4.8}$$

where, $\rho_{fl}(z)$ is the fluid density at a given depth z. However, at exhumed areas within a sedimentary basin, shallow low density sediments have been eroded away and the present-day differential stress gradient is expected to be higher compared to the paleo-differential-stress gradient under which the rocks were mechanically compacted (See Figure 4.10). Therefore, to simulate paleo-stress conditions, a differential stress gradient of 10 MPa/km

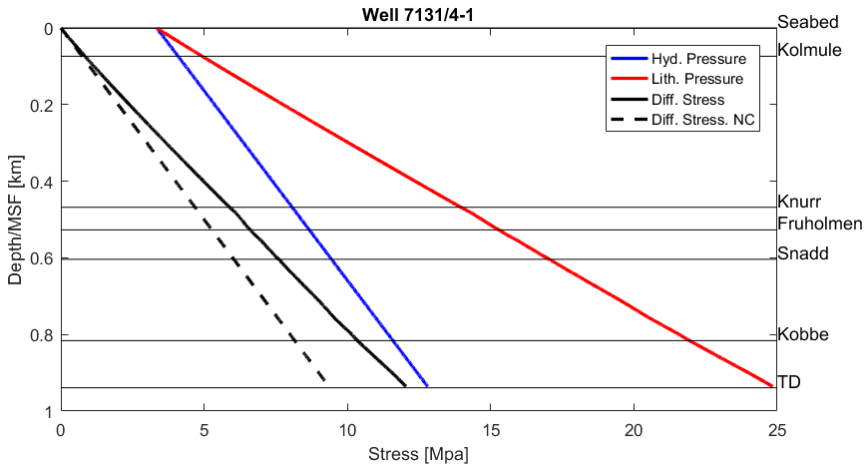

Figure 4.10: Differential Stress at well 7131/4-1 (Black). Lithostatic stress and hydrostatic pressure are depicted in red and blue, respectively. Note how the in-situ differential stress exhibit higher gradient compared to a pressure gradient of 10 MPa/km, which is commonly observed in normally compacted unexhumed areas from the Norwegian and North Sea basins.

was selected. Such a pressure gradient is generally observed in normally compacted-unexhumed areas from the Norwegian and North Sea.

4.3.3 Burial history curves

Burial history curves were constructed to establish the temperature-depth-time relationship under which sediments have been compacted. The depositional age of the base of each layer was established based on three sources of information: 1) Published chronostragraphic charts derived for specific areas within the Barents Sea, 2) Chronostratigraphic data gathered from well completion reports, 3) Published Burial history curves for a given formation, at a particular well location within the Barents Sea.

For each formation, deposition was modelled to occur at constant burial rate, depending upon the thickness of the formation and the depositional ages at the top and base. The thickness of each formation deposited is assumed to be equal to the present day thickness, except for the formation whose volumes have been eroded as consequence of the Late Cenozoic exhumation episode. For the eroded formation, the thickness prior to exhumation ΔZ, is given by:

$$\Delta Z = \Delta Z_{t=0} + NetExhumationEstimate \tag{4.9}$$

where $\Delta Z_{t=0}$ is the present day thickness. Zattin et al. (2016) carried out an integrated study using Apatite (U-Th)/He thermocronology data, and vitrinite reflectance data, and presented a burial history curve for various formations at a specific location within the Barents Sea. The age of maximum burial depth was selected to be 13 Ma. as suggested by their study.

An example of the burial curve constructed for well 7131/4-1 is shown in Figure 4.11. Since the modelling is aimed to be evaluated in terms of the net exhumation estimates, gross exhumation and post-exhumation re-burial are not considered in the construction of the burial curves.

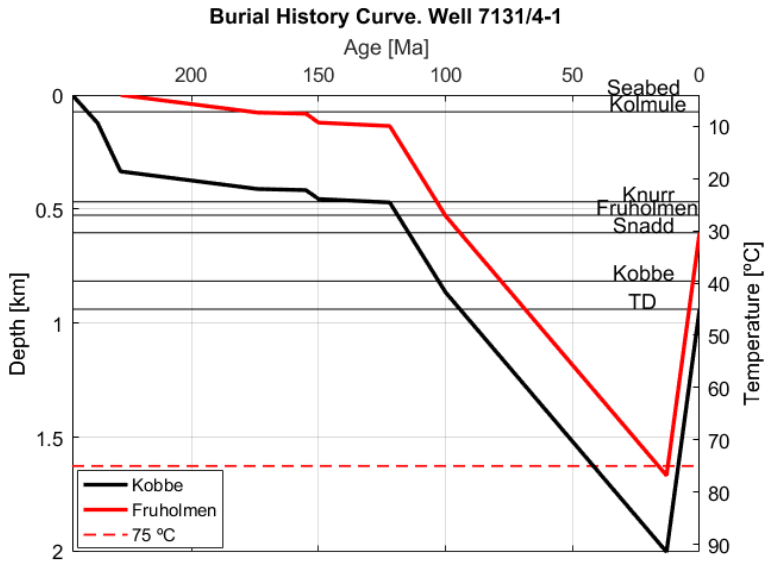

Figure 4.11: Burial History Curve for the base of Fruholmen Fm. at Well 7131/4-1 in the Barents Sea (in Whole Red). The tops depicted on the right refers to present day depth tops. The base of the model, Base Kobbe, is shown as reference (in Black). See how the base Fruholmen enters the Quartz Cementation window for a very short time period. The rocks reached maximum burial depth at 13 Ma according to Zattin et al. (2016).

4.3.4 In-situ properties of the pore fluid: Density and Elastic Moduli

To perform a sensitive comparison between the petrophysical properties measured at well location, and the properties modelled in the present study, an accurate prediction of the fluid properties is mandatory. The aim is to estimate the in-situ fluid properties, and to perform later a fluid substitution to the brine saturated scenario. The latter ensures that the comparison is performed in a scheme where observed and modelled rock properties respond to the same pore fluid, i.e. brine.

The elastic moduli and density of the pore fluids in the selected clean sandstones were estimated using Batzle and Wang (1992) equations. This equations require various inputs depending upon the fluid to be modelled. In general, it requires the pressure of the fluid in the formation and the temperature. An additional property related to the type of fluid is also required, i.e. the salinity, in the case of brine; the specific gravity, for gases; and the specific gravity of the gas and the gas oil ratio, for oil. Oil saturated formations were not modelled in this study. For gas saturated formations, the specific gravity were selected from measured values, presented at well completion reports. For water saturated formations, the salinity was estimated based on: 1) Values provided on well completion reports, or 2) Calculated from the resistivity of brine-saturated clean sandstone formations using the Picket plot. Generally, completion reports were not available for the majority of the wells studied, thus, case 2) was the common scenario. An example of the water resistivity estimation using the Picket Plot is shown in Figure 4.12.

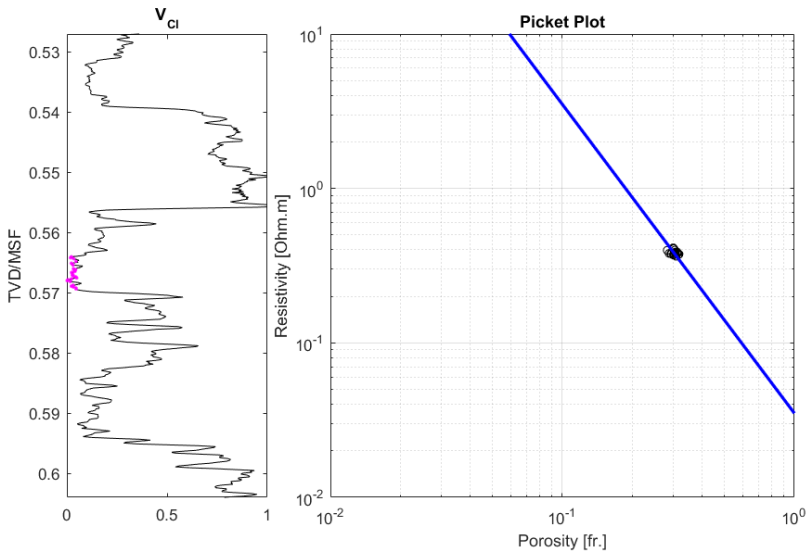

Figure 4.12: Water resistivity estimation for well 7131/4-1 using Picket Plot. Left: V_{Clay} plot depicting the cleanest Sands within the Fruholmen Fm. (Magenta points). Right: Picket Plot using the cleanest water-saturated sandstone samples shown in the left plot.

When the pore fluid comprised two phases the effective bulk moduli of the pore fluid K_{fl} was estimated using the Reuss or Isostrain average (Mavko et al., 2009):

$$\frac{1}{K_{fl}} = \sum_{i=1}^{N} \frac{f_i}{K_i} \tag{4.10}$$

where N represents the number of fluid phases, i is the subscript referring to a given fluid phase, f_i is given by the water saturation in the pore space S_w, and K_i is the bulk moduli of the fluid i. The water saturation was estimated using the well known Archie et al. (1942) equations. Note that, since fluids do not support shear, the P-wave moduli of the fluid M_{fl} is equal to the calculated K_{fl}. Similarly, the effective density of the fluid in-situ ρ_{fl} was estimated as:

$$\rho_{fl} = S_w \rho_{brine} + (1 - S_w)\rho_{gas} \tag{4.11}$$

where, ρ_{brine} and ρ_{gas} refers to the estimated brine and gas densities, respectively.

4.3.5 Dry Elastic Moduli, and P-wave and S-wave Velocity calculation

The P-wave modulus of the clean sand samples saturated with the in-situ fluids M_{sat_1}, was calculated from the bulk density ρ_b and the in-situ P-wave velocity V_p as:

$$M_{sat_1} = \rho_b V_p^2 \tag{4.12}$$

M_{sat_1} was combined with the porosity, the estimated P-wave modulus of the effective in-situ fluid M_{fl}, and the P-wave modulus of the solid grains M_o, into the Gassmann (1951); Biot (1956) Equations, to compute the P-wave moduli of the dry rocks M_{dry}. Since only clean sand samples are selected, M_o was selected to be 95.66 GPa as reported by Mavko et al. (2009) for pure quartz.

Similarly, the brine saturated P-wave modulus M_{sat_2}, was estimated by fluid substituting from the dry rock scenario to the brine saturated scenario using Gassmann (1951); Biot (1956) relations. The bulk density of the the brine saturated rocks ρ_{sat_2}, was calculated from the quartz density ρ_{ma}, and the brine density ρ_{brine} as:

$$\rho_{sat_2} = (1 - \phi)\rho_{ma} + \phi\rho_{brine} \tag{4.13}$$

Later, the P-wave velocity of the brine saturated rocks Vp_{sat_2} was computed from M_{sat_2} and ρ_{sat_2} as:

$$Vp_{sat_2} = \sqrt{\frac{M_{sat_2}}{\rho_{sat_2}}} \tag{4.14}$$

When shear wave transit time logs were not available, the brine saturated S-wave velocity Vs_{sat_2} was estimated from Vp_{sat_2}, and the estimated clay volume, using Greenberg

and Castagna (1992) equations. Then, the shear modulus of the brine saturated rock μ_{sat_2} was calculated from ρ_{sat_2} and the estimated S-wave velocity as:

$$\mu_{sat_2} = \rho_{sat_2} V s^2_{sat_2} \tag{4.15}$$

Note that, since fluids do not support shear deformation, the S-wave modulus of the rock saturated with any fluid is the same to the shear modulus of the dry rock. However, following (Blazevic, 2017) workflow, when S-wave velocity measurements were available, the shear modulus was computed directly by the taking the product of the bulk density and the the S-wave velocity squared. Lastly, the dry bulk modulus was computed as:

$$K_{dry} = M_{dry} - \frac{4}{3}\mu \tag{4.16}$$

4.3.6 Mechanical Compaction Modelling

The loss of porosity with increasing burial depth was modelled in terms of the loss of intergranular volume with increasing differential stress using Lander and Walderhaug (1999) mechanical compaction model (Equation (2.14)). The mapping from differential stress to depth was performed by using the previously established pressure-depth relation for a normally compacted basin (10 MPa/km). Figure 4.13 shows the decrease in porosity with increasing burial depth and differential stress, for the Fruholmen Fm. at well 7131/4-1. The porosity decreases from a depositional porosity of 0.40, down to the porosity at the onset of quartz cementation.

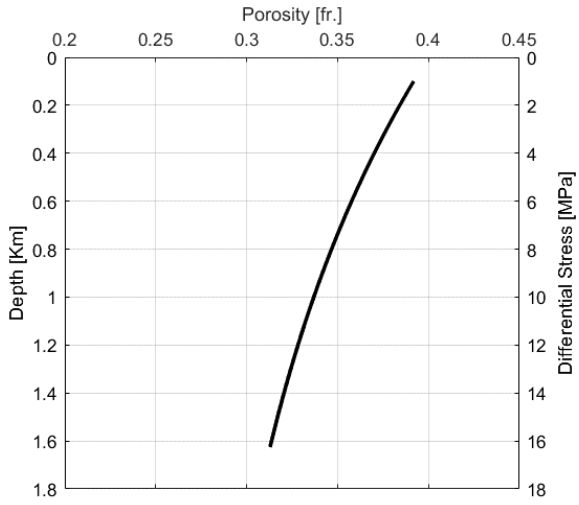

Figure 4.13: Simulation of mechanical compaction for clean sands within the Fruholmen Formation at well 7131/4-1 using Lander and Walderhaug (1999). The mapping from stress to depth was performed based on the previously established pressured-depth relation.

Table 4.1 summarizes the model parameters chosen for mechanical compaction modelling of the selected formation at each well location. The rate of intergranular volume

Table 4.1: Mechanical Compaction parameter selection for the sandstone formations modelled at each well location. A value of $\beta = 0.06$ was used in the modelling of all formations. ϕ_0 and m_o, were deduced from information regarding the degree of sorting and the volume of clay, respectively, found in petrographical thin section analysis reports and well completion reports. IGV_f was empirically calibrated using values between 0.24 and 0.28.

Well and Fm.	$\phi_o[fr.]$	$m_o[fr.]$	$IGV_f[fr.]$
7117/9-1 Torsk Sand	0.40	0.04	0.28
7120/9-2 Stø	0.38	0.00	0.24
7121/4-1 Stø	0.40	0.00	0.24
7131/4-1 Fruholmen	0.40	0.00	0.26
7220/8-1 Tubåen	0.38	0.02	0.28
7220/10-1 Stø	0.36	0.00	0.26
7222/11-1 Snadd	0.38	0.02	0.26
7316/5-1 Torsk Sand	0.40	0.04	0.28
7321/7-1 Stø	0.38	0.00	0.26

decline with effective stress β, was selected to be 0.06. This was done because there is enough empirical evidence that support the insensitivity of β to sandstone composition, with some exceptions of large amounts of highly ductile grains (Lander and Walderhaug, 1999). The depositional porosity ϕ_o was adjusted between 0.36 and 0.40 depending upon the degree of sorting that the sands exhibit according to published petrographical thin section analysis for the sands in question. Similarly, the initial proportion of matrix material m_o, was deduced from information found on petrographical reports and well completion reports. The most uncertain parameter is the stable packing configuration IGV_f. The latter was calibrated for the specific sandstone formations as suggested by Lander and Walderhaug (1999), using values between 0.24 and 0.28.

4.3.7 Chemical Compaction Modelling

The porosity loss as a consequence of quartz cementation was simulated by means of Walderhaug (1996) quartz cementation model. Storvoll et al. (2005) suggested quartz cementation to start at around 70°C - 80°C. Thus, a mean value of 75°C was selected as the onset temperature for this study. Figure 4.14, depicts the modelling results for the Fruholmen Fm. at well 7131/4-1. In this case, the sands were modelled to have been exposed in the quartz cementation window for a very short time period (3.5 Ma) reaching a maximum temperature of nearly 77°C. Hence, only very few volumes of quartz were precipitated (0.3%), with an almost negligible reduction in quartz surface area, and with the porosity remaining nearly unchanged. However, the quartz cementation have a greater impact on the stiffness of the rock.

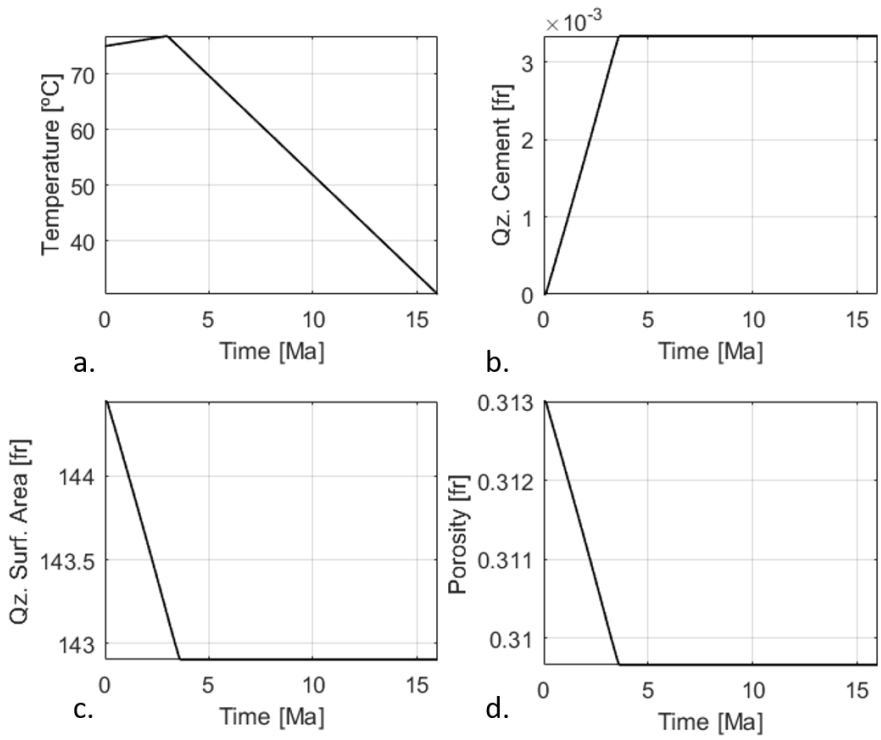

Figure 4.14: Simulation of Chemical compaction for clean sands within the Fruholmen Formation at well 7131/4-1 using Walderhaug (1996). a) Input temperature-time relationship based on the constructed burial history curve. b) Quartz cement volume precipitation as a function of time. c) Quartz surface area reduction as function of time. d) Porosity reduction due to quartz cement precipitation with time.

Table 4.2 summarizes the parameter selection for the chemical compaction modelling of the selected formation at each well location.

The grain size D, the detrital fraction of quartz f, and the clay coating factor C, were taken from published petrographical analysis performed on thin sections of the selected formations, at the given well location. When reports were not available, the values were assumed based on data from neighbour wells, average values for the given parameter in the present study, and the general lithological characteristics of the formation in question.

Table 4.2: Chemical Compaction parameter selection for the sandstone formations modelled at each well location. For some of the modelled formations, the chemical compaction parameters were taken from thin section petrographical analysis reports.
* From petrographical report:
Stø Fm. at 7121/4-1 (Mahmood, 2013)
Fruholmen Fm. at 7131/4-1 (Porten, 2012)
Snadd Fm. at 7222/11-1 (Porten, 2012; Gyenis, 2016)
! Report not found
- Chemical compaction not modelled

Well and Fm.	Grain size D [mm]	Detrital quartz f [fr.]	Clay coating Factor C [fr.]
7117/9-1 Torsk Sand	-	-	-
7120/9-2 Stø	0.10!	65!	0!
7121/4-1 Stø	0.18*	65*	0*
7131/4-1 Fruholmen	0.27 (0.17-0.30)*	65*	0*
7220/8-1 Tubåen	0.18!	55!	0!
7220/10-1 Stø	0.16!	65!	0!
7222/11-1 Snadd	0.14*	0.39*	0.9*
7316/5-1 Torsk Sand	-	-	-
7321/7-1 Stø	0.10!	61!	0!

4.3.8 Dry Elastic Moduli Modelling

The modelling of the dry elastic moduli of the rock can be summarized in three main steps:

a) *Computation of the Hertz-Mindlin elastic moduli* from Equations (2.21) and (2.22), using a coordination number N of 9, and a critical porosity ϕ_c of 0.36. The bulk and shear moduli of the solid grains were selected as the bulk and shear moduli of quartz, 37 GPa and 44 GPa, respectively (Values taken from Mavko et al. (2009)). When the grains exhibited important mineralogical variations, the elastic moduli of the solid grains were computed using the Voigt-Reuss-Hill average (See Mavko et al. (2009) for expression). Figure 4.15a shows the result of the Hertz-Mindlin moduli calculation. Differential pressure was varied from 1 MPa, up to the onset pressure P_{onset} (i.e. the pressure to which the rock is subjected when the quartz cementation temperature is reached). For the case shown in Figure 4.15, this is approximately 16 MPa.

b) *Computation of the dry elastic moduli in the mechanical compaction domain:* The Hertz-Mindlin elastic moduli equations are valid only at $\phi_c = 0.36$. To arrive at porosities higher than ϕ_c, the dry elastic moduli of the rock were calculated using the unconsolidated marine sediments model (UMS) of Dvorkin et al. (1999) (Eqs. (2.26) and (2.27)). For porosities lower than ϕ_c, down to the porosity at the onset of quartz cementation (ϕ_{onset}), the elastic moduli of the dry rock were calculated using the friable sand model (FS) of Dvorkin et al. (1999) (Eqs. (2.24) and (2.25)). Note that both models explain the variations in K_{dry} and G_{dry} with porosity, for a constant value of differential pressure. Figure 4.15b

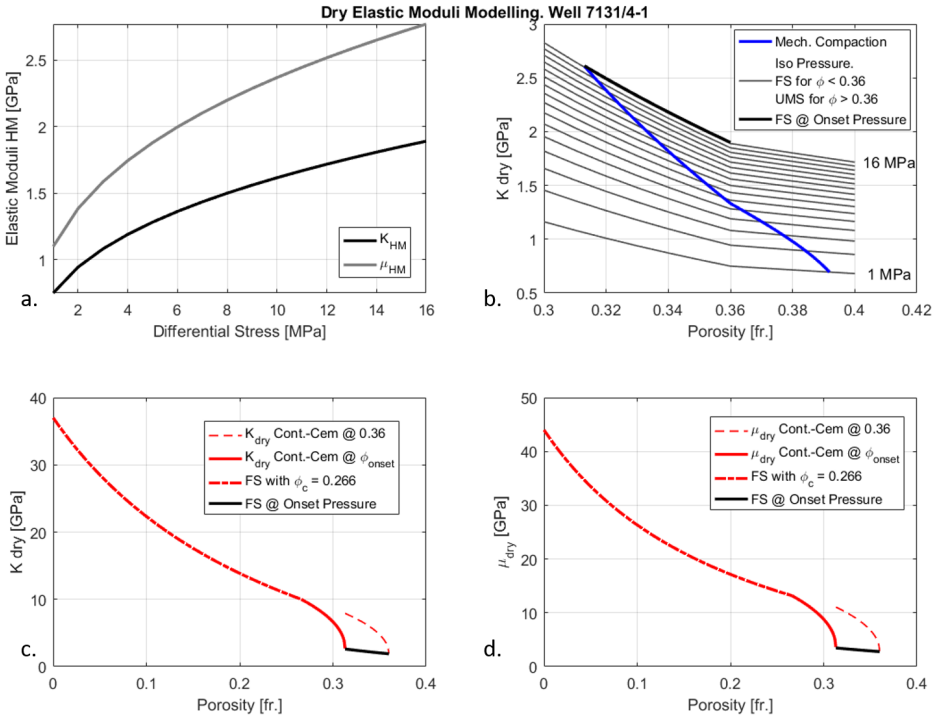

Figure 4.15: Dry elastic moduli modelling. a) Computation of the dry elastic moduli at $\phi_c = 0.36$. b) Computation of the dry bulk moduli at $\phi \neq 0.36$, using the unconsolidated marine sediments model (UMS) for $\phi > 0.36$ and the friable sand model (FS) for $\phi < 0.36$ (Iso-pressure lines in Gray). The stiffness of the rock in the mechanical compaction domain (in Blue), is computed by identifying the dry elastic moduli at a given porosity and at a particular differential stress, according to the mechanical compaction porosity-pressure relation. c) K_{dry} in the chemical compaction domain. d) μ_{dry} in the chemical compaction domain. Note how in c) and d) the Cont. Cem. model was shifted along the Friable sand model curve (in Black) to make quartz cementation start at the ϕ_{onset}. The stiffness increase due to continued quartz cementation is depicted in dotted-dashed red.

depicts the calculation of the dry-bulk modulus at differential pressures ranging from 1 MPa to P_{onset} (Iso pressure curves in Gray). The black curve refers to the friable sand model computed at P_{onset}. During burial differential stress increases, compacting the rock, and reducing its porosity. The stiffness increase during burial, until the onset of quartz cementation, was computed by identifying the dry elastic moduli at a given porosity and at a particular differential stress, according to the mechanical compaction porosity-stress relation, as shown in Figure 4.15b (in Blue).

c) *Computation of the elastic moduli of the rock in the chemical compaction domain:* The stiffness increase due precipitation of uniform layers of quartz cement in the surface of the grains was modelled by means of Dvorkin and Nur (1996) Contact-Cement Model (CC) (Eqs. (2.29) and (2.30)). This model is originally defined at 0.36 (Blazevic, 2017).

Thus, firstly, the model was applied at P_{onset} and at $\phi = \phi_c$, as shown in Figure 4.15c and 4.15d (in dashed Red). To take the model to start at ϕ_{onset}, the CC model was shifted along the Friable sand model curve (in Black). This was performed by introducing the calculated stiffness values in Equations (2.24) and (2.25) as K_{HM} and μHM, while varying ϕ_c from 0.36 down to ϕ_{onset} (Blazevic, 2017) (Figures 4.15c and 4.15d, in whole Red). Lastly, to describe the stiffness increase due to continued quartz cementation, the dry elastic moduli at the low porosity end of the CC model were introduced again in Friable sand model Eqs. (2.24) and (2.25), using a critical porosity of $\phi_{onset} - (\phi_{onset} - 0.36) = 0.266$ (See Figures 4.15c and 4.15d, in dashed-dotted Red).

Lastly, the P- and S-wave velocities for the 100% water saturation scenario were modelled. This required, first, performing Gassmann Fluid substitution on the modelled dry elastic moduli to achieve the brine saturated state. Then the brine saturated elastic moduli were combined with the brine saturated bulk density calculated from the modelled porosities.

Chapter 5

Results

The methodology tested and calibrated through synthetic exhumation examples is applied on a real case where the magnitude of net exhumation is estimated within nine wells across the Western Barents Sea. The estimates are produced using as reference, unexhumed wells from the Norwegian North Sea (33/5-2 and 34/7-1), and from the Norwegian Sea (6507/12-1). An overview of the location of the reference wells, and the wells for which net exhumation was estimated, can be observed in Figure 4.1. In the present chapter all depths are referred to mean sea bed, unless otherwise stated.

5.1 Net exhumation magnitude estimation

As explained in the methodology, for a given depth in the reference model, and for a given criterion parameter, the net exhumation is computed by averaging the vertical depth differences, at the upper and lower ends, between the P-wave velocity functions from uplifted and reference areas. This yields four exhumation estimates at the given depth, associated to each of the four criteria. The procedure is then repeated down to each depth in the reference model, producing four depth-varying uplift curves.

The results from applying the method on well 7220/8-1, drilled west of the Polheim Sub-platform and Loppa High, using well 33/5-2, as reference, is shown in Figure 5.1.

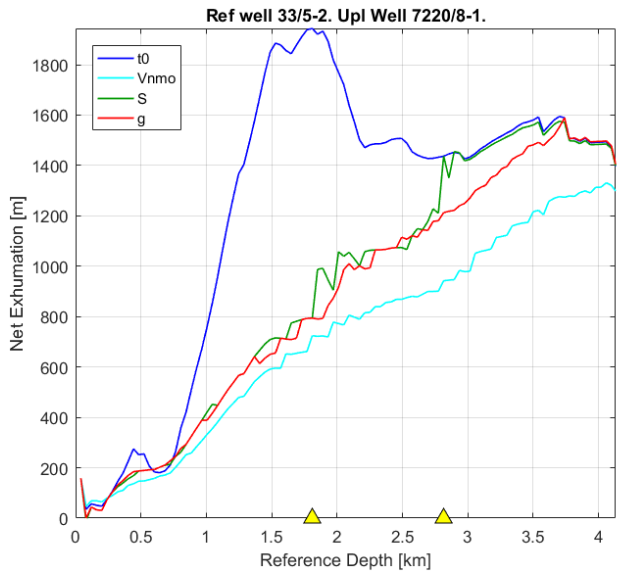

Figure 5.1: Net exhumation estimation in well 7220/8-1 using well 33/5-2 from the Norwegian North Sea as reference. Each curve represents the uplift estimate based on a given criterion, computed for all depths in the reference area. The shallow yellow triangle refers to the stabilization depth while the deep yellow triangle represents the deepest depth where equal heterogeneity is found.

Firstly, it can be observed how the T_0 criterion yields the upper bound of the net exhumation estimate, while the V_{nmo} criterion, provides the lower bound. The uplift estimate from the heterogeneity criterion, represented by the parameters S and g, lie between the upper and lower estimate bounds. This is true for the whole depth range covered in the reference well 33/5-2. Moreover, this is observed in the nine wells for which net uplift magnitudes were estimated. The latter appears to be also independent of the selected reference area. This can be observed in Figures 5.2 and 5.3, which shows the uplift curves for well 7220/8-1, when wells 34/7-1 and 6507/12-1 are used as reference, respectively.

Generally, all criteria yield exhumation estimates which exhibit a significant increase of the uplift magnitude with depth. This is partly expected. According to the well completion reports, and well tops information, the Nordland Formation is present at all locations studied. The latter was deposited during the Late Pliocene-Pleistocene glaciation, and its base represents the major upper regional unconformity (URU), where rocks units Triassic, Jurassic, and Cretaceous in age, subcrop at various location within the Western Barents Sea (Henriksen et al., 2011b). Hence, this formation is most likely at its maximum burial depth, and therefore its velocity is similar to the velocity of the unexhumed shallow sediments from the reference areas. The net exhumation magnitude increases as thicker stratigraphic columns are examined and uplifted rocks with higher velocities compared to the unexhumed area, are included in the effective medium.

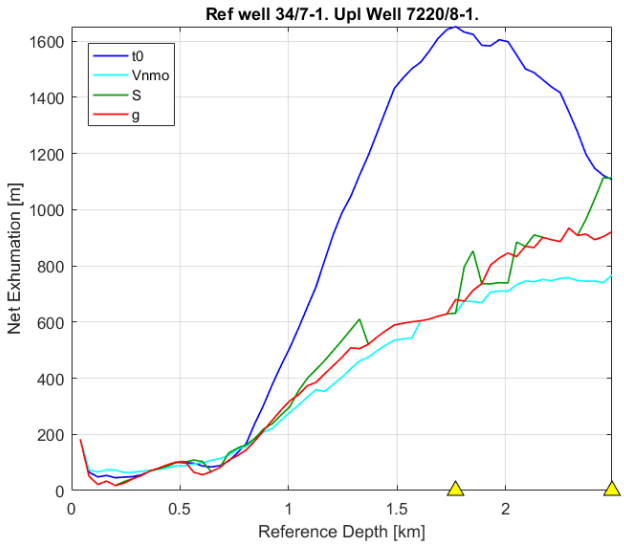

Figure 5.2: Net exhumation estimation in well 7220/8-1 using well 34/7-1 from the Norwegian North Sea as reference. Each curve represents the uplift estimate based on a given criterion, computed for all depths in the reference area. The shallow yellow triangle refers to the stabilization depth while the deep yellow triangle represents the deepest depth where equal heterogeneity is found.

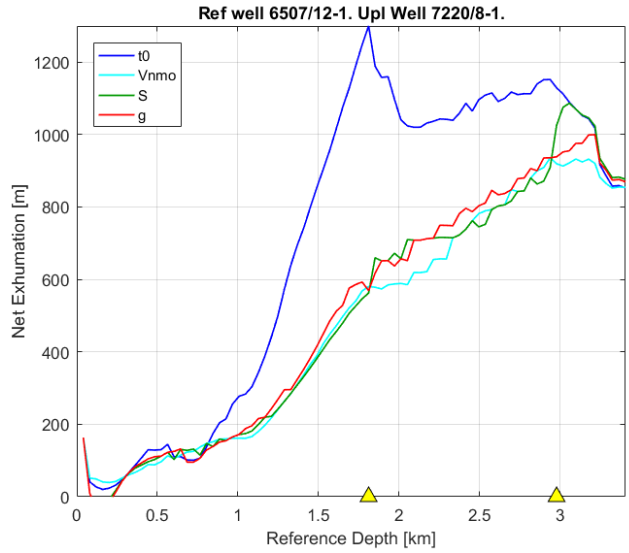

Figure 5.3: Net exhumation estimation in well 7220/8-1 using well 6507/12-1 from the Norwegian Sea as reference. Each curve represents the uplift estimate based on a given criterion, computed for all depths in the reference area. The shallow yellow triangle refers to the stabilization depth while the deep yellow triangle represents the deepest depth where equal heterogeneity is found.

The stabilization depth, i.e. the depth from which the uplift curves yield estimates close to the true magnitude and the method can be trusted, is given by the depth of the T_0 maximum. The latter is depicted by the shallow yellow triangle in Figures 5.1, 5.2 and 5.3. The net exhumation estimate, at a given well location, is given by the mean of the uplift estimates from all criteria, and at all depths between the stabilization depth and the deepest depth where equal heterogeneity S is found. The result of this procedure is shown in Figures 5.4, 5.5 and 5.6, where the net uplift magnitude is computed for well 7220/8-1, using each of the three reference wells.

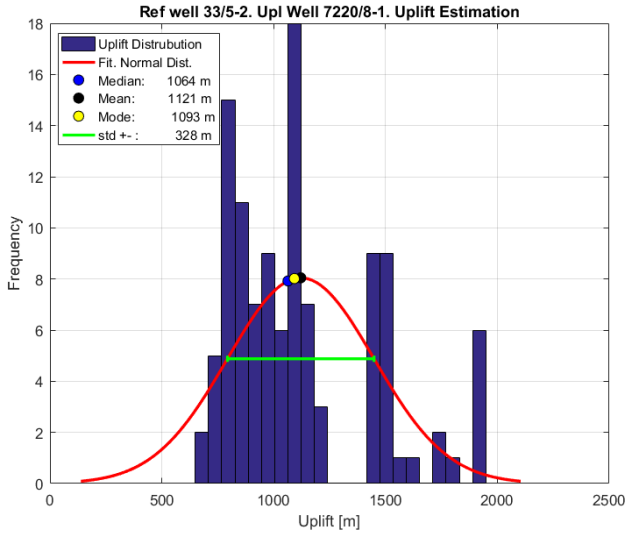

Figure 5.4: Net exhumation estimation in well 7220/8-1 using well 33/5-2 from the Norwegian North Sea as reference. A simple statistical analysis is performed including the magnitudes from all uplift curves between the stabilization depth, and the deepest depth where equal velocity heterogeneity is found.

Using well 33/5-2 as reference yields a net exhumation magnitude of 1127 $\pm$ 308 m within well 7220/8-1. Moreover, well 34/7-1 suggest a net exhumation magnitude of 970 $\pm$ 316 m at the same location, while well 6507/12-1 suggests 840 $\pm$ 179. Figure 5.7 portrays the net exhumation magnitudes estimated at each well location, using each of the three reference wells. The estimates are sorted according to the net uplift magnitudes. Note how reference well 33/5-2, provides consistently higher estimates compared to the other two references. Conversely, well 6507/12-1, suggest consistently lower exhumation magnitudes. Moreover, the difference in magnitude, between the estimates computed from the three references, remain nearly constant across most of the locations studied. The standard deviation for the estimates computed using the reference well 34/7-1 is also depicted in Figure 5.7. Note how the standard deviation seems to increase, to some extent, proportionally to the net exhumation magnitude. Furthermore, at all locations studied, except for the locations of wells 7117/9-1 and 7316/5-1, the standard deviation seems to be consistently larger compared to the differences existing between the three sets of net uplift

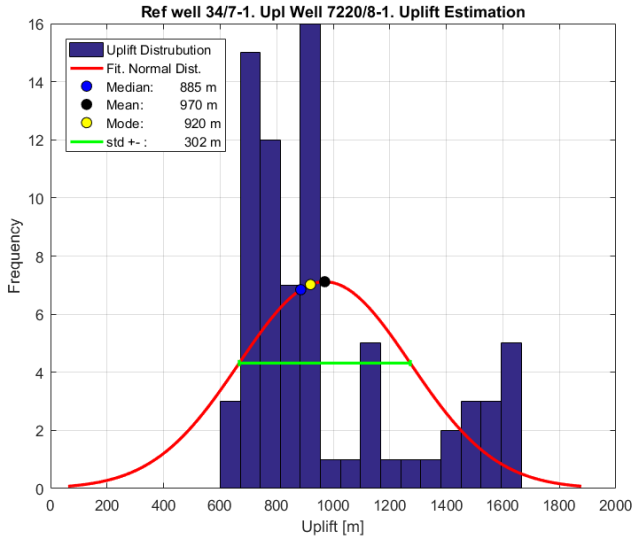

Figure 5.5: Net exhumation estimation in well 7220/8-1 using well 34/7-1 from the Norwegian North Sea as reference. A simple statistical analysis is performed including the magnitudes from all uplift curves between the stabilization depth, and the deepest depth where equal velocity heterogeneity is found.

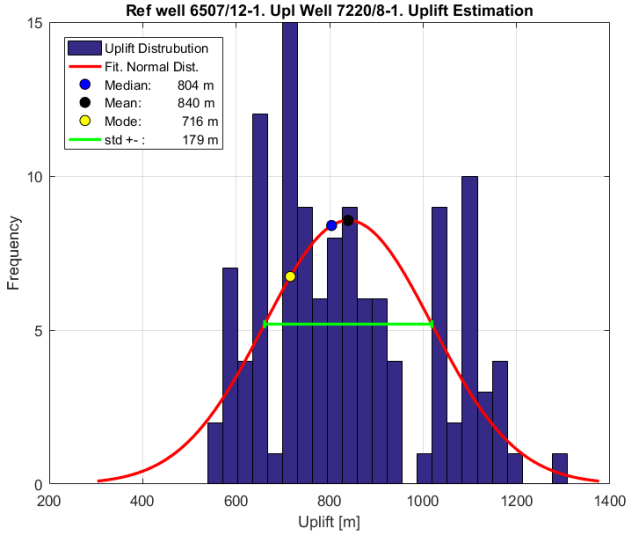

Figure 5.6: Net exhumation estimation in well 7220/8-1 using well 6507/12-1 from the Norwegian Sea as reference. A simple statistical analysis is performed including the magnitudes from all uplift curves between the stabilization depth, and the deepest depth where equal velocity heterogeneity is found.

estimates.

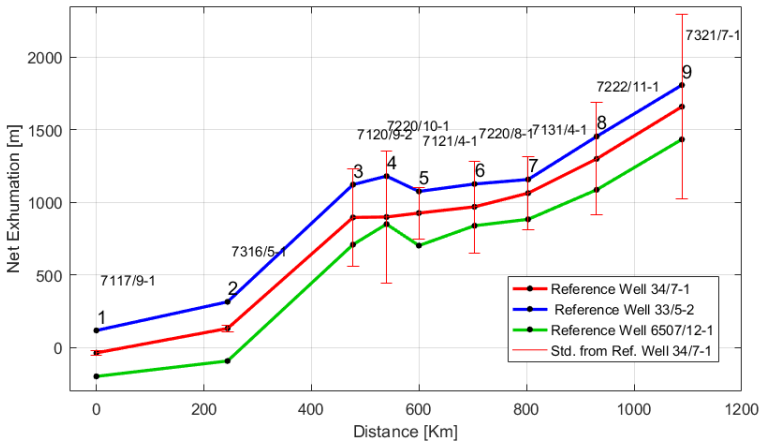

Figure 5.7: Magnitude-sorted net exhumation estimates at all studied locations, using each of the reference wells. Note how the difference in exhumation magnitudes estimated using different references remain approximately constant at all locations study. Standard deviation increases proportionally to the uplift magnitude.

The geographical distribution of the net exhumation magnitudes within the Western Barents Sea is illustrated in Figure 5.8. As reported by several authors (Baig et al., 2016; Ohm et al., 2008; Henriksen et al., 2011a; Johansen, 2016; Riis and Fjeldskaar, 1992), the net uplift magnitude seems to increase from the southwestern part of the Norwegian Barents Sea, towards the the northeast. Locations 1 and 2, Tromsø Basin and the Vestbakken Volcanic Province, respectively, appears to be nearly at their maximum burial depth. The net exhumation magnitudes increases towards the Hammerfest Basin (Locations 3 and 5), the Loppa High (Locations 4 and 8), and the Eastern Part of the Finnmark Platform (Location 7), where magnitudes ranging from 900 m to 1300 m are estimated. Similar net uplift magnitudes are also estimated for the area located at the west of the Polheim Subplatform (Location 6). Within the Loppa high, exhumation magnitude increases from south to north and from west to east. The largest net uplift magnitudes are found within the Fingerdjupet Sub-basin (Location 9), where reference well 34/7-1 suggest a net uplift magnitudes higher than 1600 m.

Table 5.1 summarizes the net exhumation magnitudes that the method provide at each of the locations studied across the western Barents Sea. The estimates are in agreement with the exhumation magnitudes estimated by different authors, using various techniques, from shale compaction depth-trends, to thermal techniques, seismic reflection data, petrographical and sedimentological analysis, etc. The net uplift estimates from Ohm et al. (2008), based entirely on vitrinite reflectance data, seem to be lower compared to the estimates from the other studies. Estimates from Riis and Fjeldskaar (1992) based on geochemical, sedimentological and seismic reflection data, seem to be too high at well locations considered to have experience minor uplift as well 7117/9-1, and too high for

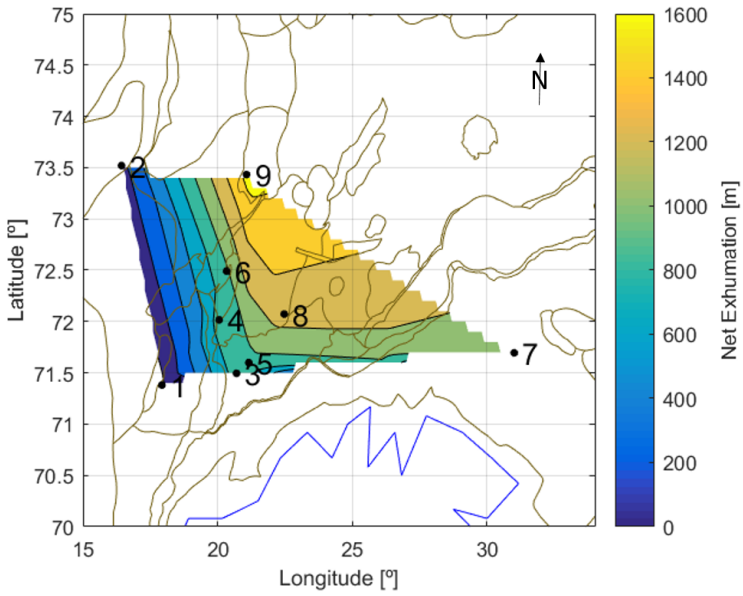

Figure 5.8: Net exhumation map for the Western Barents Sea constructed from the reference well 34/7-1 net uplift estimates. Note how exhumation increases from southwest to the east and north. Location within sub-basins: 1. Tromsø Basin; 2. Vestbakken Volcanic Province; 3 and 5. Hammerfest Basin; 4 and 8. Loppa High; 6. Area West of Polheim Subplatform; 7. Eastern Finnmark Platform. 9. Fingerdjupet Sub-basin. See Figure 5.7 for the well ID's associated to each location.

other wells as 7120/9-2. Similarly, the net exhumation estimates of Porten (2012) and Gyenis (2016), based on petrographical-sedimentological analysis, and shale compaction technique, respectively, represent most likely upper bounds to the exhumation magnitudes. On the other hand, the uplift magnitudes computed using well 33/5-2 as reference tend to be closer to the estimates of Johansen (2016), based on shale compaction techniques. Baig et al. (2016) and Henriksen et al. (2011a) studies, based on thermal and compaction-based techniques, seem to provide the closest magnitudes to the estimates produced with the proposed method. Notwithstanding, evaluation of the three sets of net exhumation magnitudes with regard to intrinsic exhumation and pore fluid pressure, suggest Well 34/7-1 estimates to be closest to the true magnitudes (Evaluation presented in the Discussion Chapter). In this sense, Baig et al. (2016) and Henriksen et al. (2011a) studies seem to slightly overestimate the uplift estimates. However, given the standard deviation of the method proposed, their results are still within the uncertainty bounds.

Table 5.1: Summary table for the net exhumation results and comparison with published studies. Reference well 33/5-2 provides consistently higher net exhumation estimates compared to the other reference wells. Well 34/7-1 provide intermediate estimates, while well 6507/12-1 provide the lowest estimates among the three sets produced. Evaluation of the net exhumation magnitudes estimated using each of the three reference wells, with regard to intrinsic exhumation and pore pressure suggest Well 34/7-1 estimates to be the closest to the true net exhumation magnitudes (See Discussion Chapter).
For a given study, the values reported in the table represent:
-Baig et al. (2016). Average of his study (shale compaction and thermal maturity techniques using well logs, and shot gather data along long offset seismic reflection lines). Retrieved from the net exhumation charts.
-Henriksen et al. (2011a). Average of his study (based on compaction, thermal maturity and apatite fission track analyses). Retrieved from from Baig et al. (2016) exhumation chart.
-Ohm et al. (2008). Vitrinite reflectance data. Retrieved from Baig et al. (2016) net exhumation charts.
-Gyenis (2016). Shale compaction techniques using 'Storvoll et al. (2005) velocity-depth trend and "Mondol (2009) kaolinite:silt 50:50 compaction curve.
-Porten (2012). Petrographic and sedimentological analysis of thin-section. Integrated analysis linking quartz overgrowth, and lack of illitization.
-Johansen (2016). Shale compaction depth trend technique.
-Riis and Fjeldskaar (1992). Geochemical and seismic reflection data.

Well	**33/5-2**	**34/7-1**	**6507/12-1**	**Baig et al. (2016)**	**Henriksen et al. (2011a)**	**Johansen (2016)**	**Ohm et al. (2008)**	**Ris and Fjeld-skaar (1992)**	**Gyenis (2016)**	**Porten (2012)**
7117/9-1	119 $\pm$ 21	-35 $\pm$ 18	-197 $\pm$ 23	200	100	287	100	500		
7120/9-2	1123 $\pm$ 273	897 $\pm$ 335	710 $\pm$ 211	1000	1200		700	1700		
7121/4-1	1076 $\pm$ 191	927 $\pm$ 178	703 $\pm$ 86	900	1050	1149				
7131/4-1	1158 $\pm$ 328	1064 $\pm$ 251	884 $\pm$ 151	1250	1400		800	800		1500
7220/8-1	1127 $\pm$ 308	970 $\pm$ 316	840 $\pm$ 179			1223				
7220/10-1	1181 $\pm$ 390	900 $\pm$ 456	851 $\pm$ 275			1271				
7222/11-1	1454 $\pm$ 468	1300 $\pm$ 386	1087 $\pm$ 242			1657			1300'-1600"	1700
7316/5-1	316 $\pm$ 35	133 $\pm$ 23	-91 $\pm$ 19	$<$50	250					
7321/7-1	1808 $\pm$ 661	1659 $\pm$ 637	1434 $\pm$ 355	1850	1800	1981				

5.2 Burial History Modelling

The net exhumation estimates obtained with the proposed method are used as input to recreate the burial history of selected clean sandstones within various formations, and at different locations across the Western Barents Sea. The time-dependent burial curves are combined with Lander and Walderhaug (1999) mechanical compaction model and Walderhaug (1996) chemical compaction model to evaluate the quality of the exhumation estimates. This is achieved through comparison of modelled quartz cement volumes, porosity, P-wave velocity, and S-wave velocity, with the properties in-situ.

The error bars in Figure 5.7 depicts the standard deviation of the uplift estimates when well 34/7-1 is used as reference. The mean uplift estimates using wells 33/5-2 and 6507/12-1 as reference, generally lie within the the uncertainty range of the uplift magnitudes provided by well 34/7-1. Therefore, the burial curves are constructed based on the minimum, maximum, and mean net exhumation magnitudes suggested by well 34/7-1.

Figure 5.9 illustrate the burial history of the base of cleanest sands within Tubåen Fm. at well 7220/8-1. Since the lower bound of the exhumation estimate (654 m) would result in the formation never being exposed to the quartz cementation temperatures, a slightly higher exhumation magnitude (696 m) was chosen as the lower bound for this particular example. Note how the rock achieves different maximum burial depths according to the minimum (in Green), mean (in Red), and maximum (in Blue) net exhumation estimates.

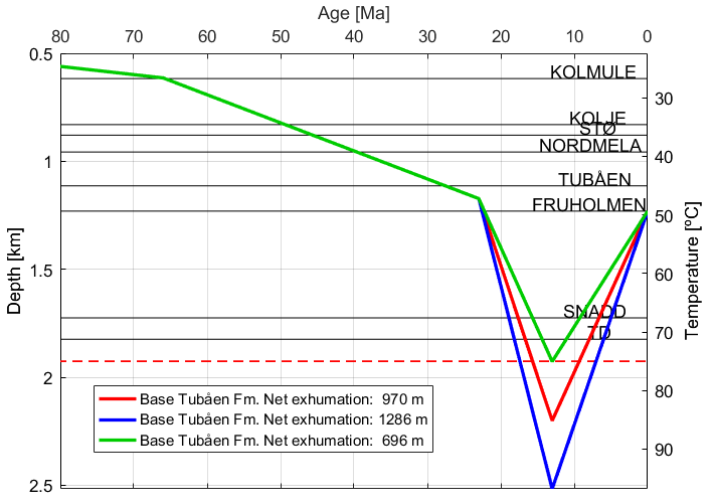

Figure 5.9: Burial History Curve for the base of the cleanest sands within Tubåen Fm. at well 7220/8-1. The burial history is recreated for three scenarios based on the minimum (in green), mean (in red), and maximum (in blue) net exhumation estimates from well 7220/8-1, when using well 34/7-1 as reference. Formation names at the right of the plot refers to present-day formation tops.

The porosity depth-trend modelled for Tubåen Fm. at well 7220/8-1 is shown in Figure 5.10. Porosity decreases due to increasing differential stress from depositional porosity (0.40) where differential stress equals zero, down to a porosity of approximately 0.32, where differential stress is slightly higher than 19 MPa. At this depth, the rock is exposed to temperatures equal or higher than 75°C and quartz cementation starts. Porosity decreases due to quartz cementation in the intergranular space of the rock. Note how the porosity reduction is dependent upon the maximum burial depth the sandstone reaches prior to exhumation. Porosity decreases also during the uplift phase until the rock is exposed to temperatures lower than 75°C, and quartz cementation process ceases. The higher the exhumation magnitude, the higher the temperatures the rock is exposed to, and the more quartz cement is precipitated. The porosity of the in-situ rocks ranges approximately between 0.28 and 0.32, and it can be explained by the mean and the standard deviation of the net exhumation estimate. Similarly to porosity, the bulk density of the in-situ rocks is also explained by the net exhumation magnitudes as shown in Figure 5.11.

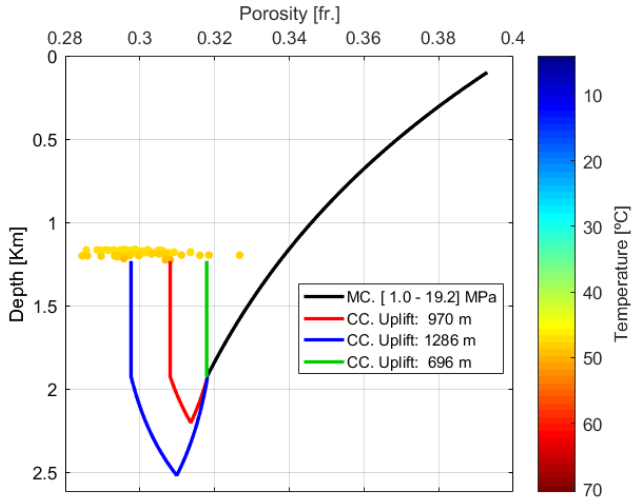

Figure 5.10: Porosity depth-trend modelling for clean sands within Tubåen Fm. at well 7220/8-1. MC refers to the mechanical compaction domain. Porosity loss with time and depth, due to chemical compaction (CC) is modelled considering the minimum (in green), mean (in red), and maximum (in blue) net exhumation scenarios. Circle-scattered data refers to the in-situ porosity of the rock, where its color depict formation temperature.

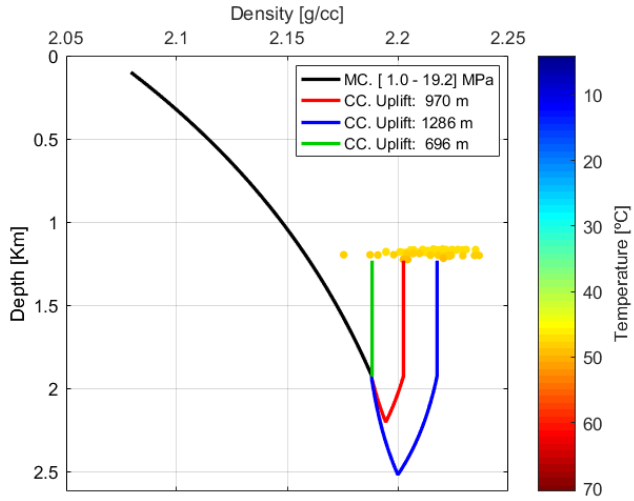

Figure 5.11: Bulk density depth-trend modelling for clean sands within Tubåen Fm. at well 7220/8-1. MC refers to the mechanical compaction domain. Density increase with time and depth due to chemical compaction (CC) is modelled considering the minimum (in green), mean (in red), and maximum (in blue) net exhumation scenarios. Circle-scattered data refers to the in-situ bulk density of the rock, where its color depict formation temperature.

The dry bulk modulus K_{dry}, modelled by means of the Dvorkin et al. (1999) Friable Sand and Unconsolidated Marine Sediments models, and the (Dvorkin and Nur, 1996) Contact-Cement model is shown in Figure 5.12. In the mechanical domain, the stiffness increases with increasing differential stress from slightly less than 1 GPa at 1 MPa differential pressure, up to around 2.6 GPa at 19.2 MPa differential stress. At this pressure, quartz cementation is modelled to take place, and the rock is modelled to become pressure insensitive, i.e. porosity reduction with increasing differential stress ceases, and subsequent stiffening of the rock is modelled to occur purely due to quartz cementation. Quartz cement precipitation results in a severe stiffness increase as shown in Figure 5.12. However, when the rock is modelled to barely enter the cementation window according to the lower bound of the exhumation estimate, only very few quartz cement volumes are precipitated, and despite explaining the observed density and porosity, it does not explain the in-situ dry bulk modulus K_{dry}. On the other hand, the upper bound of the uplift estimate allows for predicting the highest K_{dry} measured at the well location. Moreover, the mean estimate predicts the mean value of the observed K_{dry}. A similar behavior is observed in the modelling of the P-wave velocity shown in Figure 5.13. The upper bound of the modelled P-wave velocity slightly overestimates the measured P-wave velocity. However, the modelling using the mean exhumation estimate predicts the mean P-wave velocity of the sandstone. The mapping of the modelled bulk modulus and P-wave velocity to the depth domain, based on the mechanical and chemical compaction porosity-depth relation, can be observed in Figures 5.14 and 5.15, respectively. See how the mean and upper bound of the net uplift estimate explain the mean and the upper bound of the measured K_{dry} and V_p, respectively.

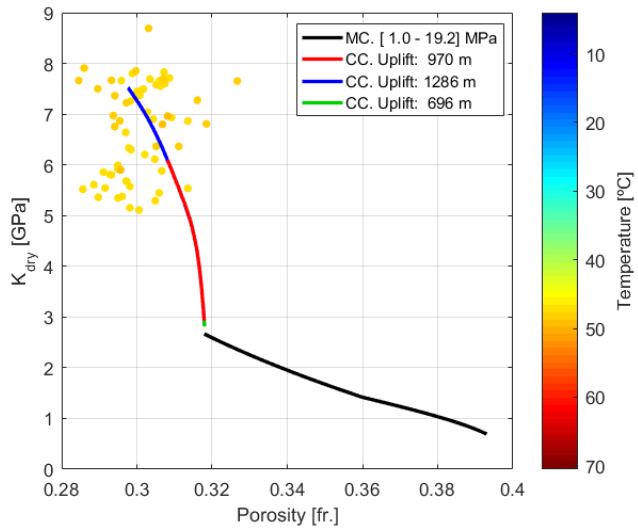

Figure 5.12: Dry bulk moduli K_{dry} modelling for clean sands within Tubåen Fm. at well 7220/8-1. MC refers to the mechanical compaction domain. K_{dry} increase due to chemical compaction (CC) is modelled considering the minimum (in green), mean (in red), and maximum (in blue) net exhumation scenarios. Circle-scattered data refers to the in-situ K_{dry} of the rock, where color depict formation temperature.

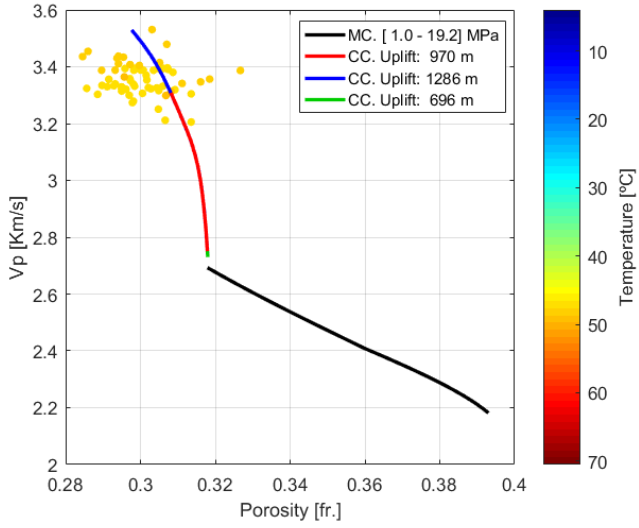

Figure 5.13: P-wave velocity modelling for clean sands within Tubåen Fm. at well 7220/8-1. MC refers to the mechanical compaction domain. V_p increase due to chemical compaction (CC) is modelled considering the minimum (in green), mean (in red), and maximum (in blue) net exhumation scenarios. Circle-scattered data refers to the in-situ V_p of the rock, where color depict formation temperature.

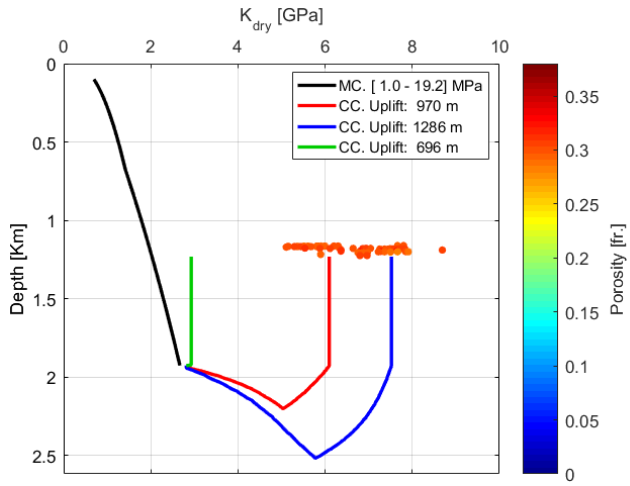

Figure 5.14: Dry bulk moduli K_{dry}, depth-trend modelling for clean sands within Tubåen Fm. at well 7220/8-1. MC refers to the mechanical compaction domain. K_{dry} increase with time and depth, due to chemical compaction (CC) is modelled considering the minimum (in green), mean (in red), and maximum (in blue) net exhumation scenarios. Circle-scattered data refers to the in-situ K_{dry} of the rock, where color depict formation porosity.

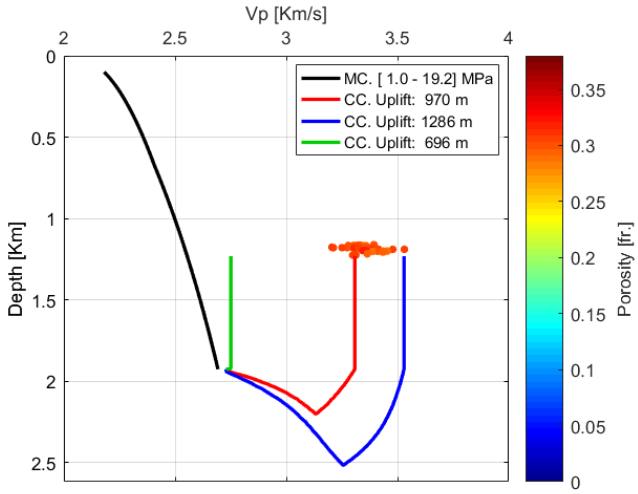

Figure 5.15: P-wave velocity depth-trend modelling for clean sands within Tubåen Fm. at well 7220/8-1. MC refers to the mechanical compaction domain. V_p increase with time and depth, due to chemical compaction (CC) is modelled considering the minimum (in green), mean (in red), and maximum (in blue) net exhumation scenarios. Circle-scattered data refers to the in-situ V_p of the rock, where color depict formation porosity.

In order to perform a sensitive evaluation of the net exhumation estimates, it is prudent to evaluate in addition, the similarity between the modelled and observed parameters for properties related to the shear strength of the rock. The upper bound of the uplift estimate seems to overpredict the shear strength of the dry rock, as shown in Figure 5.16. The same is true for the S-wave velocity, where the upper uplift bound overpredicts the in-situ S-wave velocity, as shown in Figure 5.17. On the other hand, for both μ_{dry} and V_s, the lower bound of the net uplift estimate largely underpredicts the observed properties. Notwithstanding, the μ_{dry} and V_s of the studied samples lie within the uncertainty range related to the standard deviation of the uplift estimate. Moreover, when the mean magnitude is used in the modelling, the observed μ_{dry} and V_s are successfully predicted. The latter is better illustrated in the depth-trends of the shear modulus and the S-wave velocity, shown in Figures 5.18 and 5.19, respectively.

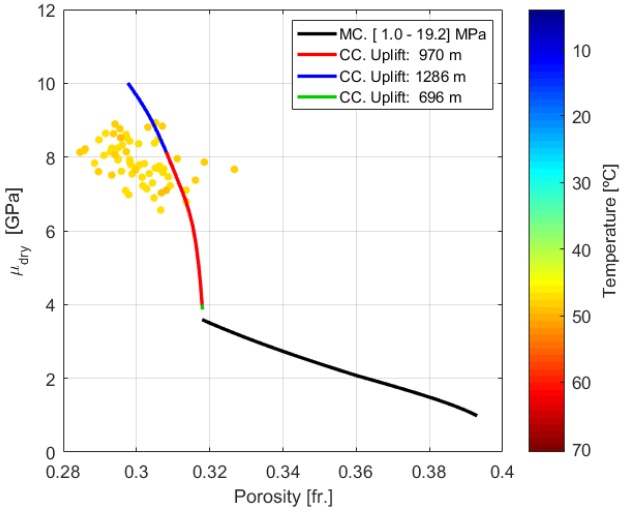

Figure 5.16: Dry shear moduli μ_{dry} modelling for clean sands within Tubåen Fm. at well 7220/8-1. MC refers to the mechanical compaction domain. μ_{dry} increase due to chemical compaction (CC) is modelled considering the minimum (in green), mean (in red), and maximum (in blue) net exhumation scenarios. Circle-scattered data refers to the in-situ μ_{dry} of the rock, where color depict formation temperature.

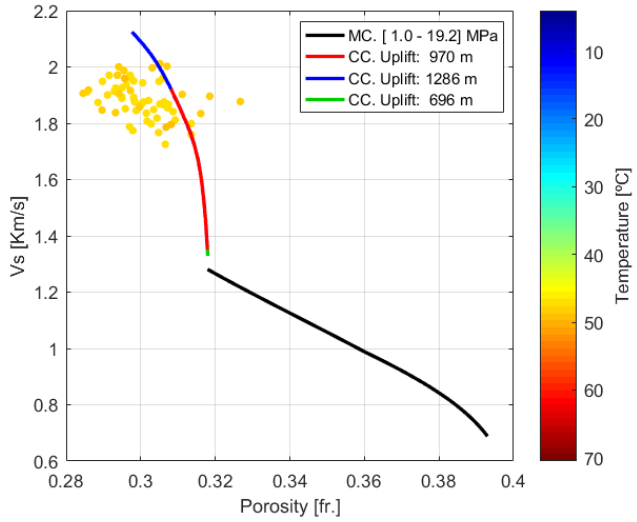

Figure 5.17: S-wave velocity modelling for clean sands within Tubåen Fm. at well 7220/8-1. MC refers to the mechanical compaction domain. V_s increase due to chemical compaction (CC) is modelled considering the minimum (in green), mean (in red), and maximum (in blue) net exhumation scenarios. Circle-scattered data refers to the in-situ V_s of the rock, where color depict formation temperature.

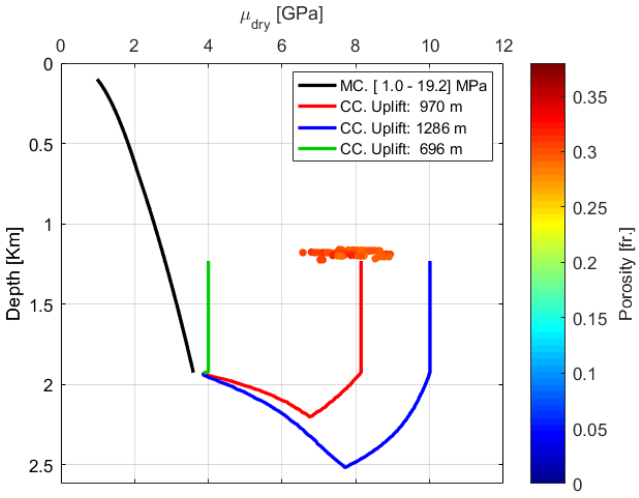

Figure 5.18: Dry shear moduli μ_{dry}, depth-trend modelling for clean sands within Tubåen Fm. at well 7220/8-1. MC refers to the mechanical compaction domain. μ_{dry} increase with time and depth, due to chemical compaction (CC) is modelled considering the minimum (in green), mean (in red), and maximum (in blue) net exhumation scenarios. Circle-scattered data refers to the in-situ μ_{dry} of the rock, where color depicts formation porosity.

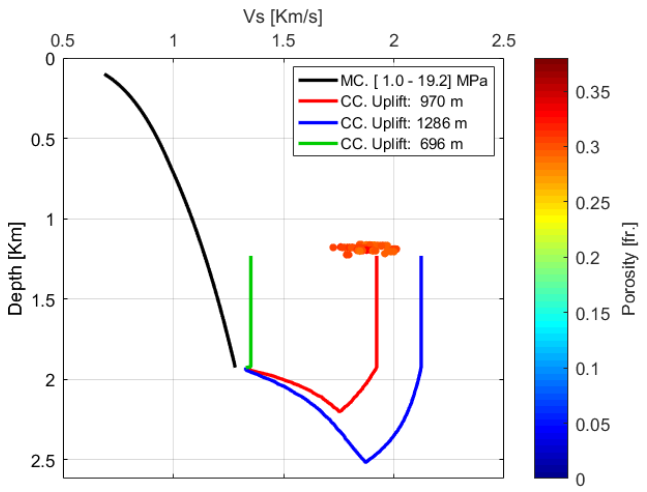

Figure 5.19: S-wave velocity depth-trend modelling for clean sands within Tubåen Fm. at well 7220/8-1. MC refers to the mechanical compaction domain. V_s increase with time and depth, due to chemical compaction (CC) is modelled considering the minimum (in green), mean (in red), and maximum (in blue) net exhumation scenarios. Circle-scattered data refers to the in-situ V_s of the rock, where color depicts formation porosity.

It is worth to mention that throughout the modelling of the nine sandstone formations, the modelled dry shear modulus and S-wave velocity seemed to predict relatively higher values compared to the bulk modulus and the P-wave velocity. The latter can be better observed in Figures 5.15 and 5.19. Note how the upper bound of the modelled P-wave velocity predicts the upper bound of the in-situ property, while the upper bound of the modelled S-wave velocity clearly overpredict the observed property. Shear wave transit times has been measured at this location, and hence, the behavior should not be attributed to errors in the estimation of the S-wave velocity from the the P-wave velocity. The overprediction of the S-wave velocity when using Dvorkin-Nur Contact Cement Model has been previously highlighted by Avseth et al. (2010). Moreover, Mavko et al. (2009) suggested the S-wave velocity estimation, using the same model, to be less reliable compared to the P-wave velocity estimation. Thus, constraining the quartz cement volumes should be more reliable based on the modelling of properties related to the bulk, and not the shear strenght of the rock.

Some interesting observations can be made from the modelling of the Tubåen sandstones at well 7220/8-1: 1) The porosity and the density of the in-situ rocks, are predicted by the upper, mean and lower bounds of the net exhumation estimate, and proved to not be very sensitive to the quartz cement volumes precipitated. 2) None of the elastic moduli of the dry rock, neither the velocities, could be explained without the sandstone undergoing quartz cementation. 3) Properties as the shear modulus of the rock and the S-wave velocity are slightly overestimated using Dvorkin and Nur (1996) contact-cement model. Notwithstanding, considering the velocity variations observed within a selected sandstone

unit, a net uplift magnitude that explains both P- and S- wave velocities, can be found. 4) The mean value of the net uplift estimate allowed for a successful estimation of the petrophysical properties of the Fruholmen Fm., at the location of well 7220/8-1.

Other example worth to present is the modelling of the properties of the Stø Fm. Figure 5.20 illustrates the porosity depth-trend modelled for the clean sands of this formation, at well 7321/7-1. Different from the previous example, the modelling using the mean net exhumation magnitude result in higher porosities compared to the porosities observed at well location. More importantly is that the latter is accompanied by a successful prediction of the mean P-wave and S-wave in-situ velocities, as illustrated in Figures 5.21 and 5.22. This behavior is observed at the four locations where Stø Fm. has been modelled.

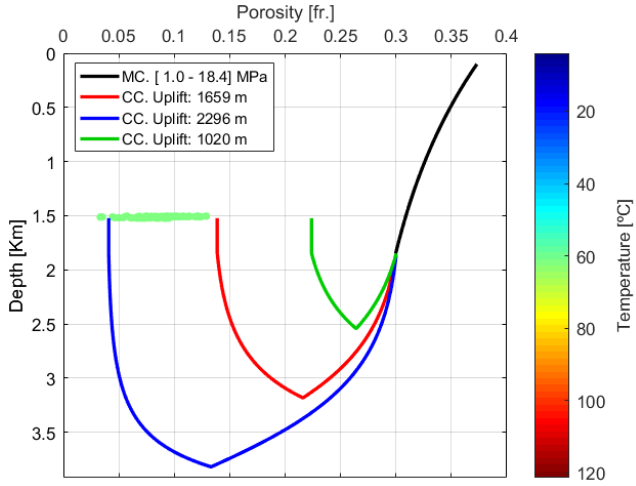

Figure 5.20: Porosity depth-trend modelling for clean sands within Stø Fm. at well 7321/7-1. MC refers to the mechanical compaction domain. Porosity loss with time and depth, due to chemical compaction (CC) is modelled considering the minimum (in green), mean (in red), and maximum (in blue) net exhumation scenarios. Circle-scattered data refers to the in-situ porosity of the rock, where its color depict formation temperature.

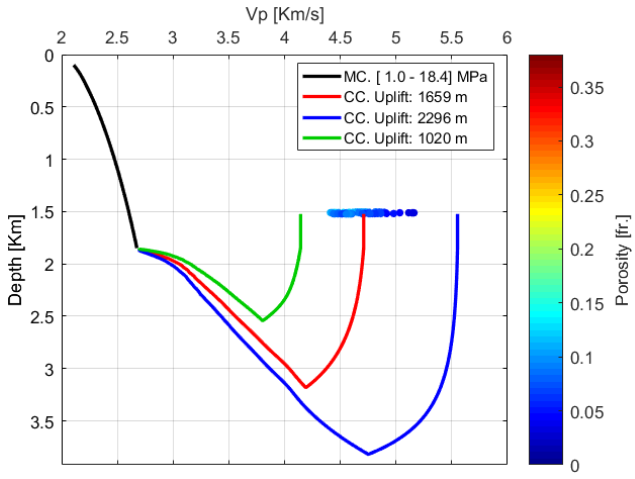

Figure 5.21: P-wave velocity depth-trend modelling for clean sands within Stø Fm. at well 7321/7-1. MC refers to the mechanical compaction domain. V_p increase with time and depth, due to chemical compaction (CC) is modelled considering the minimum (in green), mean (in red), and maximum (in blue) net exhumation scenarios. Circle-scattered data refers to the in-situ V_p of the rock, where color depict formation porosity.

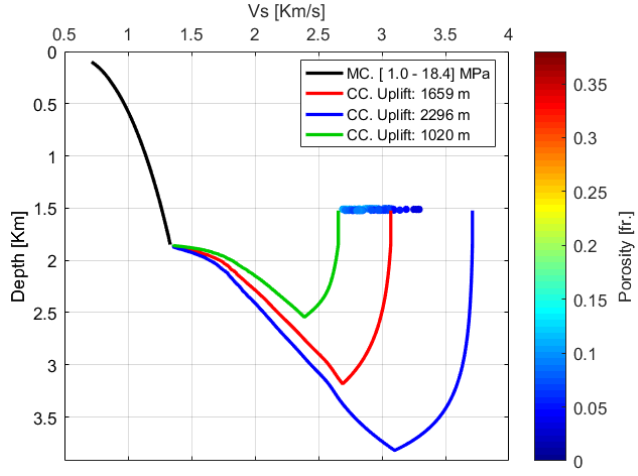

Figure 5.22: S-wave velocity depth-trend modelling for clean sands within Stø Fm. at well 7321/7-1. MC refers to the mechanical compaction domain. V_s increase with time and depth, due to chemical compaction (CC) is modelled considering the minimum (in green), mean (in red), and maximum (in blue) net exhumation scenarios. Circle-scattered data refers to the in-situ V_s of the rock, where color depicts formation porosity.

Mahmood (2013) examined thin sections from the Stø Fm. from four wells within the Snøvit field, in the Hammerfest Basin. At all locations, clay minerals as illite and Kaolinite, authigenic in origin, were found in the pore space. Moreover, Mahmood (2013) reported 5% volume of authigenic clay for well 7121/4-1. At this location, the modelled porosity exceeds the observed mean porosity by a similar fraction. This clay minerals minerals precipitate after burial, and fill the pore space of the rock, as shown in Figure 5.23. This process is not accounted for at any stage of the mechanical nor chemical compaction modelling.

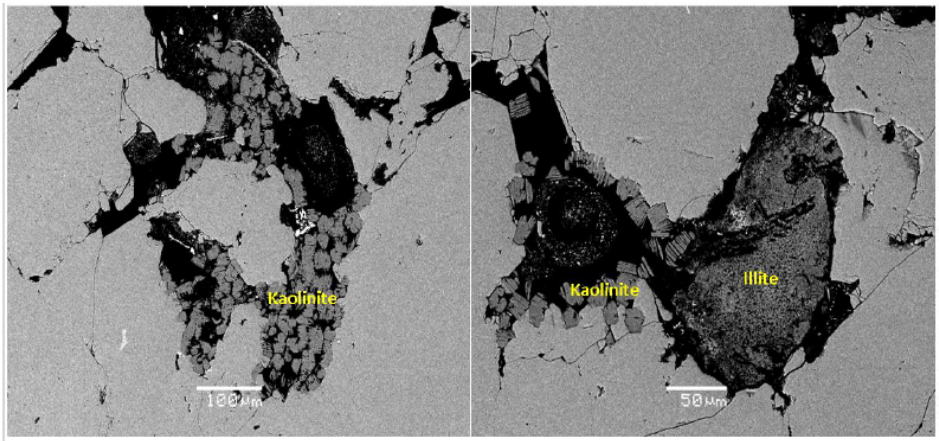

Figure 5.23: Backscattered electron image from Stø Fm. at well 7120/7-3 within Snøhvit field, showing the presence of pore filling kaolinite and illite. Taken from Mahmood (2013).

The P- and S-wave velocities depends mainly on the stiffness of the rock, which is significantly influenced by the initial precipitation of quartz cement. If the overestimation of porosity would be related to a underprediction in the quartz cement volumes, then the bulk and shear strength of the dry rock would be underestimated, and this is not the case.

An explanation for this behavior might then be that the net exhumation magnitudes successfully explain the Late-Cenozoic history of the rock, and consequently, the precipitated quartz cement volumes. Hence, P- and S-wave velocity are accurately predicted. Nevertheless, authigenic minerals, which are not accounted at any stage of the modelling, act as pore filling material, having a significant impact on the porosity whilst having only a minor impact on the stiffness and velocities of the quartz cemented sand.

The burial history modelling has been performed on the Formations Fruholmen, Tubåen, Snadd, Stø, and some thin shallow sandstone intervals within Torsk. A summary of the mean petrophysical properties observed at well locations, and at petrographical analysis reports, together with the properties modelled from the time-dependent burial curves is presented in Table 5.2. Note how at all locations where petrographical thin section analysis are available, as in wells 7121/4-1, 7131/4-1, and 7222/11-1, there is agreement

between the observed quartz cement volumes, and the volumes modelled in the present study. Note in addition, how the clay coating factor is very high for the Snadd Fm. at well 7222/11-1. The quartz grains are almost entirely covered by chlorite coatings according to Gyenis (2016), inhibiting the quartz cementation process. An example of this modelling is illustrated in Figure 7.1 in the appendix.

In general, there seems to be large agreement between the observed/measured properties and the modelled petrophysical properties when the burial history is recreated considering the mean net exhumation magnitudes. Moreover, the discrepancies observed in the modelling, are not attributed to the net exhumation magnitudes. Rather they are considered to be caused by external factors not accounted for by the models, as authigenic pore-filling clay mineral precipitation, and the reliability of Dvorkin-Nur contact cement model, when modelling the S-wave velocity.

Table 5.2: Comparison of the petrophysical properties observed at well locations and in petrographical analysis reports, with the modelled porosity and quartz cement volumes.
- The net uplift refers to the mean value estimated using well 34/7-1 as reference.
- V_q Mod. and ϕ Mod, refers to the modeled quartz volumes and modeled porosity, respectively.
- V_q Petrograph. and ϕ Petrograph., refers to the quartz cement volumes and porosity quantified by some authors through petrographical thin section analysis, respectively.
- V_{Clay} (Auth)* refers to the amounts of authigenic clay volumes quantified by some authors through thin section analysis.
- * From petrographical report:
  Stø Fm. at 7121/4-1 (Mahmood, 2013)
  Fruholmen Fm. at 7131/4-1 (Porten, 2012)
  Snadd Fm. at 7222/11-1 (Porten, 2012; Gyenis, 2016)
- ( ) A net exhumation estimate different than the mean value is used in the modelling.

Well	**Net Uplift [m]**	**V_q Mod [%]**	**V_q Petro-graph.* [%]**	**ϕ Mod [fr.]**	**ϕ Petro-graph.* [fr.]**	**ϕ Log [fr.]**	**V_{Clay} (Auth)* [%]**
7117/9-1 Torsk Sand	(0)	0	-	0.373	-	0.407	-
7120/9-2 Stø	897	4.17	-	0.237	-	0.213	-
7121/4-1 Stø	(850)	8.76	8.7*	0.203	0.175*	0.161	5*
7131/4-1 Fruholmen	1064	0.33	0.3-2.3*	0.310	0.310	0.304	0*
7220/8-1 Tubåen	970	0.99	-	0.308	-	0.301	-
7220/10-1 Stø	900	1.6	-	0.262	-	0.248	-
7222/11-1 Snadd	1300	0.16	0-0.3*	0.305	0.285	0.304	-
7316/5-1 Torsk Sand	133	0	-	0.367	-	0.358	-
7321/7-1 Stø	1659	16.12	-	0.139	-	0.087	-

Chapter 6

Discussion

6.1 Controls on the uplift estimate: Lithology and pore fluid pressure.

As previously observed in Figures 5.1, 5.2, and 5.3, the uplift curves for a given criteria exhibit variations with the reference depth. V_{nmo}, S, and g uplift curves generally exhibit a progressive increase in the exhumation magnitude with increasing depth, and the slope of the curves reduces towards the bottom of the reference model. On the other hand, the T_0 uplift curve normally exhibit a large increase in the uplift magnitude at shallow depths until the stabilization depth is reached. After this depth, the T_0 uplift curve exhibit small high frequency magnitude variations that are closely related to velocity variations in the reference rock sequence. Thus, net exhumation analysis performed at different locations, using the same reference, will result in very similar T_0 uplift curves. However, the low frequency uplift magnitude, depends upon the velocities on both reference and uplifted areas, and thus, upon the actual magnitude of net uplift.

Figure 6.1a depicts the T_0 uplift curve for well 7220/8-1 when well 33/5-2 is used as reference. As previously discussed, the shallowest sedimentary unit deposited in the Barents Sea (Nordland Fm.) is Late Pliocene-Pleistocene in Age, and it is currently at its maximum burial depth. Thus, it has similar velocity to the shallow sediments in the North Sea, and therefore, the uplift magnitude appears to be very low at shallow depths. As thicker lithological columns are examined, and high velocity uplifted rocks are included in the effective medium, the uplift magnitude increases. In Figure 6.1a, the stabilization depth is reached at around 1.75 km below sea bed. At this depth, the high T_0 uplift magnitude is attributed to two combined effects: 1) Method achieves stabilization, i.e. the low frequency trend of estimated uplift magnitudes is close to the true magnitude, and thus, estimates

can be trusted from this depth and deeper, and 2) The low velocity zone between 0.75 and 1.5 km depth. Storvoll et al. (2005) explains that this interval comprises smectitic rich mudstones with some thin silt, sand, and dolomite layers. Low velocity is therefore expected as smectite is difficult to compact, partly due to the bound water which is not released until its transformation to Illite or Chlorite (Storvoll et al., 2005). Note how the uplift magnitude reaches maximum values at the end of the low velocity zone. Note that there is about 0.5 km delay in the response of the uplift curve. Thus at 2 km, the uplift magnitude decreases significantly, in response to the velocity increase marked by the end of the smectitic rich interval. At about 2.5 km depth, the increasing interval P-wave velocity experiences a break in the trend due to increasing pore pressure compared to hydrostatic conditions. This causes a 200 m increase in the T_0 uplift magnitude starting from about 3 km depth. Note how the uplift magnitude decreases significantly after 2 km. At about 3.6 km depth, the interval velocity is increased, perhaps due to lithological variations overcoming the overpressure effect, or a reduction in the pore fluid pressure. The latter results in the T_0 uplift magnitude decrease observed at the end of the model.

On the other hand, for a given depth in the reference model, equal V_{nmo}, and S and g, are found at shallower depths in the uplifted model, since higher velocity, and velocity gradients are generally observed in exhumed areas. However, T_0 is inversely proportional to velocity, and thus equal T_0 is generally achieved at deeper depths in the uplifted area, where greater velocities dominate. This, can be observed in Figure 6.1b, where the T_0 P-wave function accounts for velocities near to 4 km/s, at a depth greater than 1.5 km, compared to the velocities accounted by the other criteria, of about 2.5 km/s at 0.5 km depth. Hence, T_0 criteria generally suggests higher exhumation magnitudes compared to the rest of the criteria, and represents most likely the upper bound of the uplift estimate.

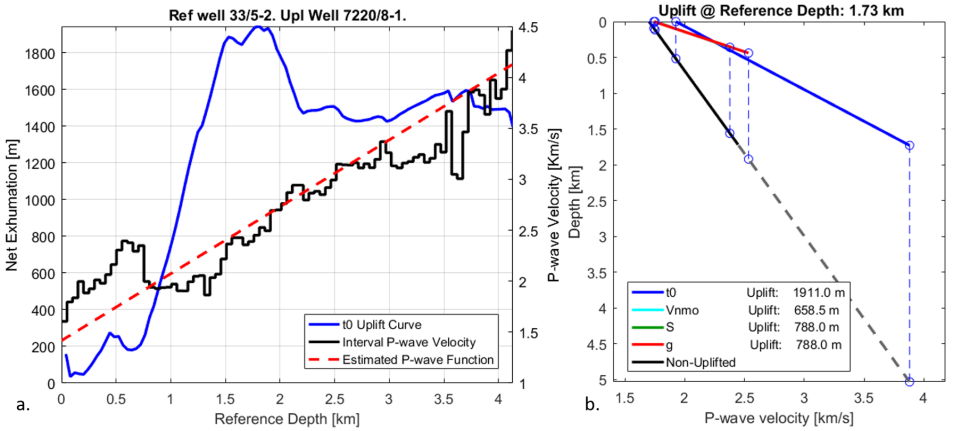

Figure 6.1: a) T_0 uplift curve for well 7220/8-1 using well 33/5-2 as reference. The plot is overlayed with the P-wave velocity profile of the reference well, and the linear P-wave function that explain the traveltimes down to the bottom depth. b) Uplift estimation at the stabilization depth: 1.73 km depth. Note how T_0 uplift is much higher compared to the rest of the criteria. S and g functions overlap with each other in the current plot.

6.2 Reference Wells. Which estimates are best?

The net exhumation estimates were computed using traveltime data from three reference wells. Wells 33/5-2, and 34/7-1 located in the Northern North Sea, and well 6507/12-1 from the Norwegian Sea. As previously observed, the uplift magnitudes estimated in the Western Barents Sea using well 33/5-2 are consistently higher, compared to the other two references. Conversely, well 6507/12-1 provides consistently lower exhumation magnitudes compared to the other two references, while the results using well 34/7-1, appears to consistently lie within the two previous estimates. Moreover, the difference between the estimates remains approximately constant among the different locations studied. The aforementioned aspects raises the following question: Which estimates should be trusted? Is there a reference well whose suggested estimates are closer to the true net uplift magnitudes? To answer this question, an evaluation of the P-wave velocities at each reference is presented in terms of intrinsic exhumation magnitude and pore pressure. Figure 6.2a depicts the backus-averaged interval P-wave velocity at each of the three reference areas used in the present study, along with its location in Figure 6.2b.

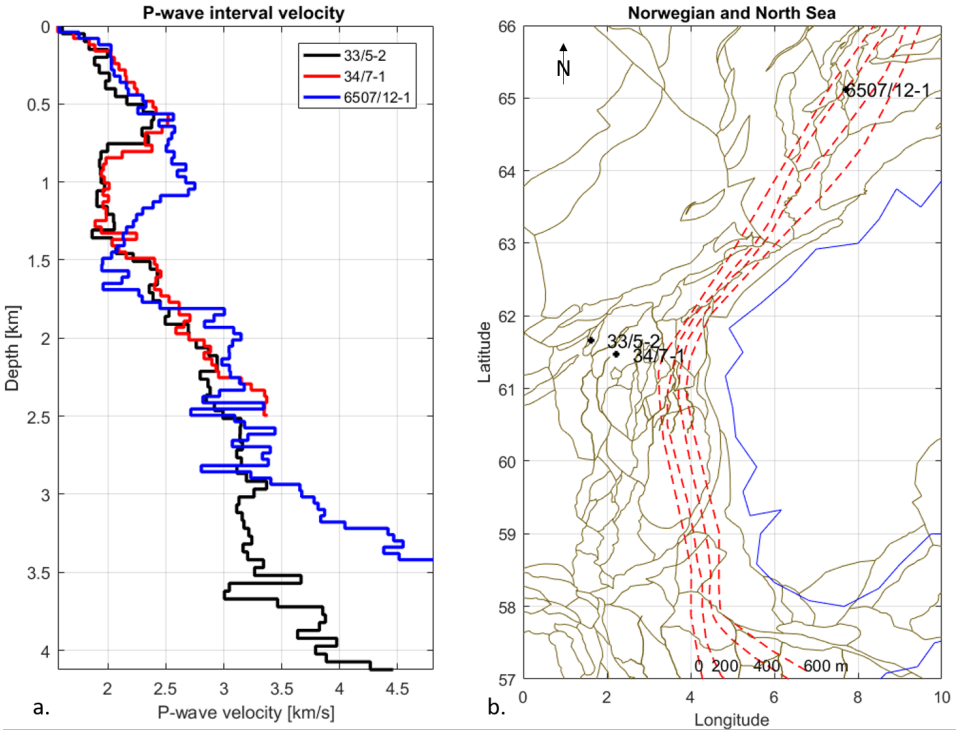

Figure 6.2: a) P-wave interval velocity profiles for the reference wells used in the present study. Depth is referenced to seabed. b) Location of the reference wells within the Norwegian Shelf, together with the iso-net-uplift curves of Hansen (1996), derived using the shale compaction depth-trend technique.

The map is overlayed with net exhumation magnitude contours derived from a comprehensive net uplift analysis using the shale depth-trend compaction method (Hansen, 1996). As it can be observed in the interval velocity profiles, well 6507/12-1 exhibit higher velocities than well 34/7-1, which at the same time exhibit higher velocities compared to well 33/5-2. This explains the net exhumation magnitude trend observed previously. According to Hansen (1996) study, well 6507/12-1 might have been uplifted by about 200 m. This might explain the higher velocities observed at this location. Moreover, the pore pressure evaluation at this location indicates that excepting the smectitic rich low velocity unit, hydrostatic pore pressure dominates the stratigraphic sequence (See Figure 6.3). The pore pressure data is taken from the completion reports of each well, where the pore pressure is estimating through a combination of mud weight measurements, Repeat Formation Test (RFT) data, Leak Off data, and interval sonic transit time measurements.

On the other hand, wells 33/5-2 and 34/7-1, where lower velocity dominates compared to well 6507/12-1, appear to be at their maximum burial depth according to (Hansen, 1996) study. However, the pore pressure increases with respect to hydrostatic conditions at both locations, as shown in Figure 6.3. The pore pressure in well 34/7-1 behaves hydrostatically down to approximately 1400 m KB where pressure starts to build up. From this depth, the pore pressure increases down to approximately 2400 m KB, where RFT data suggest a pressure drop. Well 33/5-2 appears to be slighly overpressured (1.15 g/cm^3 pore pressure gradient) down to 3250 m KB where pressure start to build up reaching a maximum of 1.6 g/cm^3 pore pressure gradient at the bottom of the well. Quantitatively, both wells reaches the same maximum pore pressure gradient of 1.6 g/cm^3. However, the cumulative effect along the whole stratigraphic sequence, seems to be greater for well 33/5-2, which exhibit anomalous pore pressures from the very shallow depths. The P-wave functions that are estimated with Stovas and Ursin (2007) formulation, depend upon the velocities of the whole stratigraphic sequence down to the selected depth. Hence, the net exhumation estimates are affected by the low velocity of the overpressured shallow sediments. This effect is considered to be more important at well 33/5-2, where the slightly overpressured shallow sediments exhibit lower velocities compared to hydrostatically pressured shallow sediments in well 34/7-1, as shown in Figure 6.2.

In addition, the burial history modelling supports that the exhumation estimates from well 34/7-1 should be closer to the true net exhumation magnitudes. Petrophysical properties modelled based on the exhumation estimates from wells 33/5-2 and 6507/12-1 represent most likely upper, and lower bounds to the in-situ properties. Notwithstanding, when the time-dependent burial curves are constructed using the mean net exhumation estimates from well 34/7-1, the mean of the in-situ properties are predicted. Hence, the integrated evaluation suggest that the net exhumation estimates based on the reference well 34/7-1 should be closer to the true uplift magnitudes.

Compared to the shale compaction depth-trend technique, the effective medium method is expected to be less affected by abnormal pore fluid pressures in the reference unexhumed area. The latter can be explained by two main factors: Firstly, if the different units within the reference stratigraphic column reached maximum burial depth at the same time, more information regarding the net exhumation magnitude is comprised within the effective ref-

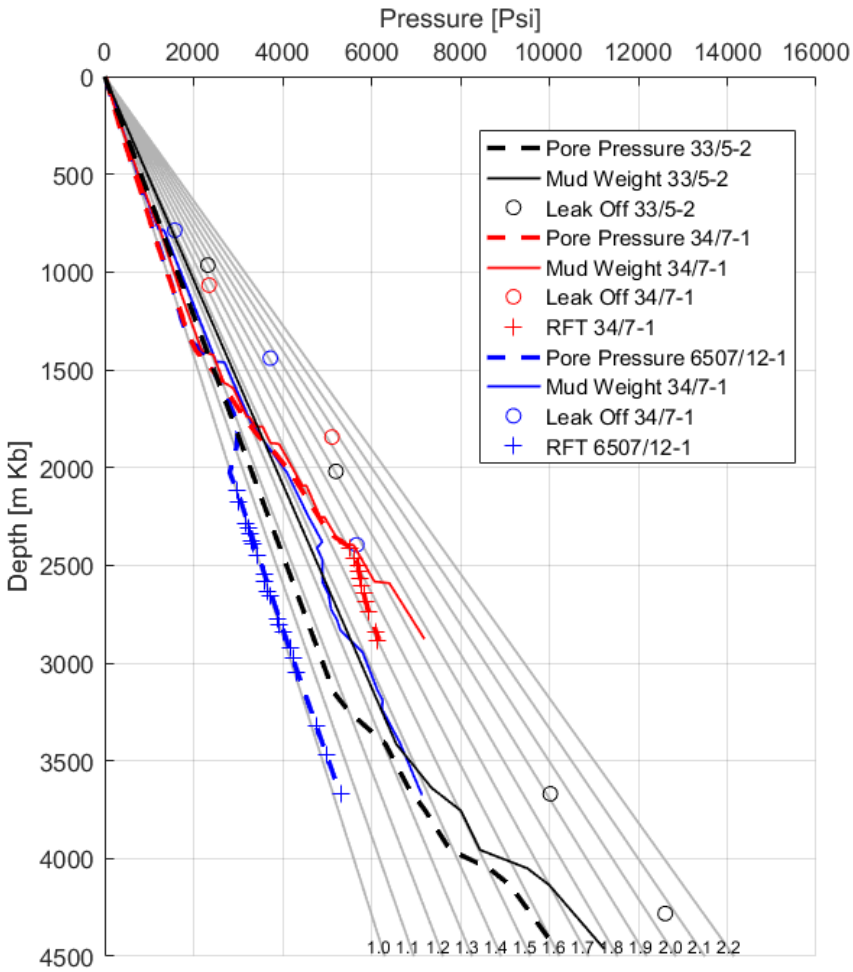

Figure 6.3: Estimated pore pressure profiles for the reference wells used in the present study. Mud weight measurements, Leak off data and RFT data, are shown for comparison. Depth is referenced to Kelly bushing elevation. Gray lines represent reference pore pressure gradients in g/cm^3.

erence medium. On the contrary, in the shale compaction technique, the maximum burial depth is expected to be recorded only on a particular shale unit, and thus, the method provides statistically less information regarding the net exhumation magnitude. To increase the statistics, velocity information from the selected shale unit from several locations considered to be at their maximum burial depth, are combined (Hansen, 1996; Tassone et al., 2014). The latter is also performed with the aim of reducing the uncertainty associate to lithological variations between the shale unit from reference and uplifted areas. Secondly, discerning abnormally pressured formations from units located at their maximum burial depth, is a rather complicated task. Within the Norwegian and North Sea, areas consid-

ered to be hydrostatically pressured generally lie within uplifted areas of the basins, whilst abnormal pore pressure are commonly observed at areas currently at their maximum burial depth. Notwithstanding, the proposed method, estimates P-wave functions through rock sequences comprising both overpressured and normally pressured units. Hence, the effect of a given low-velocity, abnormally-pressured unit is expected to be attenuated, as higher velocity normally compacted sediments are included in the reference effective medium. Thus,

6.3 Multi-phase erosion on the effective-medium compaction-based technique

Jaspen (2000) exemplified how net exhumation magnitudes can be estimated in areas affected by multi-phase erosion, when two homogeneous units which have not been simultaneously at maximum burial depth, are encountered in the same wells. However, the latter cannot be discerned with effective medium techniques.

In the methodology introduced in this study, P-wave linear functions are estimated for composite columns whose time-depth thickness is increased at each step. Thus, the velocity functions could might account or not, for the formations exposed to different maximum burial depths, depending upon the thickness of the column examined.

Despite both uplift episodes could be qualitatively evaluated by examining the magnitude changes that the uplift curves provide at different burial depths, the method cannot quantitatively distinguish between the various uplift episodes. The net uplift estimate represents an average of all the magnitudes within the stabilization depth, and the deepest depth where equal heterogeneity is found. Thus, any information with regard the to maximum burial depth of each of the different formations is averaged. Hence, in areas affected by multi-phase erosion, the method would most likely provide the average magnitude of the different exhumation episodes, recorded by the different units, weighted by the thickness fraction of each unit with respect to the thickness of the whole composite column. Conversely, the net uplift estimate would be closer to the true magnitude in areas where the whole stratigraphic sequence has reached maximum burial depth at the same time.

In the Barents Sea, several unconformities are recognized at different stratigraphic levels as shown in Figure 3.2. The most important unconformities are the Base Cenozoic, and the Upper Regional unconformity (URU), which marks the base of the glacigenic sediments deposited in response to the Late Pliocene-Pleistoscene glacial erosion (Baig et al., 2016). Moreover, there seems to be agreement that rocks where subjected to maximum burial depth before the last episode of Cenozoic exhumation, as highlighted by Zattin et al. (2016). Thus, the net exhumation magnitudes provided in this study, are considered to be close to the true magnitude.

6.4 Evaluation of the net exhumation estimates: Differential stress and Sandstone Compaction trends

Henriksen et al. (2011a) with the intention of evaluating the quality of their net exhumation estimates, compared core porosity of Upper Triassic/Jurassic uplifted sandstones from the Barents Sea, to Ramm and Bjørlykke (1994) porosity depth-trend derived for sandstones in the Haltenbanken Area (Mid-Norwegian Sea). However, evaluating the uplift magnitude considering a unexhumed trend which explain both mechanical and chemical compaction with a first order polynomial is rather a gross approximation. It neglects the exponential nature of compaction as differential stress increases as described by several authors (Athy, 1930; Magara, 1976; Lander and Walderhaug, 1999). Moreover, it is not precise at accounting for the the increased porosity loss due to quartz cementation in deeply buried sandstones.

An improved evaluation of the exhumation magnitudes can be performed by using Vucelic et al. (2017) P-wave velocity mechanical and chemical compaction depth trends derived for Norwegian Sea and North Sea sandstones. Figure 6.4a depicts this trends together with the mean P-wave velocity of brine saturated unexhumed sandstones studied by Vucelic et al. (2017), and the P-wave velocity of the brine saturated Barents Sea sands analyzed in this study. Note how the uplifted sandstones from the Barents Sea exhibit higher velocities at shallower depths, compared to the North Sea and Norwegian Sea non-uplifted sands. Figure 6.4b depicts the scenario where the rocks have been corrected to their maximum burial depth based on the net exhumation magnitudes estimated using well 34/7-1 as reference. The grain size of the sandstones modelled in this study ranges between 0.10 and 0.27 mm with a mean value of 0.16 mm. Thus, the chemical compaction trend of Vucelic et al. (2017) for fine grains (in Blue) should adjust better to the depth corrected Barents Sea sands. Generally, the geothermal gradient in the Barents Shelf is larger compared that in the North Sea and Norwegian Sea basins. Thus, quartz cementation is generally expected to occur at shallower depths in the Barents Sea (See Table 7.1 in the appendix for detailed information about the Barents Sea temperatures). Moreover, the largest differences after the uplift correction are observed at locations where marked difference in the geothermal gradient between the Barents Sea, and Norwegian and North Sea exists. For example, present day temperature profiles of well 7131/4-1 suggest that quartz cementation temperature (75°) is reached at 1.626 km depth, which would explain the depth difference between the Fruholmen Fm. and the unexhumed trend, at this location.

Another evaluation of the net exhumation estimates can be performed by studying the differential stress profiles at each of the locations studied. For normally compacted unexhumed areas, a differential stress gradient of 10 MPa is normally observed across the Norwegian and North Sea. As exhumation take place, stiffer and denser rocks are displaced towards shallower depths, and if pore pressure behaves hydrostatically, an increase in the differential stress gradient is expected. The latter can be observed in Figure 6.5, where the differential stress assuming hydrostatic pore pressure has been computed at all locations studied. The legend of the figure depicts the magnitude-sorted mean net exhumation estimates obtained with our method. Note how at the locations where our technique

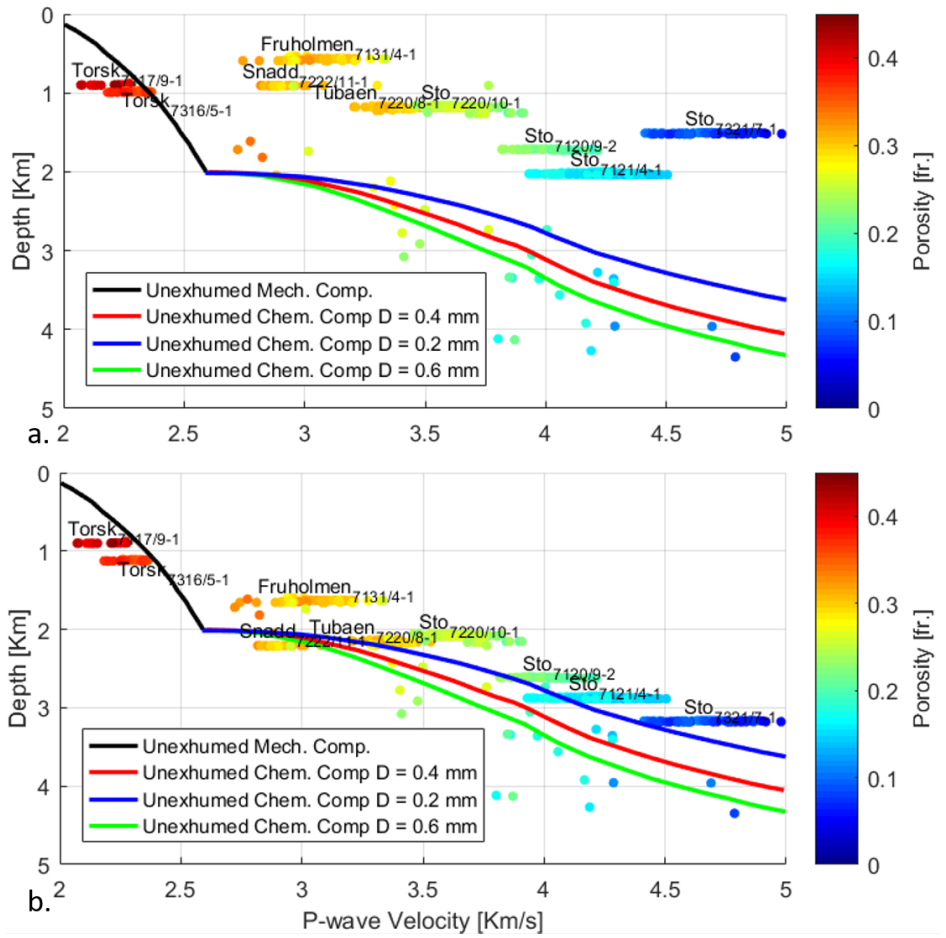

Figure 6.4: a) Present-day depth, sandstone velocity comparison. The red, blue, and green curves refers to the chemical compaction trends of Vucelic et al. (2017), derived for clean sands within the Norwegian Sea and the Northern North Sea, using various grain sizes D. The black curve represents the mechanical compaction trend. The single dots refers to the mean P-wave velocity of the sands studied by Vucelic et al. (2017). Clustered data represents the velocity Barents Sea sands analyzed in this study. The color in the scatter data depicts formation porosity. b) Barents Sea sands are depth corrected to their maximum burial depth based on the net exhumation estimates.

and the burial history modelling suggest zero or minor net uplift as in well 7117/9-1, the differential stress has a gradient close to 10 MPa/km. Moreover, at almost all locations, the pressure gradient increase is closely correlated with the net uplift magnitudes. Furthermore, Figure 6.5 highlights the importance of using Palaeo-stress profiles (assumed 10 MPa/km in this study) and not present-day pressure, when modelling mechanical compaction in uplifted basins. Otherwise, it would result in magnification of the porosity loss in the mechanical compaction domain.

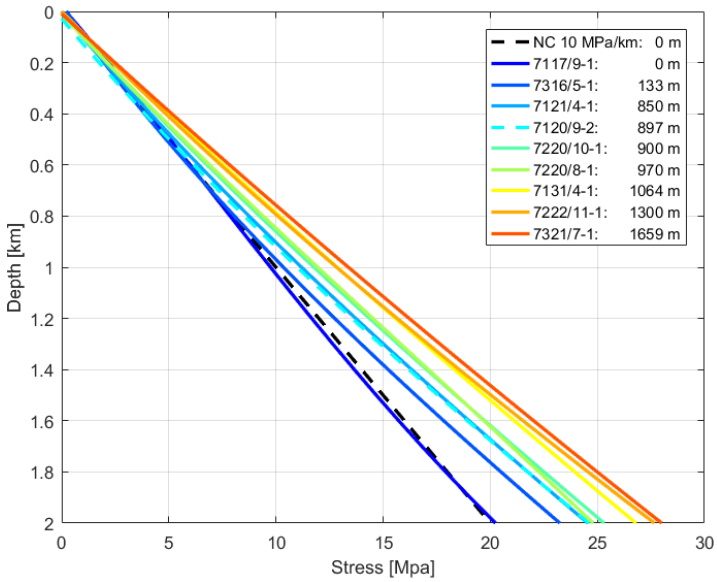

Figure 6.5: Differential Stress estimated at each of the locations studied in the western Barents Sea. Hydrostatic pore pressure is assumed. The segmented black line refers to the normal compaction differential pressure gradient of 10 MPa/km commonly observed in the Northern North Sea and Norwegian Sea. Note the high correlation between the net uplift magnitudes, and the pressure gradient.

6.5 Anisotropy Effect on the net exhumation estimates

The methodology described in this study for the estimation of the net exhumation magnitude has its foundation on the theory developed by Stovas and Ursin (2007). According to their formulation, given large-offset traveltime data through a stack of isotropic, horizontally layered strata, a P-wave linear velocity function that explains the traveltimes down to a given reflector can be estimated. However, the majority of the crustal rocks are experimentally found to be anisotropic (Thomsen, 1986).

In the present study, traveltime data has been generated by means of isotropic ray tracing through backus-averaged P-wave velocity logs. Hence, the offset-dependent NMO parameters obtained through the velocity analysis as V_{nmo} and S, respond only to the heterogeneity of the media. However, if traveltime data were generated by a real seismic example, V_{nmo} and S would be affected by both heterogeneity and anisotropy. The latter, in principle, would violate the assumptions required by Stovas and Ursin (2007) formulation.

Li (2006) proposed some relations that allows for the prediction of weak anisotropic parameters using the P-wave velocity of a sedimentary rock as a proxy of compaction, and the clay volume. The NMO parameters were computed from analytical equations

relating the firsts, with the weak anisotropic parameters. Thus, a short example simulating transversely isotropic (VTI) data could be performed to test the applicability of the methodology on anisotropic data. The example suggests that due to the anisotropy effect, the heterogeneity parameter S increases to magnitudes which are hardly caused by the heterogeneity of the media itself. Hence, Stovas and Ursin (2007) formulation assumptions are violated, and the estimated P-wave velocity function does not explain the exact traveltimes. Moreover, the thickness of the layer is underpredicted, as shown in Figure 6.6a. However, the hypothesis is that the thick sedimentary sequences examined in the unexhumed area, and the generally thinner equivalent effective-media in the uplifted area, exhibit similar degree of anisotropy. Thus the error in the prediction of the traveltimes and thicknesses, is similar as well. Notwithstanding, the relative velocity differences between reference and uplifted areas are preserved, and the net uplift estimate is not very much affected. The latter is illustrated in Figure 6.6b. The anisotropic net exhumation example for well 7220/8-1 using well 33/5-2 as reference suggest 1102 m uplift at this location, which is similar to the 1127 m predicted using the same reference in the isotropic example (See Figure 5.4). A more detailed study concerning the quantitative impact of anisotropy

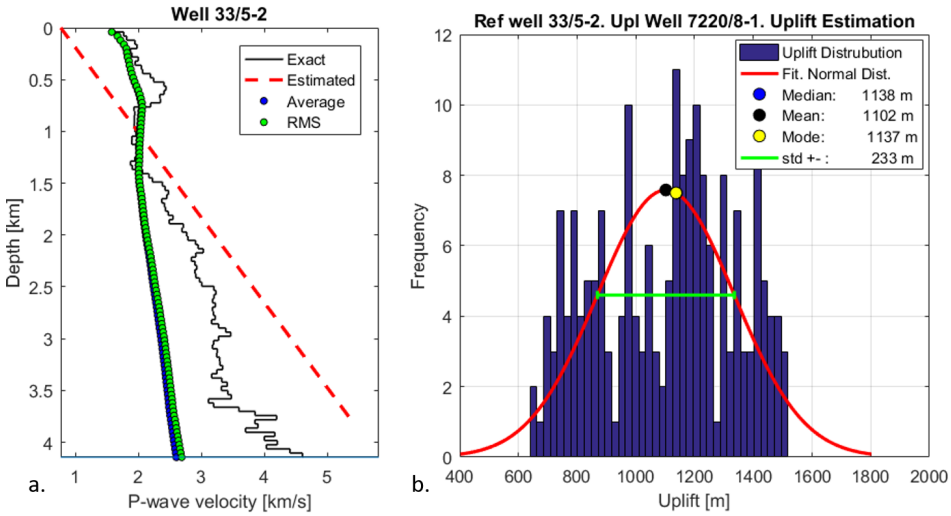

Figure 6.6: a) P-wave linear velocity function estimation on a semi-synthetic anisotropic media. Note how the thickness of the well column is underpredicted. b) Anisotropic net exhumation estimation for well 7220/8-1 using well 33/5-2 as reference. Result is similar to the isotropic uplift estimation example.

on the net uplift estimate is still required. However, the short example suggest that the anisotropic net exhumation estimate is similar to the isotropic analogue, and depicts the applicability potential of the method on real seismic examples.

6.6 Burial History Modelling. Sensitivity Analysis

The time-dependent burial curves, whose construction is aided by the net exhumation estimates of the methodology proposed, proved to be successful in the prediction of clean sandstones petrophysical properties. Both petrophysical properties measured at well locations, and observed through thin sections petrographical analysis, were predicted. However, the mechanical and chemical modelling is dependent on many parameters, whose sensitivity, and uncertainty with respect to their estimation is worth to discuss.

In the results chapter, the effect of selecting different exhumation magnitudes was illustrated by modifying the burial history curve according to the minimum, mean, and maximum exhumation magnitudes obtained using well 34/7-1 as reference. The exhumation magnitude is of first order importance, and the mean value of the petrophysical properties could only be predicted in all parameters ϕ, ρ, K_{dry}, μ_{dry}, V_p and V_s, when the mean value of the exhumation estimates were used.

On the other hand, the modelling appeared to be significantly sensitive to the grain size D, as shown in Figure 6.7. However, it is less sensitive compared to the sensitivity to the net exhumation magnitudes. Note how porosity, density, and P- and S-wave velocities are predicted for variations of $\pm$ 0.10 mm around the selected value for the modelling. However, grain sizes round 0.08 mm suggest over prediction of the S-wave velocity. Nevertheless, the selection of the grain sizes for some of the formations has been constrained by thin section petrographic analysis presented in published literature, and core descriptions presented at completion reports. Moreover, at locations where information is missing, qualified guesses based on data from neighbour wells, and lithological description of the formations have been used. Hence, selected grain sizes are considered to be representative of the studied formations, and to not represent an important source of error for this particular study. The construction of the time-dependent burial curves requires also information regarding the timing when the rock reaches its maximum burial depth. Despite a quantitative example is not presented here, qualitative evaluation suggest the latter to be less important compared to the net exhumation magnitude for this particular study, given the time constrains set by previous studies. Zattin et al. (2016) performs a comprehensive discussion regarding the time constraints to the Cenozoic exhumation. According to their bibliography review, three main Cenozoic exhumation episodes have been proposed in previous studies: One in the Late Paleocene-Early (55-50 Ma) related to the opening of the Norwegian-Greenland Sea, a second, of age Oligocene-Miocene (30-15 Ma), related to inversion during the development of the passive margin, and a third, of fluvio-glacial origin, during the Late Pliocene-Pleistocene glaciation (2.6-0 Ma). However, according to Zattin et al. (2016) integrated study combining apatite (U-Th)/He thermochronology data, and vitrinite reflectance measurements, exhumation occurred in the Late Miocene-early Pliocene, ruling out the hypotesis of uplift related to the passive margin development, diminishing the significance of the glacial related uplift, and suggesting a distinct exhumation phase preceding the glaciations. Letting the time of maximum burial depth to span between 55 and 2.7 Ma would have had a significant impact in the modelling. However, restricting the times for maximum burial depth to Late Miocene-early Pliocene, according

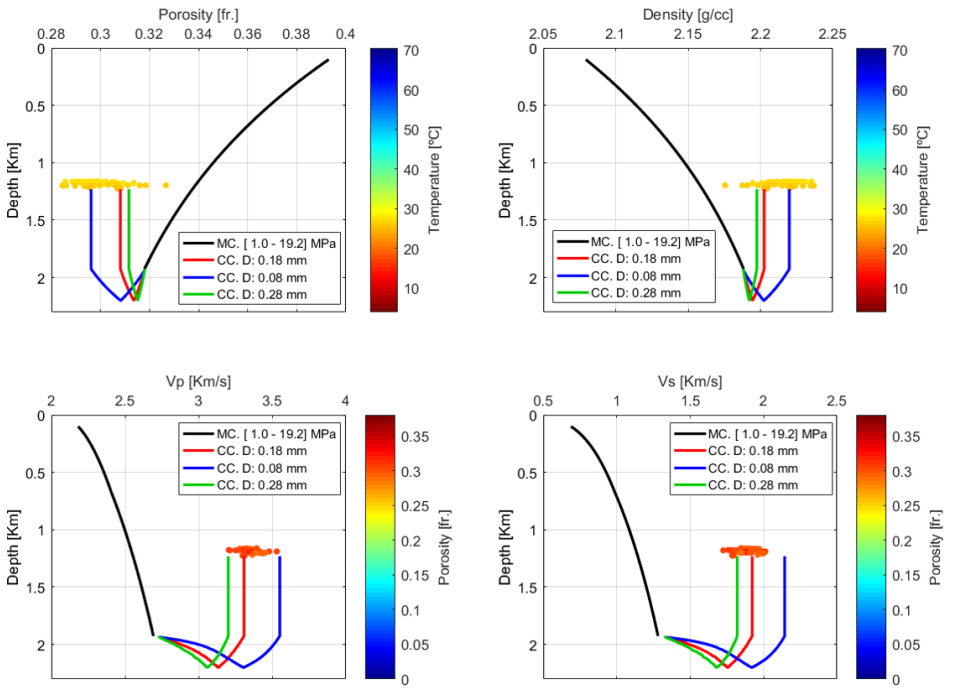

Figure 6.7: Porosity, Density, P-wave velocity, and S-wave velocity, modelled depth trends for the Tubåen Sandstones at well 7220/8-1. The net exhumation magnitude has been kept constant, and equal to the mean estimates for well 7220/8-1 using well 34/7-1 as reference. The gran size D is varied $\pm$ 0.10 mm from the selected value to evaluate the sensitivity of the modelling to this parameter.

to Zattin et al. (2016) results, reduces the sensitivity of this parameter for the present study.

One factor considered to be potentially of first order importance in the burial history modelling is the temperature-depth relation through time. In the present study, a constant temperature gradient equal to the present day gradient has been used for the modelling at each well location. Differences between the present-day depth temperature gradient and that at the time of maximum burial depth, are of equal importance compared to the net exhumation magnitudes. Zattin et al. (2016) thermochronology study was performed on apatite grains from Early-Middle Jurassic and Early Cretaceous sandstone samples from, among others, well 7220/10-1, which is analyzed in this study. Though some variations with time, in the temperature gradient, and in the water depth are portrayed in their burial history curves, the maximum temperature reached by their studied samples range between 80-90°C. This coincides with the maximum temperature of 84° modelled for the Middle Jurassic Stø Fm. at the same well location, in the our study. Moreover, Zattin et al. (2016) burial history modelling suggest a net temperature decrease due to 800-1000 m of erosion, of 30-33°C at well 7220/10-1. The latter is close to the 34°C decrease due to 900 m net exhumation, modelled in the present study. Thus, though variations in the geothermal

gradient through time can have severe impact on the modelling results, the assumption of constant geothermal gradient combined with constant water depth through time, seem reasonable at the locations studied.

Chapter 7

Conclusions

A new seismically based technique has been introduced for estimating net exhumation magnitudes in sedimentary basin areas. The method allowed for the estimation of net exhumation magnitudes at different locations across the Western Barents Sea. Three sets of net uplift magnitudes were estimated based on three selected reference wells. The estimates were used as input for the generation of burial history curves, which were used to simulate mechanical and chemical compaction in clean sandstone formations. The latter allowed for a comparison between the observed and modelled petrophysical properties, and thus for an evaluation of the quality of the net exhumation estimates. The key findings from the present study are summarized below:

- Differently from the shale compaction technique, the method proposed compares the entire stratigraphic sequences from reference and uplifted areas, and not an individual shale formation. Hence, the method allows for estimating net exhumation magnitudes at areas where reference shale units has been removed due to severe uplift and erosion, as it is the case for various locations within the Western Barents Sea.

- The method, compared to the shale compaction technique, is considered to be less affected by abnormal pore pressure building in the unexhumed reference area. The effective medium net uplift estimate is influenced by the velocity contributions of both overpressured and hydrostatically pressured rock units, and thus attenuation of the overpressure effect is expected.

- The differences observed between the three sets of net exhumation estimates are most likely caused due to exhumation in the Norwegian Sea reference area, and due to relative variations in the pore fluid pressure between the North Sea reference areas. This is supported by the pore fluid pressure profiles, and published compaction-

based net uplift studies carried out in the Norwegian and North sea. Moreover, reference well 34/7-1 is found to be the least affected by the aforementioned factors, and thus, its estimates are considered to be the most reliable.

- As suggested by previous studies, net exhumation magnitudes in the Western Barents Sea increases from the west and southwest where minor or no uplift have taken place, towards the East and North-East, where exhumation magnitudes between 800 m and 1700 m are estimated. The net exhumation magnitudes are in agreement with published estimates based on a variety of techniques ranging from shale compaction depth-trends, to thermal techniques, seismic reflection data, petrographical and sedimentological analysis, etc.

- Reconstruction of the Late-Cenozoic burial history of clean sandstones based on the net exhumation estimates allowed for a successful prediction of the observed petrophysical properties. The net exhumation magnitudes explains the mean values of porosity, density, bulk and shear dry elastic moduli, and P- and S- wave velocities, measured at well locations. Furthermore, the estimated quartz cement volumes are in agreement with published volumes quantified through petrographical thin section analysis for the same sands, at the same locations.

- The P-wave velocity represents the most important parameter for constraining the precipitated quartz cement volumes and the net exhumation magnitudes through burial history modelling. Oppositely to porosity and density, the P-wave velocity is not severely affected by authigenic pore-filling clay mineral precipitation. Furthermore, its prediction based on the Dvorkin-Nur contact-cement model is more reliable compared to the S-wave velocity estimation.

- The burial history modelling appeared to be most sensitive to the maximum temperatures achieved according to the net exhumation magnitudes. Other factors as grain size, and timing for maximum burial depth, are better constrained, and thus, are considered to be of second order importance. Changes with time in the temperature gradient and water depths are of first order importance. However, the assumption of time-invariant values, equal to the present day conditions, provided results in agreement with thermo-chronological published exhumation studies.

- The estimated net exhumation magnitudes are correlated to preset-day differential stress profiles. Furthermore, after correcting the Barents Sea sands to maximum burial depth, their velocities coincide to velocity depth-trends derived for unexhumed sandstones from the Norwegian and North Sea using mechanical and chemical compaction models.

- The estimated net exhumation magnitudes are correlated to preset-day differential stress profiles. Furthermore, after correcting the Barents Sea sands to maximum burial depth, their velocities are in agreement with mechanical and chemical compaction velocity depth-trends derived for unexhumed sandstones from the Norwegian and North Sea.

- The net exhumation examples presented in this study are based on traveltime data generated through isotropic ray tracing on well log data, and not real (anisotropic)

seismic data. Though the quantitative impact of anisotropy on the uplift estimate is still a topic of further research, the presented anisotropic short-example suggested similar uplift estimates compared to the isotropic analogue.

References

Al-Chalabi. (1974). An analysis of stacking, rms, average, and interval velocities of a horizontally layered ground. *Geophysical Prospecting*, 22:458–475.

Archie, G. E. et al. (1942). The electrical resistivity log as an aid in determining some reservoir characteristics. *Transactions of the AIME*, 146(1):54–62.

Athy, L. F. (1930). Density, porosity, and compaction of sedimentary rocks. *AAPG Bulletin*, 14(1):1–24.

Aven, E. (2017). Is it possible to estimate the magnitude of uplift and erosion by the use of checkshot data and average velocity? Master's thesis, Department of Geoscience and Petroleum, Norwegian University of Science and Technology (NTNU).

Avseth, P., Mukerji, T., Mavko, G., and Dvorkin, J. (2010). Rock-physics diagnostics of depositional texture, diagenetic alterations, and reservoir heterogeneity in high-porosity siliciclastic sediments and rocks – a review of selected models and suggested work flows. *Geophysics*, 75(5):75A31–75A47.

Backus, G. E. (1962). Long-wave elastic anisotropy produced by horizontal layering. *Journal of Geophysical Research*, 67(11):4427–4440.

Baig, I., Faleide, J. I., Jahren, J., and Mondol, N. H. (2016). Cenozoic exhumation on the southwestern barents shelf: Estimates and uncertainties constrained from compaction and thermal maturity analyses. *Marine and Petroleum Geology*, 73(Supplement C):105–130.

Batzle, M. and Wang, Z. (1992). Seismic properties of pore fluids. *Geophysics*, 57(11):1396–1408.

Bjørlykke, K. and Jahren, J. (2015). Sandstones and sandstone reservoirs. In *Petroleum Geoscience*, pages 119–149. Springer, Berlin, Heidelberg.

Blazevic, L. A. (2017). Modeling burial induced changes in physical sandstone properties: A case-study of north sea and norwegian sea sandstone formations. Master's

thesis, Department of Geoscience and Petroleum, Norwegian University of Science and Technology (NTNU).

Corcoran, D. V. and Dore, A. G. (2005). A review of techniques for the estimation of magnitude and timing of exhumation in offshore basins. *Earth-Science Reviews*, 72:129–168.

Dix, C. H. (1955). Seismic velocities from surface measurements. *Geophysics*, 20(1):68–86.

Doré, A. (1995). Barents sea geology, petroleum resources and commercial potential. *Arctic*, pages 207–221.

Dore, A. G. and Jensen, L. N. (1996). The impact of late cenozoic uplift and erosion on hydrocarbon exploration: offshore norway and some other uplifted basins. *Global and Planetary Change*, 12:415–436.

Dvorkin, J. and Nur, A. (1996). Elasticity of high-porosity sandstones: Theory for two north sea data sets. *Geophysics*, 61(5):1363–1370.

Dvorkin, J. and Nur, A. (2002). Critical-porosity models. *MEMOIRS-AMERICAN ASSOCIATION OF PETROLEUM GEOLOGISTS*, pages 33–42.

Dvorkin, J., Prasad, M., A., S., and Lavoie, D. (1999). Elasticity of marine sediments: Rock physics modeling. *GEOPHYSICAL RESEARCH LETTERS*, 26(12):1781–1784.

Faleide, J. I., Bjørlykke, K., and Gabrielsen, R. H. (2015). Geology of the norwegian continental shelf. In *Petroleum Geoscience*, pages 603–637. Springer.

Faleide, J. I., Gudlaugsson, S. T., and Jacquart, G. (1984). Evolution of the western barents sea. *Marine and Petroleum Geology*, 1(2):123–150.

Greenberg, M. and Castagna, J. (1992). Shear-wave velocity estimation in porous rocks: Theoretical formulation, preliminary verification and applications. *Geophysical prospecting*, 40(2):195–209.

Gyenis, T. (2016). Reservoir quality of the triassic snadd and kobbe formations in the barents sea. Master's thesis, Department of Geosciences, University of Oslo (UiO).

Hansen, S. (1996). Quantification of net uplift and erosion on the norwegian shelf south of 66n from sonic transit times of shale. *Norsk Geologisk Tidsskrift*, 76:245–252.

Heasler, H. P. and Kharitonova, N. A. (1996). Analysis of sonic well logs applied to erosion estimates in the bighorn basin, wyoming. *AAPG bulletin*, 80(5):630–646.

Henriksen, E., Bjrnseth, H. M., Hals, T. K., Heide, T., Kiryukhina, T., Kløvjan, O. S., Larssen, G. B., Ryseth, A. E., Rønning, K., Sollid, K., and Stoupakova, A. (2011a). Chapter 17 uplift and erosion of the greater barents sea: impact on prospectivity and petroleum systems. *Geological Society, London, Memoirs*, 35(1):271–281.

Henriksen, E., Ryseth, A. E., Larssen, G. B., Heide, T., Rønning, K., Sollid, K., and Stoupakova, A. V. (2011b). Chapter 10 tectonostratigraphy of the greater barents sea: implications for petroleum systems. *Geological Society, London, Memoirs*, 35(1):163–195.

Herron, D. (2011). *First Steps in Seismic Interpretation*. Society of Exploration Geophysicists.

Japsen, P. (1993). Influence of lithology and neogene uplift on seismic velocities in denmark: implications for depth conversion of maps. *AAPG Bulletin*, 77(2):194–211.

Jaspen, P. (1998). Regional velocity-depth anomalies, north sea chalk: A record of overpressure and neogene uplift and erosion. *AAPG Bulletin*, 82(11):2031–2074.

Jaspen, P. (2000). Investigation of multi-phase erosion using reconstructed shale trends based on sonic data. sole pit axis, north sea. *Global and Planetary Change*, 24(3):189–210.

Johansen, N. S. (2016). Regional net erosion estimations and implications for seismic avo signatures in the western barents sea. Master's thesis, Department of Geoscience and Petroleum, Norwegian University of Science and Technology (NTNU).

Lander, R. H. and Walderhaug, O. (1999). Predicting porosity through simulating sandstone compaction and quartz cementation. *AAPG Bulletin*, 83(3):433–449.

Li, Y. (2006). An empirical method for estimation of anisotropic parameters in clastic rocks. *The Leading Edge*, 25(6):706–711.

Magara, K. (1976). Thickness of removed sedimentary rocks, paleopore pressure, and paleotemperature, southwestern part of western canada basin. *AAPG Bulletin*, 60(a):554–566.

Mahmood, F. (2013). Reservoir quality of jurassic sandstones in sw barents sea: a mineralogical, petrographical and petrophysical approach. Master's thesis, Department of Geosciences, University of Oslo (UiO).

Margrave, G. F. (2000). New seismic modelling facilities in matlab. Technical report, CREWES Research Report 12.

Mavko, G., Mukerji, T., and Dvorkin, J. (2009). *The rock physics handbook: Tools for seismic analysis of porous media*. Cambridge university press.

Mondol, N. H. (2009). Porosity and permeability development in mechanically compacted silt-kaolinite mixtures. In *SEG Technical Program Expanded Abstracts 2009*, pages 2139–2143. Society of Exploration Geophysicists.

Ohm, S. E., Karlsen, D. A., and Austin, T. (2008). Geochemically driven exploration models in uplifted areas: Examples from the norwegian barents sea. *AAPG bulletin*, 92(9):1191–1223.

Porten, H. W. (2012). Petrography, diagenesis and reservoir quality of the triassic fruholmen, snadd and kobbe formations, southern barents sea. Master's thesis, Department of Geology and Mineral Resources Engineering, Norwegian University of Science and Technology (NTNU).

Ramm, M. and Bjørlykke, K. (1994). Porosity/depth trends in reservoir sandstones: assessing the quantitative effects of varying pore-pressure, temperature history and mineralogy, norwegian shelf data. *Clay Minerals*, 29:475–490.

Richardsen, G., Vorren, T. O., and Tørudbakken, B. O. (1993). Post-early cretaceous uplift and erosion tn the southern barents sea: a discussion based on analysis of seismic interval velocities. *Norsk Geologisk Tidsskrift*, 73:3–20.

Riis, F. and Fjeldskaar, W. (1992). On the magnitude of the late tertiary and quaternary erosion and its significance for the uplift of scandinavia and the barents sea. *Structural and tectonic modelling and its application to petroleum geology*, 1:163–185.

Riis, F. and Jensen, L. N. (1992). Introduction: Measuring uplit and erosion - proposal for a terminology. *Norsk Geologisk Tidsskrift*, 72:223–228.

Schlumberger (2009). *Log Interpretation Charts*. Schlumberger.

Smelror, M., Petrov, O., Larssen, G. B., and Werner, S. (2009). Geological history of the barents sea. *Norges Geol. undersøkelse*, pages 1–135.

Storvoll, V., Bjrlykke, K., and Mondol, N. H. (2005). Velocity-depth trends in mesozoic and cenozoic sediments from the norwegian shelf. *AAPG bulletin*, 89(3):359–381.

Stovas, A. and Ursin, B. (2007). Estimation of layer parameters for linear p- and s- wave velocity functions. *Geophysics*, 72(3):U27–U30.

Tassone, D. R., Holford, S. P., Duddy, I. R., Green, P. F., and Hillis, R. R. (2014). Quantifying cretaceous - cenozoic exhumation in the otway basin, southeastern australia, using sonic transit time data: Implications for conventional and unconventional hydrocarbon prospectivity. *The American Association of Petroleum Geologists*, 98(1):67–117.

Thomsen, L. (1986). Weak elastic anisotropy. *Geophysics*, 51(10):1954–1966.

Ursin, B. and Stovas, A. (2006). Traveltime approximations for a layered transversely isotropic medium. *Geophysics*, 71(2):D23–D33.

Vucelic, L. A. B., Duffaut, K., and Avseth, P. (2017). Burial induced changes in physical sandstone properties: A case study of north sea and norwegian sea sandstone formations. In *SEG Technical Program Expanded Abstracts 2017*, pages 3626–3631. Society of Exploration Geophysicists.

Walderhaug, O. (1996). Kinetic modeling of quartz cementation and porosity loss in deeply buried sandstone reservoirs. *AAPG bulletin*, 80(5):731–745.

Wilson, M. D. and Stanton, P. T. (1994). Diagenetic mechanisms of porosity and permeability reduction and enhancement. In *Reservoir quality assessment and prediction in clastic rocks*, pages 59–119. Special Publications of SEPM.

Zattin, M., Andreucci, B., de Toffoli, B., Grigo, D., and Tsikalas, F. (2016). Thermochronological constraints to late cenozoic exhumation of the barents sea shelf. *Marine and Petroleum Geology*, 73:97–104.

Appendix

Table 7.1: Sensitive temperature information at the locations studied across the Western Barents Sea. Note how quartz cementation temperatures (75°C), are generally reached at shallower depths compared to the Norwegian and North Sea, where onset temperatures are generally found at around 2 km deep.

Well	T @ (2km) [°C]	Z @ (75°C) [km]
7117/9-1 Torsk Sand	78.2	1.914
7120/9-2 Stø	70.1	2.149
7121/4-1 Stø	78.6	1.903
7131/4-1 Fruholmen	91.3	1.626
7220/8-1 Tubåen	77.72	1.926
7220/10-1 Stø	77.9	1.922
7222/11-1 Snadd	82.4	1.811
7316/5-1 Torsk Sand	105.1	1.405
7321/7-1 Stø	80.8	1.849

Table 7.2: Summary of pore fluid properties for the Barents Sea clean sandstone formations examined in the present study. K_{brine}, and K_{gas}, refer to the bulk moduli of the brine and gas, respectively. R_w refers to the water resistivity at the average temperature T, of the formation of interest. ρ_{brine} is the brine density. ρ_{gas} and G, are the gas density and gravity, respectively.
**** Well contains Oil and Gas.
** Well contains only Gas.
* Well contains only Oil.
* Water
( ) Value from report.
ˆWell is not dry, but brine-saturated formations or the brine-saturated interval of a hydrocarbon bearing formation is used in the modelling.

Well	ρ_{brine} [g/cm^3]	K_{brine} [g/cm^3]	ρ_{gas}	K_{gas} [Gpa]	R_w @ Sand	G	T [°C)]
7117/9-1*	1.0201	2.5312	-	-	0.12	-	37.31
7120/9-2***ˆ	1.1288	3.3724	-	-	0.028	-	60.81
7121/4-1*****	1.103	2.962	0.2003	0.0551	0.0284	0.741	79.15
7131/4-1*	1.2308	3.807	-	-	0.035	-	28.91
7220/8-1*****ˆ	1.1979	3.7023	-	-	0.032	-	47.57
7220/10-1***ˆ	1.1813	3.6149	-	-	0.02	-	47.68
7222/11-1*****ˆ	1.0163	2.5248	-	-	0.12	-	39.68
7316/5-1***ˆ	1.0213	2.6454	-	-	0.095	-	53.75
7321/7-1*	1.0844	3.1097	-	-	0.036	-	62.06

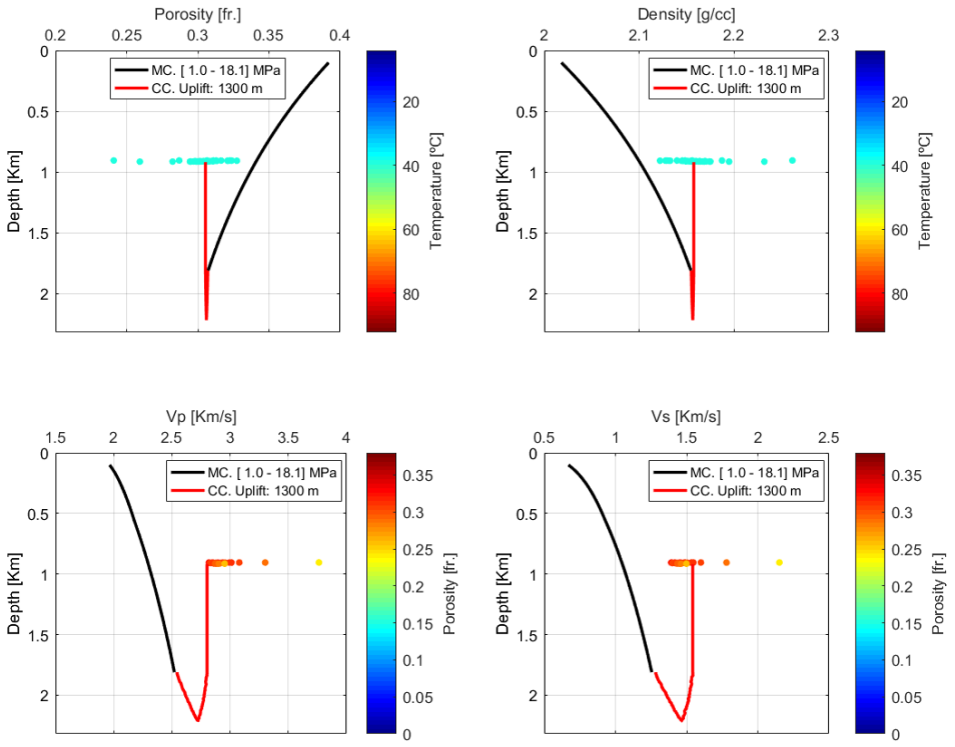

Figure 7.1: Porosity, density, P-wave velocity and S-wave velocity depth-trends after burial history modelling of the clean sands within Snadd Fm., at well 7222/11-1. MC refers to the mechanical compaction domain (Black). Property variations in the chemical compaction domain (CC) are shown in red. Circle-scattered data refers to the in-situ properties of the rock. Color represents formation porosity in the case of Vp and Vs, and formation temperature in the case of porosity and density.

Net exhumation estimation using an effective-medium technique based on seismic traveltime measurements.

Ricardo J. Martinez G. and Kenneth Duffaut.
Norwegian University of Science and Technology.

Summary:

We propose a new seismically based technique for estimating net exhumation magnitudes on sedimentary basin areas. The method uses traveltime measurements mapped from e.g. seismic data, or ray traced well log data, starting at the sea floor on a reference unexhumed area, and on an area suspected to be uplifted. Analogously to the shale compaction depth-trend methodology, where two homogenous shale formations with comparable petrophysical properties are identified, in reference and uplifted areas, we consider the stratigraphic columns instead as effective media with comparable NMO parameters and velocity heterogeneity. Linear P-wave velocity functions of both reference and uplifted areas are derived from dix-type mathematical relations, and compared in a depth dependent scheme. The methodology is applied in nine wells spread across the Norwegian part of the Barents Sea. Our technique provide results in agreement with published net exhumation magnitude estimates derived from standard compaction depth-trends and thermal maturity techniques. Our uplift magnitude estimates are further used to construct time-dependent burial curves for simulating mechanical and chemical compaction of sandstones. The modelling scheme predicts successfully quartz cement volumes quantified from petrographic analysis, and porosity, rock moduli, and velocities measured by wireline well logging.

Introduction

Net uplift, or net exhumation estimates represents one of the most important inputs in hydrocarbon exploration in some sedimentary basins. Together with its timing, it provides information about the maturation state of a source rock, the expected quality of the reservoirs, and the sealing capacity of a impermeable rock unit.

Shale compaction, net exhumation estimation techniques rely upon finding an homogeneous shale with similar characteristics in both, normally-compacted unexhumed areas, and uplifted areas. However, this is not always achieved. In the western Barents Sea, the Paleogene shale Fm., Torsk, is missing in areas that has experience severe uplift. Thus, older shale Fms. as the regionally preserved Lower Cretaceous Kolmule Fm. has to be used. Nevertheless, in areas as Vestbakken province, considered to be at the maximum burial depth by Baig et al. (2016), the wells do not penetrate this formation. Baig et al. (2016) addressed the problem by using wells from areas with minor uplift as the Tromsø Basin, where Kolmule Fm. is drilled, and depth correcting those wells to maximum burial depth based on uplift estimates from opal-A to opal-CT to quartz silica-phase transformation. This induces an extra uncertainty that adds to the uncertainty of the shale compaction method itself. Moreover, Henriksen et al. (2011) have reported uplift magnitudes of 250 m for wells used by Baig et al. (2016) to construct the Normal Compaction Trends (NCT's). The latter suggest underprediction of the net uplift magnitudes in studies where Barents Sea shales are used to construct the reference trend.

Stovas and Ursin (2007) presented a mathematical formulation that allows for estimation of a P-wave linear velocity function that explains the seismic traveltimes through a stack of isotropic layers, given PP seismic reflection curves are provided. The present study seeks to use Stovas and Ursin (2007) formulation, as the basis for estimating the net exhumation magnitude at different locations within the Western Barents Sea, using effective lithological columns rather than a particular shale unit. Moreover, since the uplift estimates will be based on composite lithological columns, wells within non-uplifted areas, from the Norwegian and North sea, can be used as reference. Lastly, the net uplift magnitudes will be used as input for burial history modelling using Lander and Walderhaug (1999) mechanical and chemical compaction models. The aim is to investigate whether the estimates can explain published quartz cement volumes observed from thin section analysis, and whether the porosity, elastic parameters and velocities measured at well locations, can be predicted.

Theory and Method

The seismic traveltimes down to a given reflector, in a stack of isotropic, horizontally layered strata with a given P-wave velocity profile can be explained by a linear P-wave velocity function of the effective single layer medium:

$$Vp(z) = Vp_0(1+\beta_p z) = Vp_0 + Kz \tag{1}$$

where $z = 0$ corresponds to the top of the layer, Vp_0 to the velocity at the top of the layer, β_p to the velocity gradient in units of $[m]^{-1}$ and K to the velocity gradient in units of $[s]^{-1}$.

For an isotropic, horizontally layered medium, with a constant P-wave velocity gradient, Stovas and Ursin (2007) developed a methodology that allows for estimating a linear P-wave velocity function from large offset PP seismic reflections. The method can be divided in three main steps:

1. Velocity analysis on large-offset PP seismic traveltimes curves to obtain NMO parameters at the top and bottom of a given layer.
2. Finding the solution of an equation relating the differences in effective NMO parameters T_0, V_{nmo} and S, between two reflections of interest.
3. Computing layer parameter Vp_0, β_p and the thickness of the layer H, from Stovas and Ursin (2007) analytical expressions.

The methodology, in short, consist in estimating linear P-wave velocity functions from wells or seismic data, from a reference unexhumed area, and from an uplifted area. The two linear trends are then compared and the net exhumation magnitude is computed from the vertical depth difference between the linear functions.

PP traveltime curves for the reference well are produced by performing ray tracing through the given P-wave interval velocity model. At each reflection depth Z_j, the maximum offset X_{max_j} was selected to be 2.5 times the depth of the reflector, to ensure large-offset condition. The receiver spacing was kept at 10 m to ensure enough sampling and to ease the velocity analysis. Prior to the ray racing, P- and S-wave velocity logs were upscaled by means of Backus averaging in 40 m thick intervals. This was done to simulate wave propagation at seismic frequencies, and at the same time, to avoid the critical reflections that would occur in response to the large velocity variations commonly observed at well logging frequencies.

To compute the effective NMO parameters, velocity analysis was carried on the measured traveltimes. The procedure comprised first, polynomial fitting on the measured curves to obtain an initial guess of the NMO velocity V_{nmo}, and zero-offset two-way traveltime T_0. In addition, traveltimes were modelled using Ursin and Stovas (2006) three-term approximation, assuming the heterogeneity coefficient S to be 1. Finally, the true value of the NMO parameters was computed by minimizing the differences between the observed and modelled traveltimes in a least square sense. Layer parameters were then computed using Stovas and Ursin (2007) analytical equations. With it, a linear velocity function that explains the traveltimes in the reference area was estimated, as shown in Figure 1a.

In addition, interval velocities were calculated through Dix inversion from the NMO velocities estimated at each interfase. The first was then used to compute the average velocity. The average velocity V_{avg}, and the RMS velocity V_{rms}, were then combined to compute Al-Chalabi. (1974) Heterogeneity Factor g (See Figure 1b). This quantity gives a measure of the degree of velocity heterogeneity in the ground and it is defined as:

$$g = \frac{V_{rms}^2 - V_{avg}^2}{V_{avg}^2} \tag{2}$$

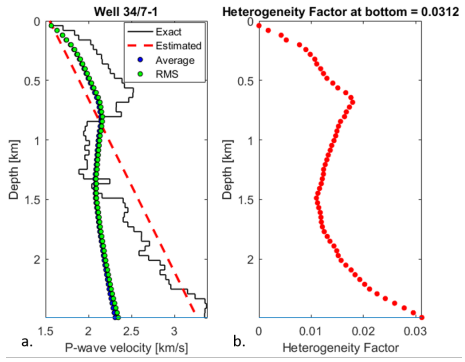

Figure 1 *a) P-wave velocity profile for the reference well 34/7-1 in the North Sea (Black) and the P-wave velocity function estimated for the model (Red). Calculated average and RMS velocities are also displayed. b) Heterogeneity Factor g. Note the correlation between g and the velocity variations in the model.*

The same procedure can be repeated for the uplifted well, and the linear P-wave velocity function that explains the traveltimes, can be estimated.

Note that in well log data examples, the interval velocity is known, and the NMO parameters can be computed through analytical equations. However, the method presented here is formulated assuming that the depth model is unknown, and that the traveltimes is the only input information.

Analogously to the shale compaction depth trend technique, where a shale formation with similar properties has to be found in reference and uplifted areas, we consider the two stratigraphic columns instead, as effective media, where equality of the two composite columns is evaluated in terms of the equality of T_0, V_{nmo}, S and g.

Consider a reference depth Z_1 selected in the unexhumed well, for instance the bottom of the well. Thus, the NMO parameters T_{0_1}, V_{nmo_1}, S_1, and the heterogeneity factor g_1 can be computed together with the pair $[Vp_{0_1}, K_1]$, which forms the linear P-wave velocity function that explains the traveltimes

down to Z_1 (Black curve, Figure 2). By performing velocity analysis on all reflections in the uplifted well, NMO parameters can be estimated at each interface. A search through the zero-offset two-way traveltimes in the uplifted well can be performed until a value T_{0_2} equal to T_{0_1} (or closest) is found at a certain depth. Thus, a linear P-wave velocity function that explains the traveltimes down to that depth can be estimated. Now, the procedure can be repeated for the other parameters V_{nmo}, S and g. This would provide a total of four linear functions defined by the four pairs $[Vp_{0_2T_0}, K_{2T_0}]$,$[Vp_{0_2V_{nmo}}, K_{2V_{nmo}}]$,$[Vp_{0_2S}, K_{2S}]$, and $[Vp_{0_2g}, K_{2g}]$, as shown in Figure 2. As previously addressed, from the compaction-based technique, the vertical difference between the P-wave linear curve in the reference and uplifted areas yields the amount of net uplift. However, the gradients of the velocity functions in reference and uplifted areas will generally be different. Hence, the uplift provided by a given criteria is computed by averaging the vertical differences at the upper and lower ends of the curves, as shown in Figure 2. The estimated linear function for a given criteria evaluated at the depth of equality $Vpl_2(Z_{2crit})$ might be lower or higher than the velocity of the reference function at the reference depth $Vpl_1(Z_1)$. Thus, the reference curve is extrapolated or contracted prior to the averaging, as depicted in Figure 2. Lastly, the mean of the four exhumation estimates yields the amount of net exhumation for the given reference depth.

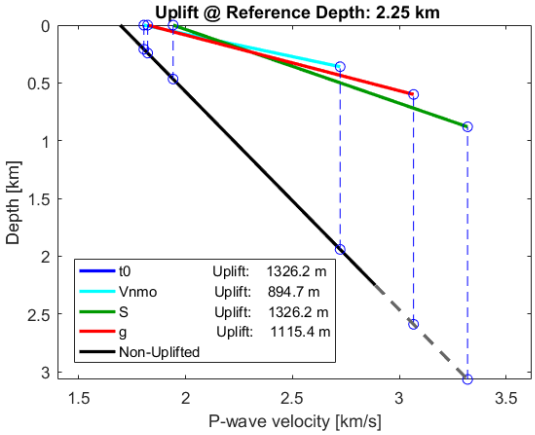

Figure 2 *P-wave linear velocity functions estimated for each criteria parameter. Note that T_0 curve is equal to and overlapped by the S curve. For each criteria, the uplift is computed by averaging the vertical differences between uplifted and reference curves at the upper and lower ends. Extrapolation of the reference function is shown in gray.*

Example

Net exhumation estimates are computed within nine wells at various locations across the Western Barents Sea, using unexhumed wells from the North Sea area as reference (33/5-2, 34/7-1, and 6507/12-1). An example from applying the technique on well 7131/4-1 located at the Finmark East area, using well 34/7-1 from the North Sea, as reference, is shown in Figure 3. The methodology explained above is repeated

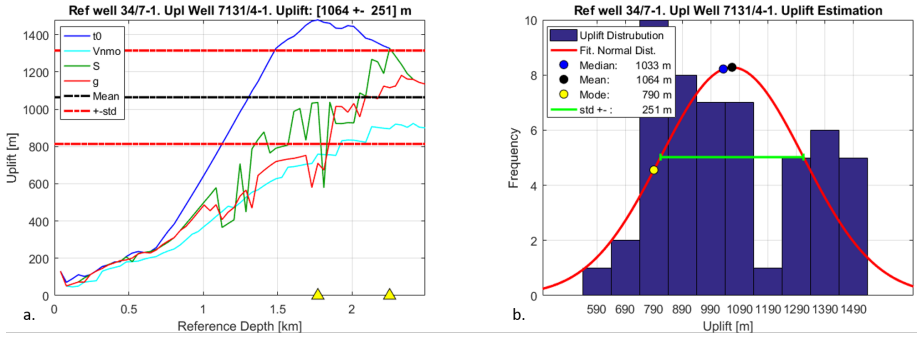

Figure 3 *Net uplift estimation in well 7131/4-1. Well 34/7-1 from the North Sea is used as the reference. a) Methodology repeated for each depth in the reference well. b) Simple statistical analysis from all uplift samples within the two yellow triangles on the (a) plot.*

for each depth in well 34/7-1, producing net exhumation curves as shown in Figure 3a. For shallow

depths, the procedure is rather unstable. As the method examines deeper depths, and P-wave functions are estimated for thicker lithological columns, the uplift increases and the method becomes stable. The yellow triangle located at around 1.75 km depth depicts the stabilization depth, given by the maximum of the T_0 uplift curve. The second yellow triangle at around 2.5 km depth represents the deepest depth point at which equal heterogeneity is found. A simple statistical analysis is then performed including all the samples from the uplift curves between the two yellow triangles, yielding the uplift chart shown in Figure 3b. Well 7131/4-1 is likely to be uplifted about 1064 +- 251 m, whose estimate comes from the mean and standard deviation of the examined samples.

Conclusions

Traveltime compaction-based effective medium techniques proved to be successful at estimating the magnitude of net exhumation for nine wells across the Norwegian Barents Sea. The results are in agreement with published net exhumation estimates from conventional shale compaction depth trends and thermal maturity techniques. Net exhumation results of well 7131/4-1, when used as input for the generation of time dependent burial curves, for simulating mechanical and chemical compaction in clean sandstones within the Fruholmen Fm., successfully predicts the quartz cement volumes quantified in petrographic analysis. Wireline well logging porosity, P-wave velocity and S-wave velocity are also predicted, as shown in Figure 4.

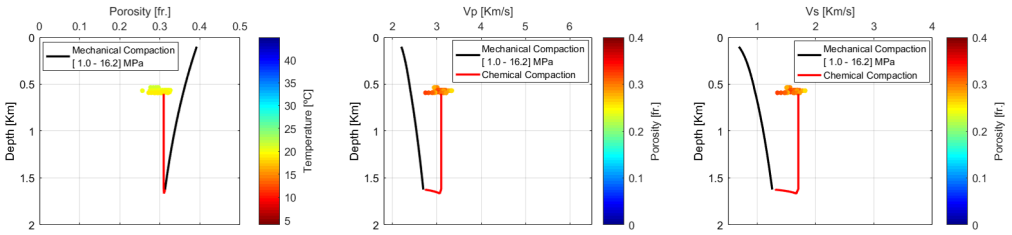

Figure 4 *Uplift estimates reproduce the porosity and velocities of the cleanest sandstones within the Fruholmen formation after burial history modelling using Lander and Walderhaug (1999) mechanical and chemical compaction models.*

Acknowledgements

We would like to acknowledge NPD-Schlumberger for the well log data provided, CREWES and Gary, F. Margrave for the Matlab Ray Tracing facility, and NTNU for permission to publish the results.

References

Al-Chalabi. [1974] An Analysis of Stacking, rms, Average, and Interval Velocities of a Horizontally Layered Ground. *Geophysical Prospecting*, **22**, 458–475.

Baig, I., Faleide, J.I., Jahren, J. and Mondol, N.H. [2016] Cenozoic exhumation on the southwestern Barents Shelf: Estimates and uncertainties constrained from compaction and thermal maturity analyses. *Marine and Petroleum Geology*, **73**(Supplement C), 105–130.

Henriksen, E., Bjørnseth, H.M., Hals, T.K., Heide, T., Kiryukhina, T., Kløvjan, O.S., Larssen, G.B., Ryseth, A.E., Rønning, K., Sollid, K. and Stoupakova, A. [2011] Chapter 17 Uplift and erosion of the greater Barents Sea: impact on prospectivity and petroleum systems. *Geological Society, London, Memoirs*, **35**(1), 271–281.

Lander, R.H. and Walderhaug, O. [1999] Predicting Porosity through Simulating Sandstone Compaction and Quartz Cementation. *AAPG Bulletin*, **83**(3), 433–449.

Stovas, A. and Ursin, B. [2007] Estimation of layer parameters for linear P- and S- wave velocity functions. *Geophysics*, **72**(3), U27–U30.

Ursin, B. and Stovas, A. [2006] Traveltime approximations for a layered transversely isotropic medium. *Geophysics*, **71**(2), D23–D33.